

THE CIRCUMGALACTIC MEDIUM OF NEARBY GALAXIES

*by*

DAVID M. FRENCH

A dissertation submitted in partial fulfillment of

the requirements for the degree of

DOCTOR OF PHILOSOPHY

(ASTRONOMY)

*at the*

UNIVERSITY OF WISCONSIN-MADISON

2018

Date of final oral examination: 6 August 2018

The dissertation is approved by the following members of the Final Oral Committee:

Dr. Bart Wakker, Senior Scientist, Astronomy

Dr. Elena D'Onghia, Assistant Professor, Astronomy

Dr. Christy Tremonti, Associate Professor, Astronomy

Dr. Peter Timbie, Professor, Physics

Dr. Robert Benjamin, Professor, Physics

# Abstract

The abstract!



## Acknowledgments

Acknowledgements!

# Contents

Abstract . . . . .	i
Dedication . . . . .	ii
Acknowledgments . . . . .	iii
Contents . . . . .	iv
List of Tables . . . . .	xi
List of Figures . . . . .	xii
<b>1 Introduction</b>	<b>1</b>
1.1 Overview of the Circumgalactic Medium . . . . .	2
1.2 Science Goals . . . . .	7
1.2.1 Galaxy Proximity . . . . .	8
1.2.2 Galaxy Orientation . . . . .	8
1.2.3 Galaxy Rotation . . . . .	9
1.3 Summary of Thesis . . . . .	10
References . . . . .	12
<b>2 A Catalogue of Nearby (<math>cz \leq 10,000 \text{ km s}^{-1}</math>) Galaxies</b>	<b>15</b>
Abstract . . . . .	16
2.1 Introduction . . . . .	17
2.2 Data . . . . .	18

2.2.1	Data Retrieval	18
2.2.2	Completeness	19
2.3	The Catalogue	25
2.3.1	Name	25
2.3.2	NEDname	26
2.3.3	z	26
2.3.4	RAdeg	26
2.3.5	DEdeg	26
2.3.6	RAh	26
2.3.7	RAm	26
2.3.8	RAs	26
2.3.9	DE-	26
2.3.10	DED	26
2.3.11	DEm	27
2.3.12	DEs	27
2.3.13	GLON	27
2.3.14	GLAT	27
2.3.15	Vhel	27
2.3.16	vcorr	27
2.3.17	distvcorr	27
2.3.18	RID_mean	28
2.3.19	RID_median	28
2.3.20	RID_std	28
2.3.21	RID_min	28
2.3.22	RID_max	28

2.3.23 bestDist . . . . .	28
2.3.24 e_bestDist . . . . .	29
2.3.25 distIndicator . . . . .	29
2.3.26 MajDiam_ang . . . . .	29
2.3.27 MinDiam_ang . . . . .	34
2.3.28 e_MajDiam_ang . . . . .	34
2.3.29 e_MinDiam_ang . . . . .	34
2.3.30 MajDiam . . . . .	35
2.3.31 MinDiam . . . . .	35
2.3.32 e_MajDiam . . . . .	35
2.3.33 e_MinDiam . . . . .	35
2.3.34 R_vir . . . . .	35
2.3.35 inc . . . . .	36
2.3.36 adjustedInc . . . . .	36
2.3.37 e_inc . . . . .	36
2.3.38 PA . . . . .	37
2.3.39 diam_key . . . . .	37
2.3.40 ratio_key . . . . .	37
2.3.41 pa_key . . . . .	37
2.3.42 RC3_type . . . . .	37
2.3.43 RC3_d25 . . . . .	37
2.3.44 RC3_r25 . . . . .	38
2.3.45 RC3_pa . . . . .	38
2.3.46 group_num . . . . .	38
2.3.47 group_mem . . . . .	38

2.3.48	group_dist	38
2.3.49	MType	38
2.3.50	flag	38
2.3.51	lumClass	39
2.3.52	E(B-V)	40
2.3.53	Bmag	40
2.3.54	Bmag_key	40
2.3.55	Bmag_max	40
2.3.56	Bmag_max_key	41
2.3.57	Bmag_min	41
2.3.58	Bmag_min_key	41
2.3.59	Bmag_sdss	41
2.3.60	gmag_sdss	41
2.3.61	rmag_sdss	41
2.3.62	zmag_sdss	41
2.3.63	Lstar_med	42
2.3.64	e_Lstar_med	42
2.3.65	Lstar_max	42
2.3.66	e_Lstar_max	42
2.3.67	Lstar_min	42
2.3.68	e_Lstar_min	43
2.3.69	Lstar_sdss	43
2.3.70	e_Lstar_sdss	43
2.3.71	altNames	43
2.4	Limitations & Future	43

References . . . . .	44
<b>3 Probing Large Galaxy Halos</b>	<b>46</b>
Abstract . . . . .	47
3.1 INTRODUCTION . . . . .	48
3.2 DATA AND ANALYSIS . . . . .	51
3.2.1 Galaxy Data . . . . .	51
3.2.2 Spectra . . . . .	54
3.3 RESULTS . . . . .	57
3.3.1 EW- $\rho$ Anti-correlation . . . . .	61
3.3.2 Inclination . . . . .	64
3.3.3 Velocity Difference ( $\Delta v$ ) . . . . .	67
3.3.4 Azimuth . . . . .	69
3.4 DISCUSSION . . . . .	72
3.5 SUMMARY . . . . .	74
References . . . . .	75
<b>4 Rotation in CGM</b>	<b>78</b>
Abstract . . . . .	79
4.1 INTRODUCTION . . . . .	80
4.2 DATA AND ANALYSIS . . . . .	87
4.2.1 SALT Data . . . . .	87
4.2.2 COS Spectra . . . . .	89
4.3 Halo Rotation Model . . . . .	89
4.4 Discussion . . . . .	94
4.4.1 Co-rotation Fraction . . . . .	95

4.4.2	Co-rotation as a function of $L^*$	99
4.4.3	Doppler $b$ -parameters	100
4.5	Summary	101
	References	110
A	SALT Galaxies	113
A.1	CGCG039-137	113
A.2	ESO343-G014	113
A.3	IC5325	114
A.4	MCG-03-58-009	115
A.5	NGC1566	116
A.6	NGC3513	118
A.7	NGC3633	119
A.8	NGC4536	120
A.9	NGC4939	121
A.10	NGC5364	122
A.11	NGC5786	123
A.12	UGC09760	124
B	Ancillary Data	126
B.1	NGC3198	127
B.2	NGC3351	128
B.3	NGC5907	128
B.4	NGC4565	129
B.5	UGC06446	129
B.6	NGC3631	129
B.7	NGC3726	130

B.8	NGC3067	131
B.9	NGC6140	132
B.10	NGC4529	133
B.11	UGC04238	133
B.12	NGC2770	133
B.13	NGC3432	135
B.14	NGC3666	136
B.15	NGC5951	136
B.16	NGC7817	137
B.17	UGC08146	137
<b>5</b>	<b>Conclusions</b>	<b>138</b>

# List of Tables

2.1	Distance Indicator Keys . . . . .	30
2.2	Summary of Diameter, Ratio, and P.A. Sources and Fits . . . . .	33
3.1	COS Targets in this Sample . . . . .	55
3.2	All Associated Systems Galaxy-absorber Systems . . . . .	59
3.3	Average properties of the associated galaxy sample split into red and blue-shifted bins based on $\Delta v$ . . . . .	73
4.1	SALT Galaxy Observations . . . . .	83
4.2	Summary of QSO Sample . . . . .	84
4.2	Summary of QSO Sample . . . . .	86
4.3	Halo Model Results and Ly $\alpha$ Absorption Properties . . . . .	92
4.3	Halo Model Results and Ly $\alpha$ Absorption Properties . . . . .	93
4.3	Halo Model Results and Ly $\alpha$ Absorption Properties . . . . .	94
4.4	Summary of Results . . . . .	96

# List of Figures

1.1	An artist's impression of the CGM of a galaxy. Image credit: NASA/STScI/Ann Field.	4
1.2	The EW of Ly $\alpha$ absorbers as a function of distance to the center of a galaxy filament. Blue downward tracing triangles indicate upper limits for non-detection, and all stars indicate detections with red stars for detections within a galaxy's virial radius and blue for those far from any known galaxy. See Wakker et al. (2015).	5
1.3	The linewidth (or Doppler $b$ -parameter) and FWHM of Ly $\alpha$ absorbers as a function of physical impact parameter to the nearest galaxy. Histograms show the 10th, 50th, and 90th percentiles of the distribution. See Wakker & Savage (2009).	6
1.4	A simulated galaxy halo showing the coherent co-rotation of halo gas out at least 100 kpc from the inner disk (the galaxy disk is seen in dark blue and red at the image center; see Stewart et al. (2011a)).	10

2.1 Distribution of $L/L^*$ values for all galaxies in the dataset. Black vertical lines highlight 1, 0.5, 0.1, 0.05 and 0.01 $L^*$ . The turnoff in the distribution for each region reveals the corresponding completeness. We are highly complete to $0.01L^*$ out to $2500 \text{ km s}^{-1}$ , $0.05L^*$ between $2500 \leq cz \leq 5000 \text{ km s}^{-1}$ , $0.1L^*$ between $6000 \leq cz \leq 8000 \text{ km s}^{-1}$ , and $0.3L^*$ $8000 \leq cz \leq 10000 \text{ km s}^{-1}$ . See §3.1 for a discussion of these limits. . . . .	20
2.2 Number of objects included from the major sources 2MASS (solid-black), SDSS (dashed-red), 2dF (solid-gold-crosses), 6dF (dot-dashed-green), RC3 (dotted-diamond-blue) and all other sources (solid-grey) plotted as a function of heliocentric velocity. The peak for “other sources” between $2500 \lesssim v_{\text{hel}} \lesssim 3100 \text{ km s}^{-1}$ is due to the small (1.3 square degrees) ultra-deep Subaru/XMM-Newton Deep Sky Survey (SXDS), which reaches a $B$ -band magnitude limit of $B = 28.2$ . . . . .	21
2.3 The positions of all galaxies with $flag = 0$ (see 2.3.50 below) plotted in Aitoff projection and colored according to heliocentric velocity. We include 3 maps, centered here at R.A. = 0h. See below for R.A. = 6h and R.A. = 12h centered maps. . . . .	22
2.3 The positions of all galaxies with $flag = 0$ (see 2.3.50 below) plotted in Aitoff projection and colored according to heliocentric velocity. We include 3 maps, centered here at R.A. = 6h. See above and below for R.A. = 0h and R.A. = 12h centered maps. . . . .	23
2.3 The positions of all galaxies with $flag = 0$ (see 2.3.50 below) plotted in Aitoff projection and colored according to heliocentric velocity. We include 3 maps, centered here at R.A. = 12h. See above for R.A. = 0h and R.A. = 6h centered maps. . . . .	24

2.4 Relationship between absolute $B$ -band magnitude and physical diameter for all galaxies with available data. Data are in grey, and a least-squares fit is shown in blue. The function form of this fit is $M = a \log_{10}(D) + b$ , with fit parameters $a = -4.696 \pm 0.01$ and $b = -12.963 \pm 0.01$ . We also include the fit derived by Wakker & Savage (2009) in dashed-red. . . . .	34
3.1 Distribution of $L/L^*$ values for all galaxies in the dataset. The red dashed vertical lines highlight 1, 0.5, 0.1, 0.05 and 0.01 $L^*$ . . . . .	52
3.2 (a) An example of 2 Ly $\alpha$ lines found in the Mrk290 sightline at 3105 and 3207 . (b) A map of <i>all</i> galaxies within a 500 kpc impact parameter of target Mrk290 sightline and with velocity ( $cz$ ) within $400 \text{ km s}^{-1}$ of absorption detected at 3207 $\text{km s}^{-1}$ (central black star). The galaxy NGC5987 ( $v = 3010 \text{ km s}^{-1}$ , inclination $= 65^\circ$ ) has been paired with the Ly $\alpha$ absorption features at $v = 3105, 3207 \text{ km s}^{-1}$ because it is the largest and closest galaxy in both physical and velocity space to the absorption feature. . . . .	62
3.3 (a) Equivalent width of each absorber as a function of impact parameter $\rho$ . (b) Equivalent width as a function of $\rho/R_{\text{vir}}$ . The anti-correlation is strongest when scaling $\rho$ by the galaxy virial radius. Absorbers are separated into redshifted and blueshifted samples based on $\Delta v$ . Bins of mean $EW$ are overplotted in red dotted, and blue dashed lines for their respective samples. Open symbols correspond to systems with $\rho \leq R_{\text{vir}}$ . . . . .	63

3.4 (a) Equivalent width of each absorber as a function of the virial radius of the associated galaxy. (b) Impact parameter to each absorber as a function of the virial radius of the associated galaxy. The black dashed line indicates the cutoff at $\rho/R_{\text{vir}} = 2.14$ imposed by our $\mathcal{L}$ limit. In each, the blue dashed and red dotted lines show the average $EW$ in 50 kpc bins of impact parameter for the blueshifted and redshifted absorbers, respectively. Open symbols correspond to systems with $\rho \leq R_{\text{vir}}$ . . . . .	64
3.5 Equivalent width of each absorber as a function of the inclination angle of the associated galaxy. The black and dashed gray lines show the mean and 90th percentile $EW$ of all absorbers in bins of $15^\circ$ . Open symbols correspond to systems with $\rho \leq R_{\text{vir}}$ . . . . .	65
3.6 Top: distribution of inclinations for all associated galaxies, split into redshifted and blueshifted sets. Bottom: distribution of inclinations of all observed galaxies in the $cz \leq 10,000 \text{ km s}^{-1}$ redshift range. The dashed line shows the inclination distribution for a truly random sample (i.e., no observational biases). . . . .	66
3.7 Equivalent width as a function of the velocity separation between the galaxy and absorption line. Open symbols correspond to systems with $\rho \leq R_{\text{vir}}$ . . . . .	68
3.8 Azimuth is the angle, $\alpha$ , between the major axis of the galaxy, $a$ , and a vector extending from the QSO target to the galaxy center. Image of NGC891 credit: composite Image Data - Subaru Telescope (NAOJ), Hubble Legacy Archive, Michael Joner, David Laney (West Mountain Observatory, BYU); Processing - Robert Gendler. . . . .	69

3.9 The distributions of azimuth angles for red and blue-shifted samples, with the combined sample plotted in black. Azimuth = 0 corresponds to absorption detected along the projected major axis of the galaxy, and Azimuth = 90 is along the minor axis. . . . .	70
3.10 A map of where each absorber was detected with respect to the associated galaxies, separated into three bins of inclination (illustrated by the gray ellipse in the bottom left corner of each plot). Left: absorbers associated with galaxies of inclination $0 \leq Inc \leq 40$ ; center: $40 \leq Inc \leq 65$ ; and right: $65 \leq Inc$ . Blueshifted and redshifted absorbers are separated into the top (diamonds) and bottom (circles) panels, and the marker size is scaled with $EW$ . The sightlines containing multiple absorbers associated with the same galaxy can be identified by their darker colors. Open symbols correspond to systems with $\rho \leq R_{vir}$ . . . . .	71
4.1 Left: The rotation curve for NGC3633 is shown in black, with the outer 1/2 mean rotation velocity indicated in green. Our cylindrical model simply extends this green average velocity out to $3R_{vir}$ . Middle: The observed rotation curve is again shown in black, with an NFW profile fit overlaid in green. Right: The model velocity predictions for the cylindrical and NFW models are shown in dashed-black and solid-green (respectively). . . . .	85
4.2 A 3D example mockup of our halo rotation model showing the orientation and extent of the NGC3633 model from 3 different viewing angles. The approaching extreme edge of the NGC3633 cylindrical halo is shown by dark-blue oval, with the far edge shown in red. The dark-grey line shows the location of the sightline toward RX_J1121.2+0326 as it penetrates the halo, with a red star marking the first intercept point. . . . .	85

- 4.3 A map of the locations of each absorber normalized with respect to the galaxy virial radius, with *no* additional constraints. The color and style of each point indicates the line-of-sight velocity compared to that of the rotation of the nearby galaxy. Blue diamonds indicate co-rotation, red crosses indicate anti-rotation, and grey circles indicate cases where either is possible due to a combination of orientation and velocity uncertainties. The size of each point is scaled to reflect the EW of the absorber. Concentric rings indicate distances of 1, 2, and 3  $R_{\text{vir}}$ . All galaxies are rotated to PA = 90 or 270, such that their major axis' are horizontal and their approaching side is on the left as indicated. The number identifiers correspond to the system number given in column (1) of Table 4.3. . . . . 104
- 4.4 A map of the locations of each absorber normalized with respect to the galaxy virial radius. A zoom in showing only those systems within  $1R_{\text{vir}}$  (exactly the same as Figure 4.3 within  $1R_{\text{vir}}$ ). The color and style of each point indicates the line-of-sight velocity compared to that of the rotation of the nearby galaxy. Blue diamonds indicate co-rotation, red crosses indicate anti-rotation, and grey circles indicate cases where either is possible due to a combination of orientation and velocity uncertainties. The size of each point is scaled to reflect the EW of the absorber. All galaxies are rotated to PA = 90 or 270, such that their major axis' are horizontal and their approaching side is on the left as indicated. The number identifiers correspond to the system number given in column (1) of Table 4.3. . . 105

4.5 A map of the locations of each absorber normalized with respect to the galaxy virial radius. The color and style of each point indicates the NFW rotation model results for each absorber with a $v_{\text{Ly}\alpha} \leq v_{\text{rot}}$ constraint imposed. Concentric rings indicate distances of 1, 2, and 3 $R_{\text{vir}}$ . Blue diamonds indicate co-rotation, red crosses indicate anti-rotation, and grey circles indicate cases where either is possible due to a combination of orientation and velocity uncertainties. The size of each point is scaled to reflect the EW of the absorber. All galaxies are rotated to PA = 90 or 270, such that their major axis' are horizontal and their approaching side is on the left as indicated. The number identifiers correspond to the system number given in column (1) of Table 4.3. . . . .	106
4.6 <b>Top:</b> The fraction of co-rotating absorbers as a function of $L^*$ . The upper edges of the $L^*$ bins are located at 0.5, 1.0, 1.7, and $> 1.7 L^*$ (i.e., all systems $1.7L^*$ and higher). <b>Bottom:</b> The fraction of co-rotating absorbers as a function of cumulative $L^*$ distribution. All systems are included at the $L^* = 2.0$ bin (this bin includes galaxies brighter than $2.0L^*$ as well), then only galaxies with $L^* \leq 1.8$ are included at $L^* = 1.8$ , and so on. . . . .	107

4.7 A map of the locations of each absorber normalized with respect to the galaxy virial radius. The color and style of each point indicates the NFW rotation model results for each absorber with $\Delta v \leq v_{rot}$ and $L^* \leq 0.6$ constraints imposed. Blue diamonds indicate co-rotation, red crosses indicate anti-rotation, and grey circles indicate cases where either is possible due to a combination of orientation and velocity uncertainties. The size of each point is scaled to reflect the EW of the absorber. Concentric rings indicate distances of 1, 2, and 3 $R_{vir}$ . All galaxies are rotated to PA = 90 or 270, such that their major axis' are horizontal and their approaching side is on the left as indicated. The number identifiers correspond to the system number given in column (1) of Table 4.3. . . . .	108
4.8 <b>Top:</b> The distributions of Doppler $b$ -parameters for all Ly $\alpha$ absorbers with $\Delta v \leq v_{rot} \pm 10 \text{ km s}^{-1}$ . The co-rotating versus anti-rotating designation here is based on NFW results. In the middle we do the same but only for $\rho \leq 1R_{vir}$ , and on the bottom we separate based on absorbers near $L^* \leq 0.6$ (blue) and $L^* > 0.6$ (red-hatched) galaxies. <b>Bottom:</b> The Doppler $b$ -parameters of each absorber as a function of $\Delta v$ , split into co-rotating (blue diamonds) and anti-rotating (red crosses). The data point for the NGC3067-3C232 LLS ( $b = 245.2 \pm 25.9$ , $\Delta v = -68.0 \pm 11 \text{ km s}^{-1}$ , co-rotating) is not shown in order to highlight the majority distribution in greater detail. . . . .	109
4.9 a) Rotation curve of CGCG039-137. The solid green line indicates the weighted mean velocity over the corresponding x-axis region, and the shaded green indicates the $1\sigma$ error in the mean. b) SALT finder chart for CGCG039-137 showing the position of the slit in red. . . . .	114

4.10 a) Rotation curve of ESO343-G014. The solid green line indicates the weighted mean velocity over the corresponding x-axis region, and the shaded green indicates the $1\sigma$ error in the mean. b) SALT finder chart for ESO343-G014 showing the position of the slit in red. . . . .	115
4.11 a) Rotation curve of IC5325. The solid green line indicates the weighted mean velocity over the corresponding x-axis region, and the shaded green indicates the $1\sigma$ error in the mean. b) SALT finder chart for IC5325 showing the position of the slit in red. . . . .	116
4.12 a) Rotation curve of MCG-03-58-009. The solid green line indicates the weighted mean velocity over the corresponding x-axis region, and the shaded green indicates the $1\sigma$ error in the mean. b) SALT finder chart for MCG-03-58-009 showing the position of the slit in red. . . . .	117
4.13 a) Rotation curve of NGC1566. The solid green line indicates the weighted mean velocity over the corresponding x-axis region, and the shaded green indicates the $1\sigma$ error in the mean. b) SALT finder chart for NGC1566 showing the position of the slit in red. . . . .	118
4.14 a) Rotation curve of NGC3513. The solid green line indicates the weighted mean velocity over the corresponding x-axis region, and the shaded green indicates the $1\sigma$ error in the mean. b) SALT finder chart for NGC3513 showing the position of the slit in red. . . . .	119
4.15 a) Rotation curve of NGC4536. The solid green line indicates the weighted mean velocity over the corresponding x-axis region, and the shaded green indicates the $1\sigma$ error in the mean. b) SALT finder chart for NGC3633 showing the position of the slit in red. . . . .	120

4.16 a) Rotation curve of NGC4536. The solid green line indicates the weighted mean velocity over the corresponding x-axis region, and the shaded green indicates the $1\sigma$ error in the mean. b) SALT finder chart for NGC4536 showing the position of the slit in red. . . . .	122
4.17 a) Rotation curve of NGC4939. The solid green line indicates the weighted mean velocity over the corresponding x-axis region, and the shaded green indicates the $1\sigma$ error in the mean. b) SALT finder chart for NGC4939 showing the position of the slit in red. . . . .	123
4.18 a) Rotation curve of NGC5364. The solid green line indicates the weighted mean velocity over the corresponding x-axis region, and the shaded green indicates the $1\sigma$ error in the mean. b) SALT finder chart for NGC5364 showing the position of the slit in red. . . . .	124
4.19 a) Rotation curve of NGC5786. The solid green line indicates the weighted mean velocity over the corresponding x-axis region, and the shaded green indicates the $1\sigma$ error in the mean. b) SALT finder chart for NGC5786 showing the position of the slit in red. . . . .	125
4.20 a) Rotation curve of UGC09760. The solid green line indicates the weighted mean velocity over the corresponding x-axis region, and the shaded green indicates the $1\sigma$ error in the mean. b) SALT finder chart for UGC09760 showing the position of the slit in red. . . . .	126

# Chapter 1

## Introduction

Galaxies must accrete gas from the intergalactic medium (IGM) in order to sustain star formation at observed levels. In order to understand this complex process, and how it influences galaxy evolution globally, it is necessary to understand the physical conditions and distribution of the gas around galaxies, known as the circumgalactic medium (CGM). This thesis aims to address these questions through the largest-to-date survey of low column density Ly $\alpha$  absorption detected in the spectra of background QSOs taken by the Cosmic Origins Spectrograph (COS) on the *Hubble Space Telescope (HST)*. By correlating the positions of detected absorption lines with the galaxies in their proximity, I aim to gain insights to the complex relationship between intergalactic gas and the galaxies which feed on it. This introduction provides some historical and astrophysical perspective, as well as an overview of the methods and history of QSO absorption line spectroscopy.

## 1.1 Overview of the Circumgalactic Medium

The majority ( $\sim 90\%$ ) of the baryons in the universe are found *outside* of galaxies, in the diffuse intergalactic and circumgalactic media (IGM/CGM). We define the CGM as the gas for which a nearby galaxy's gravity dominates, which generally extends to approximately a virial radius (see, e.g., Shull 2014). The IGM, CGM and the galaxies that reside in it are tightly linked by processes such as feedback and accretion. In order to sustain the level of star formation observed, galaxies must accrete gas throughout their lifetimes (e.g., Oort 1966, 1969, 1970; Tinsley & Larson 1978; Tinsley & Danly 1980; Wakker et al. 1999; Erb 2008; Prochaska & Wolfe 2009). At the same time, ongoing star formation and active galactic nuclei (AGN) activity produce feedback that drives gas back into the IGM. This life cycle of gas is complex, and difficult to constrain observationally. Understanding the properties of the IGM, such as its densities, temperatures, motions, and its relationship to the galaxies embedded within it is *essential* for explaining the evolution of galaxies and

the star formation history of the Universe.

The properties of the vast reservoir of material in the IGM can be understood by analyzing lines of sight toward background quasi-stellar objects (QSOs). Individual concentrations of gas along a given sightline imprint a ‘forest’ of absorption lines on the spectrum in the direction of the QSO target. The metal lines trace the star formation history within the intervening gas, and neutral hydrogen lines ( $\text{Ly}\alpha$  is one of the most commonly and easily observed) indicate both the location and velocities of outflowing gas, as well as the presence of fuel for future star formation. Figure 1.1 shows an artists impression of a galaxy complete with a CGM halo with arrows indicating outflowing and recycling material, and an illustration of a HST sightline detecting halo gas absorption. The relationship between the galaxies and the IGM is usually studied by looking for galaxies that lie at similar redshifts as detected absorption lines. This approach has value but is incomplete; it does not allow for an unbiased understanding of the distribution of the gas around galaxies, which requires looking for both detections and non-detections of gas, both near as well as far away from galaxies.

The current standard model of structure formation is given by Lambda Cold-Dark-Matter ( $\Lambda\text{CDM}$ ) cosmology, which predicts the hierarchical growth of large scale structures seeded by initial fluctuations in the dark matter background. In this picture, both galaxies and the IGM should follow the same underlying density profile (e.g., Fukugita & Peebles 2006; Frieman et al. 2008 and references therein). Some observational evidence of this large-scale relationship has appeared recently, such as Wakker et al. (2015), who showed that  $\text{Ly}\alpha$  absorption strength (equivalent width; EW) traces the overall distribution of galaxies in a Cosmic Web filament. Figure 1.2 shows their plot of the EW of  $\text{Ly}\alpha$  absorbers as a function of distance to the center of a galaxy filament, with the enhanced absorption strength evident close to the filament center. In addition, numerous studies have shown

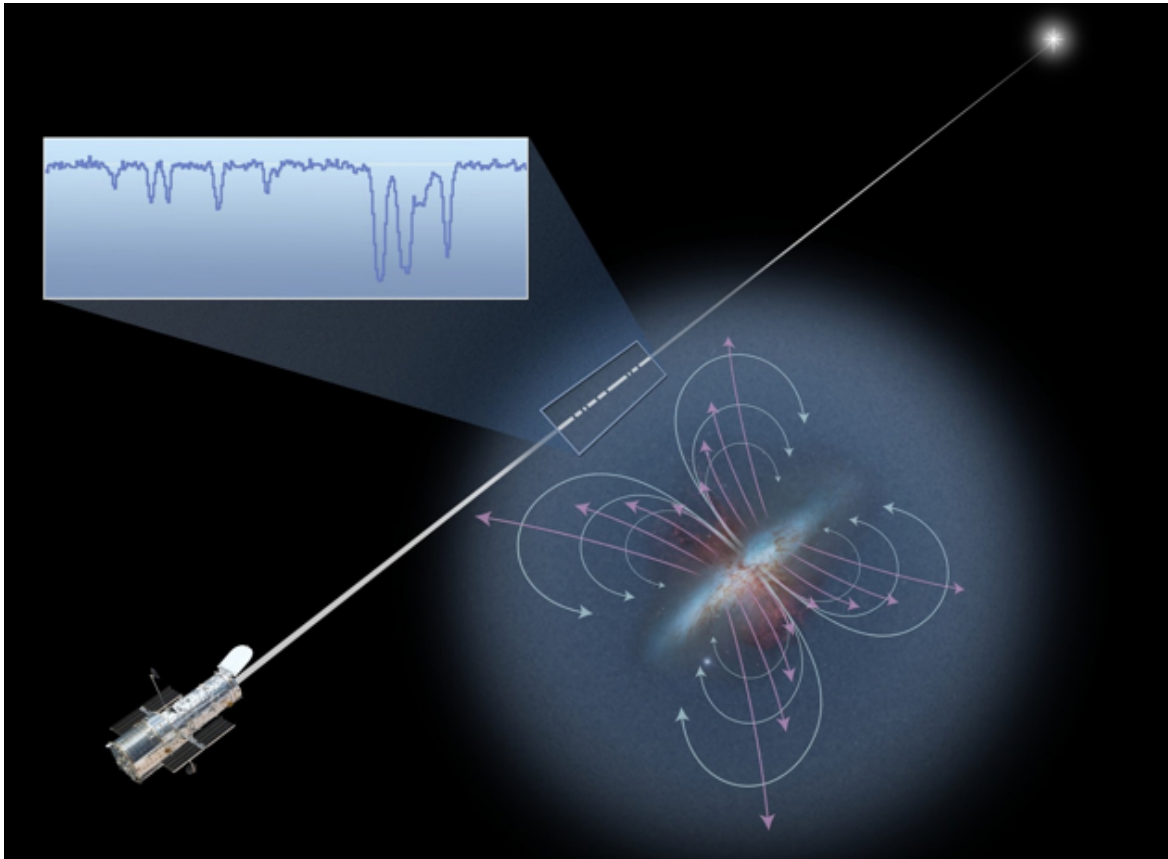


**Figure 1.1 :** An artist's impression of the CGM of a galaxy. Image credit: NASA/STScI/Ann Field.

that Ly $\alpha$  absorbers also trace individual galaxy halos (e.g., Lanzetta et al. 1995; Chen et al. 1998, 2001; Tripp et al. 1998; Bowen et al. 2002; Côté et al. 2005; Wakker & Savage 2009; Steidel et al. 2010; Prochaska et al. 2011; Thom et al. 2012; Stocke et al. 2013; Tumlinson et al. 2013; Liang & Chen 2014; Danforth et al. 2016).

The majority of these studies have reported tentative evidence for enhanced Ly $\alpha$  absorption strength with increasing galaxy proximity. The studies of Côté et al. (2005) and Prochaska et al. (2006) found that about half of Ly $\alpha$  absorbers lie within galaxy halos, at impact parameters  $\rho \lesssim 350$  kpc. In addition, Wakker & Savage (2009) found that for 90% of  $L > 0.1L^*$  galaxies an absorber can be found within 400 kpc and  $400 \text{ km s}^{-1}$ , and

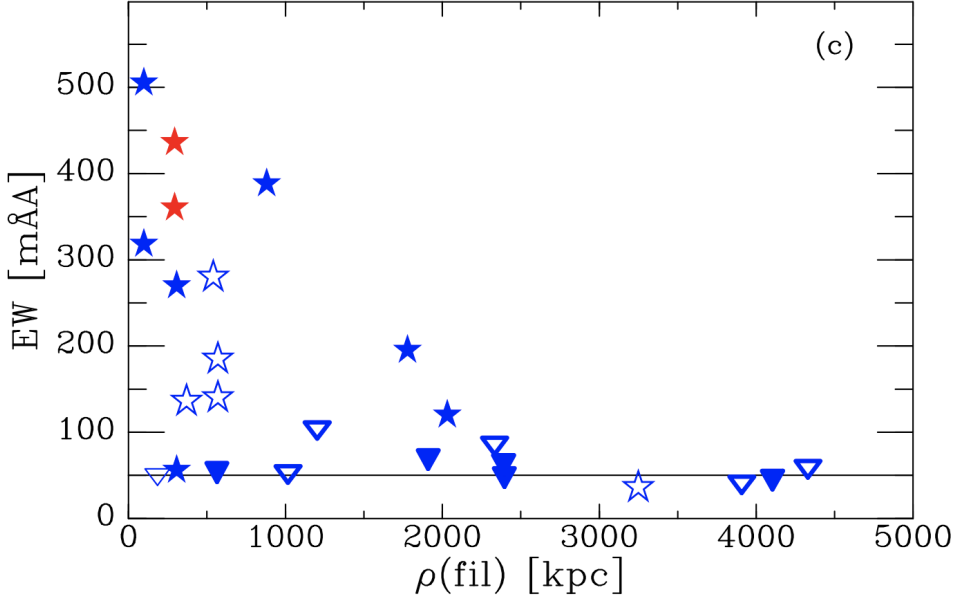


**Figure 1.2 :** The EW of Ly $\alpha$  absorbers as a function of distance to the center of a galaxy filament. Blue downward tracing triangles indicate upper limits for non-detection, and all stars indicate detections with red stars for detections within a galaxy’s virial radius and blue for those far from any known galaxy. See Wakker et al. (2015).

all galaxies have a Ly $\alpha$  absorber within 1.5 Mpc. Higher redshift studies, such as Rudie et al. (2012) at  $2 < z < 3$ , find evidence for an elevated density of absorbers up to 2 Mpc from galaxies. Wakker & Savage (2009) also confirmed a previously suggested correlation between Ly $\alpha$  absorption linewidth (also called Doppler  $b$ -parameter) and impact parameter ( $\rho$ ), observing that the broadest lines (FWHM  $> 150 \text{ km s}^{-1}$ ) are only seen within 350 kpc of a galaxy, while only narrower lines (FWHM  $< 75 \text{ km s}^{-1}$ ) are found at  $\rho > 1 \text{ Mpc}$  (see Figure 1.3). The more recent COS-Halos survey (Tumlinson et al. 2013 and references therein) studied both the H I and low-to-medium ionization state metals CGM around  $\sim L^*$  galaxies, and found that H I is detected nearly ubiquitously within  $\sim 150$  kpc of both star-forming and passive galaxies, with metal absorption lines also detected in the majority of cases but with a stronger dependence on galaxy type (e.g., Tumlinson et al. 2011; Werk

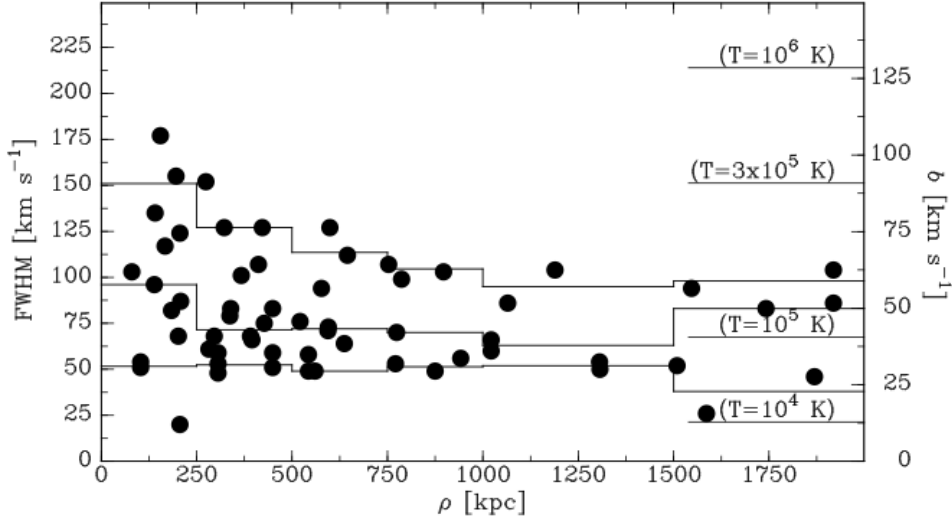


**Figure 1.3 :** The linewidth (or Doppler  $b$ -parameter) and FWHM of Ly $\alpha$  absorbers as a function of physical impact parameter to the nearest galaxy. Histograms show the 10th, 50th, and 90th percentiles of the distribution. See Wakker & Savage (2009).

et al. 2013).

In addition, studying the enrichment of galaxy halos is necessary for constraining outflow models and informing stellar feedback prescriptions. Directly measuring the velocity field and column densities of absorbers as a function of impact parameter and orientation around galaxies would provide the clearest evidence of inflow or outflow activity, but results are few and uncertain. Kacprzak et al. (2011b) claim to find that Mg II equivalent widths correlate with galaxy inclination but Mathes et al. (2014) find no such correlation for Ly $\alpha$  and O VI absorbers. Furthermore, we should expect outflowing gas to be more highly enriched and trace the metallicity of the associated galaxy, with inflowing gas instead appearing only in H I. Both Stocke et al. (2013) and Liang & Chen (2014) find an “edge” to heavy ion absorption at  $\sim 0.5R_{\text{vir}}$ , but with Ly $\alpha$  covering fractions of  $\sim 0.75 - 1$  continuing out to  $R_{\text{vir}}$ . However, Mathes et al. (2014) measure O VI absorption out to  $\sim 3R_{\text{vir}}$ .

All these previous studies have suffered from small sample sizes (most with fewer than 50 systems), and incompleteness due to their higher mean redshifts where it is increasingly difficult to detect faint galaxies surrounding absorption systems. This thesis aims to address some of these issues by compiling the largest-yet survey of Ly $\alpha$  absorbers spread across a range of environments, and both near and far from galaxies. The installation of the Cosmic Origins Spectrograph (COS; Green et al. 2012) on the *Hubble Space Telescope* (*HST*) has opened up a new era for studying intergalactic gas via UV QSO-absorption lines, as COS is able to observe fainter targets than ever before with high signal to noise and velocity resolution. Over 700 QSOs have now been observed with COS, most of which have good quality data covering the Ly $\alpha$  transition in the nearby Universe ( $cz \leq 10,000 \text{ km s}^{-1}$ ), where the existing galaxy data is also good and relatively complete to  $\sim 0.1L^*$  on average.

This project aims to take advantage of all this existing data to study the Ly $\alpha$  traced CGM in the local universe with a survey of unprecedented size. In Chapter 1 I describe the compilation of a new nearby galaxy catalog to take advantage of the existing galaxy data. This catalog is then correlated with the over 700 archival QSO targets observed by the Cosmic Origins Spectrograph (COS) on the Hubble Space Telescope (HST) to produce a sample of galaxy-absorption line systems including a range of galaxy environments, orientations, and types. In the following section I summarize the 3 major questions this thesis aims to tackle with the resulting dataset.

## 1.2 Science Goals

While there are numerous open questions concerning the interactions of galaxies and the gas that surrounds them, this thesis focuses on the following:

### 1.2.1 Galaxy Proximity

*How strongly is intergalactic gas concentrated near galaxies, and does the presence of galaxies affect the physical properties of absorbers?* Recent studies find that half of all Ly $\alpha$  absorbers lie within galaxy halos, at impact parameters of  $\rho < 350$  kpc and within  $400 \text{ km s}^{-1}$  of a galaxy (e.g., Côté et al. 2005; Prochaska et al. 2006; Wakker & Savage 2009). Furthermore, Sorini et al. (2018) find that the “sphere of influence” of galaxy can extend all the way to  $\sim 2$  Mpc, far more distant than the  $\sim 150$  kpc or  $\sim 1R_{\text{vir}}$  often used as the search radius for CGM studies. However, this may just be an effect of galaxies being embedded in filaments, and not necessarily evidence of the influence of the galaxies themselves. The properties of the lines also appear to change with impact parameter. For example, it has been known for some time that higher column density absorption is found closer to galaxies, and there is good evidence that the same is true for absorption linewidth (e.g., Wakker & Savage 2009; Prochaska et al. 2011). However, it remains unclear which physical process is responsible; increased turbulence, temperature, ionizing radiation field, or an effect of velocity gradients or blending of multiple cloudlets along the line of sight. Studying this phenomenon as a function of environment with good understanding of the properties, morphologies, and group memberships of the nearby galaxies is the clearest way forward on this question, and a larger statistical sample than previously employed will be required.

### 1.2.2 Galaxy Orientation

*Do the physical properties of absorbers depend on their orientation with respect to nearby galaxies?* Recent results suggest that absorbing systems have a preferred orientation with respect to the major and minor axes of the galaxies they are near to (e.g., Kacprzak et al. 2011b, 2012). This could be evidence of inflows and outflows, an effect of the global

structure of galaxy halos, or a signature of a preferred orientation of galaxy halos within Cosmic Web filaments. Unfortunately the statistics are not yet good enough to distinguish between these possible scenarios. Additionally, very few authors (see, e.g., Mathes et al. 2014; Bordoloi et al. 2014) have investigated the dependence of absorber properties on nearby galaxy *inclination*, the results of which could have important implications for galaxy halo shape and the spatial dependence of halo gas covering fractions. A large-scale study into the inclination and azimuth angle dependence of absorption is the clearest path forward here.

### 1.2.3 Galaxy Rotation

*Does intergalactic gas “know” about the rotation of the galaxies embedded within it?*

In particular we would like to know how far out (or to what impact parameter) the rotational curves of galaxies extend, or in other words what angular momentum information is retained by galaxy halos. Galaxy disks are built via accretion of material from the IGM, which carries with it angular momentum. This angular momentum must eventually contribute to the disk rotation, so it is reasonable to expect the overall rotation signature of halo gas to trace that of the more readily measured disk gas rotation. Indeed, the simulations of Stewart et al. (2011a,b, 2013) predict that H I gas out to at least  $1R_{\text{vir}}$  should co-rotate with galaxies, and furthermore that absorption lines in QSO sightlines should be able to accurately trace this (see Figure 1.4; a simulated galaxy halo showing coherent halo gas rotation from Stewart et al. 2011a). Previous studies (e.g., Steidel et al. 2002; Côté et al. 2005; Wakker & Savage 2009; Kacprzak et al. 2011a) were unable to find a clear correlation between the rotation of galaxy disks and the kinematics of nearby absorbers. However, none of these previous studies have been able to produce a sample of more than a handful of systems, and have only considered the possibility of an extended, warped stellar disk in their analysis. A

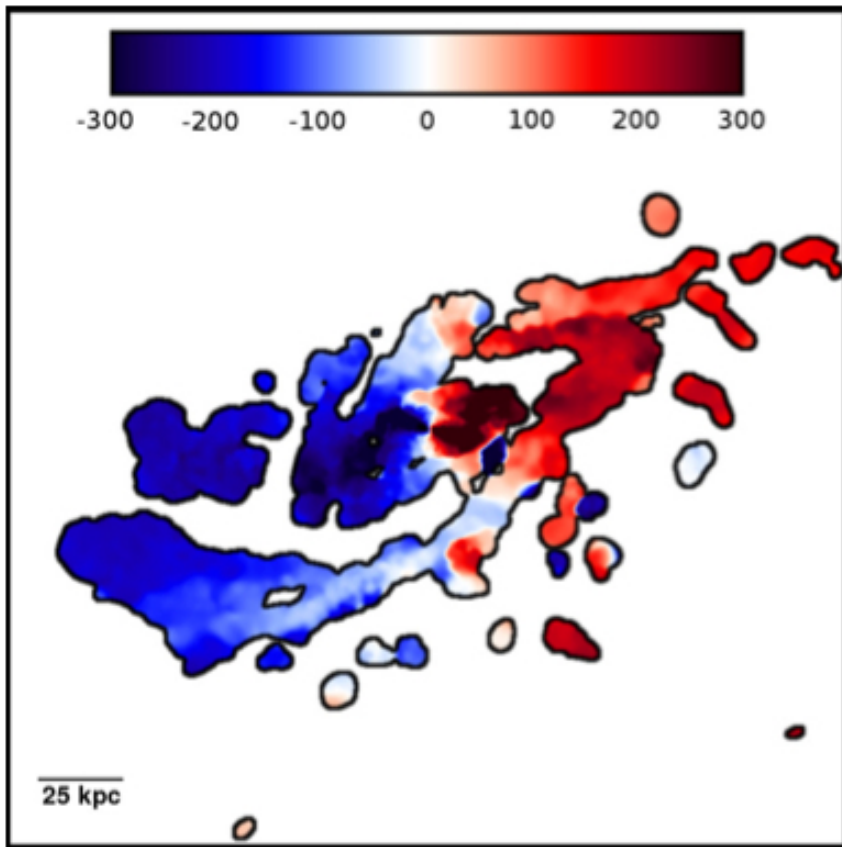


**Figure 1.4 :** A simulated galaxy halo showing the coherent co-rotation of halo gas out at least 100 kpc from the inner disk (the galaxy disk is seen in dark blue and red at the image center; see Stewart et al. (2011a)).

targeted observational campaign for easily observed galaxies in the local Universe could make substantial progress here.

### 1.3 Summary of Thesis

In the following chapters I describe a program to observationally explore the connections between low column density Ly $\alpha$  absorption and the galaxy environment in the local Universe. This program focuses mainly on archival QSO observations taken by the Cosmic Origins Spectrograph (COS) on the Hubble Space Telescope (HST), and correla-

tions between the locations of detected Ly $\alpha$  absorption and of galaxies larger than  $\sim 0.1L^*$ . By restricting our study to low-redshifts ( $cz \leq 10,000 \text{ km s}^{-1}$ ) we are able to compile a dataset of unparalleled size while remaining highly complete to galaxies of all types, sizes, and distances from absorption detections. The results of this thesis are presented as follows:

1. In Chapter 1 I present a new nearby galaxy catalog. In order to study the CGM-galaxy connection on a large, all-sky scale, we rely heavily on archival, publicly available data for the positions and properties of the galaxies. We describe the retrieval, handling, homogenization and completeness of these data, as well as detailed descriptions of each included galaxy property (i.e., the catalog columns).
2. In Chapter 2 I present the results of a pilot study with 33 QSO sightlines chosen for their proximity to large galaxies ( $D \geq 25 \text{ kpc}$ ). We introduce a new method for absorber-galaxy matching called the likelihood-method, which will make it possible to algorithmically study our large final data set. Using this likelihood-method we match 48 Ly $\alpha$  absorption lines with nearby large galaxies, and study the absorption strength (EW) as a function of velocity and spatial separation, azimuth angle and inclination. We find that the strongest absorbers are all found within  $100 \text{ km s}^{-1}$  of a galaxy, and that there exists an overabundance of detections near highly inclined galaxies ( $inc \gtrsim 50^\circ$ ). We attribute this overabundance to the effect of flattened, non-spherical galaxy halos on the detection probability as a function of impact parameter.
3. In Chapter 3 I present the results of a study of the kinematic connection between galaxy disks and Ly $\alpha$ -traced halo gas. We have compiled a sample of 29 galaxies with known rotation curves both from the literature and from new observations with the Southern African Large Telescope (SALT) which also appear within  $3R_{\text{vir}}$  of a COS QSO sightline. We compare the galaxy disk kinematics to the velocities of

$\text{Ly}\alpha$  absorption lines detected in 19 nearby QSO sightlines with the help of custom cylindrical and NFW-based halo rotation models (Navarro et al. 1996, 1997). We find that the co-rotation fraction of absorbers declines as a function of galaxy luminosity, which we attribute to the effect of cold-mode accretion dominating in lower-mass galaxy halos.

4. In Chapter 4 I present the results of our full CGM survey, which includes 1135  $\text{Ly}\alpha$  absorbers detected in the spectra of 264 QSO spectra. We explore the effect of different normalizations to our likelihood-method for absorber-galaxy matching, and use this technique to split absorber-galaxy systems into 5 different bins based on their galaxy environments. We find that both absorption strength (EW) and linewidth (Doppler  $b$ -parameter) are enhanced with proximity to a single galaxy, and further enhanced by proximity to multiple galaxies. We also detect a bimodal azimuth distribution, with  $\text{Ly}\alpha$  absorbers preferentially found slightly offset from both the minor and major galaxy axes. We confirm the inclination results first suggested in Chapter 2.
5. In Chapter 5 I summarize the results of this thesis, and place these results in the broader context of the circumgalactic medium and its implications for global galaxy evolution.

## References

- Bordoloi, R., Lilly, S. J., Kacprzak, G. G., & Churchill, C. W. 2014, ApJ, 784, 108  
 Bowen, D. V., Pettini, M., & Blades, J. C. 2002, ApJ, 580, 169  
 Chen, H.-W., Lanzetta, K. M., Webb, J. K., & Barcons, X. 1998, ApJ, 498, 77  
 —. 2001, ApJ, 559, 654

- Côté, S., Wyse, R. F. G., Carignan, C., Freeman, K. C., & Broadhurst, T. 2005, *ApJ*, 618, 178
- Danforth, C. W., Keeney, B. A., Tilton, E. M., et al. 2016, *ApJ*, 817, 111
- Erb, D. K. 2008, *ApJ*, 674, 151
- Frieman, J. A., Turner, M. S., & Huterer, D. 2008, *ARA&A*, 46, 385
- Fukugita, M., & Peebles, P. J. E. 2006, *ApJ*, 639, 590
- Green, J. C., Froning, C. S., Osterman, S., et al. 2012, *ApJ*, 744, 60
- Kacprzak, G. G., Churchill, C. W., Barton, E. J., & Cooke, J. 2011a, *ApJ*, 733, 105
- Kacprzak, G. G., Churchill, C. W., Evans, J. L., Murphy, M. T., & Steidel, C. C. 2011b, *MNRAS*, 416, 3118
- Kacprzak, G. G., Churchill, C. W., & Nielsen, N. M. 2012, *ApJL*, 760, L7
- Lanzetta, K. M., Bowen, D. V., Tytler, D., & Webb, J. K. 1995, *ApJ*, 442, 538
- Liang, C. J., & Chen, H.-W. 2014, *MNRAS*, 445, 2061
- Mathes, N. L., Churchill, C. W., Kacprzak, G. G., et al. 2014, *ApJ*, 792, 128
- Navarro, J. F., Frenk, C. S., & White, S. D. M. 1996, *ApJ*, 462, 563
- . 1997, *ApJ*, 490, 493
- Oort, J. H. 1966, *Bull. Astron. Inst. Netherlands*, 18, 421
- . 1969, *Nature*, 224, 1158
- . 1970, *A&A*, 7, 381
- Prochaska, J. X., Weiner, B., Chen, H.-W., Mulchaey, J., & Cooksey, K. 2011, *ApJ*, 740, 91
- Prochaska, J. X., Weiner, B. J., Chen, H.-W., & Mulchaey, J. S. 2006, *ApJ*, 643, 680
- Prochaska, J. X., & Wolfe, A. M. 2009, *ApJ*, 696, 1543
- Rudie, G. C., Steidel, C. C., Trainor, R. F., et al. 2012, *ApJ*, 750, 67
- Shull, J. M. 2014, *ApJ*, 784, 142
- Sorini, D., Oñorbe, J., Hennawi, J. F., & Lukić, Z. 2018, *ApJ*, 859, 125
- Steidel, C. C., Erb, D. K., Shapley, A. E., et al. 2010, *ApJ*, 717, 289
- Steidel, C. C., Kollmeier, J. A., Shapley, A. E., et al. 2002, *ApJ*, 570, 526

- Stewart, K. R., Brooks, A. M., Bullock, J. S., et al. 2013, *ApJ*, 769, 74
- Stewart, K. R., Kaufmann, T., Bullock, J. S., et al. 2011a, *ApJL*, 735, L1
- . 2011b, *ApJ*, 738, 39
- Stocke, J. T., Keeney, B. A., Danforth, C. W., et al. 2013, *ApJ*, 763, 148
- Thom, C., Tumlinson, J., Werk, J. K., et al. 2012, *ApJL*, 758, L41
- Tinsley, B. M., & Danly, L. 1980, *ApJ*, 242, 435
- Tinsley, B. M., & Larson, R. B. 1978, *ApJ*, 221, 554
- Tripp, T. M., Lu, L., & Savage, B. D. 1998, *ApJ*, 508, 200
- Tumlinson, J., Thom, C., Werk, J. K., et al. 2011, *Science*, 334, 948
- . 2013, *ApJ*, 777, 59
- Wakker, B. P., Hernandez, A. K., French, D. M., et al. 2015, *ApJ*, 814, 40
- Wakker, B. P., & Savage, B. D. 2009, *ApJS*, 182, 378
- Wakker, B. P., Howk, J. C., Savage, B. D., et al. 1999, *Nature*, 402, 388
- Werk, J. K., Prochaska, J. X., Thom, C., et al. 2013, *ApJS*, 204, 17

## Chapter 2

A Catalogue of Nearby ( $cz \leq 10,000 \text{ km s}^{-1}$ )

Galaxies

*To be submitted to the Astrophysical Journal*

## Abstract

We present an all-sky catalogue of galaxies with recession velocity  $cz \leq 10,000 \text{ km s}^{-1}$ .

We used published data available through the NASA Extragalactic Database (NED), the NASA/IPAC Infrared Science Archive (IRSA), the Third Reference Catalogue of Bright Galaxies (RC3), and the Tully (2015) 2MASS galaxy group catalogue. We homogenized the combined dataset by converting diameter measurements to 2MASS values, and employing outlier rejection to choose representative values for position angle, inclination, redshift-independent distance, and  $B$ -band magnitude. We use these values to estimate galaxy  $B$ -band luminosities.

## 2.1 Introduction

Galaxy catalogues form the basis for all studies of the nearby universe, as they are needed to create representative samples, study the distribution of galaxies, among many other things. The ideal solution of an all-sky and all-object online database containing homogenized information has not been completely realized, even as the NASA Extragalactic Database (NED)<sup>1</sup>, Vizier<sup>2</sup>, SIMBAD<sup>3</sup> and others approach some of these requirements. Each of these databases offer slightly different sets of information on their objects, and there is often no straightforward way for extracting all the parameters needed. Moreover, these aggregation sites typically contain all published parameters with no judgment of their quality. For example, there is no way to return the diameters of all known galaxies in a particular redshift range. Furthermore, comparing and choosing between disparate measurements of common galaxy parameters (e.g., diameter, inclination, magnitude, distance, etc.) is not trivial when a large sample is required. The need for a simple, highly complete easy-lookup nearby galaxy catalogue remains.

For our studies of the circumgalactic medium (CGM) around galaxies in the nearby universe we required just such a galaxy dataset, with a high degree of completeness and homogeneity. Therefore we have constructed a catalogue of galaxies within the redshift range  $cz \leq 10,000 \text{ km s}^{-1}$ . All of the data included here is publicly available through the NASA Extragalactic Database (NED), the NASA/IPAC Infrared Science Archive (IRSA), the Third Reference Catalogue of Bright Galaxies (RC3; Corwin et al. 1994), and the Tully

---

<sup>1</sup><https://ned.ipac.caltech.edu/>

<sup>2</sup><http://vizier.u-strasbg.fr/>

<sup>3</sup><http://simbad.u-strasbg.fr/simbad/>

(2015) 2MASS Galaxy Group Catalog. We have endeavored in various ways to create a single, homogeneous catalogue. The largest effort on this front revolved around deriving consistent linear and angular galaxy diameters. While we originally began compiling this data base as a tool to aid in the matching of galaxies to absorption detected in background QSO spectra, we hope that it can prove useful to the community at large.

In Section 2 we discuss our data retrieval methods and handling of distance and velocity measurements. In Section 3, we provide explanation and details for each galaxy attribute included in the catalogue (i.e., the data columns). We discuss caveats and limitations in Section 4. Throughout this catalogue we have adopted the cosmology  $H_0 = 71 \text{ km s}^{-1} \text{ Mpc}^{-1}$ ,  $\Omega_m = 0.27$ , and  $\Omega_\Lambda = 0.73$  when converting recession velocities into distances.

## 2.2 Data

### 2.2.1 Data Retrieval

All data contained in this catalogue *except* for extinction, RC3 parameters, and group membership were retrieved from NED. Our criterion for including a galaxy in this dataset is only a published redshift which places the galaxy in the  $cz \leq 10,000 \text{ km s}^{-1}$  velocity range. These data were retrieved from NED in a two-step process. First, we used the NED “Search By Parameters” service to retrieve all objects with classification type “Galaxies (G)” and heliocentric velocity  $\leq 10,000 \text{ km s}^{-1}$ . Because of a 10,000 object retrieval cap imposed by NED, this step was completed in 14 separate redshift steps. Next, we used the retrieved list of object names to query NED for more detailed information than is available through the initial search. We completed this query using a suite of custom Python scripts which retrieve the object’s XML VOTable, which contains *all* object information

and measurements contained in NED.

We then retrieved the Galactic dust extinction ( $E(B - V)$ ) estimates produced by Schlafly & Finkbeiner (2011) toward each object from the Galactic Dust Reddening and Extinction service hosted by the NASA/IPAC Infrared Science Archive (IRSA)<sup>4</sup>. Again, this took several steps because of the 20,000 row limit imposed by the Table Upload mode offered by IRSA. Group information (membership; §2.3.46, number of members; §2.3.47, and group distance; §2.3.48) for each galaxy was taken from the 2MASS Galaxy Group Catalogue Tully (2015). Finally, we also include the galaxy type (§2.3.42), position angle (§2.3.45), apparent major isophotal diameter (§2.3.43), and major-to-minor axis ratio (§2.3.44) from the Third Reference Catalogue of Bright Galaxies (RC3; §Corwin et al. 1994) for the 18,601 galaxies in this catalogue.

### 2.2.2 Completeness

The galaxy dataset contains 130,819 objects, and includes data from SDSS, 2MASS, 2dF, 6dF, RC3, and many other, smaller surveys. Figure 2.1 shows the number of objects as a function of luminosity in four bins of heliocentric velocity, and Figure 2.2 shows the number of objects coming from each of the major included surveys as a function of heliocentric velocity.<sup>5</sup> Our restricted velocity range of  $cz \leq 10,000 \text{ km s}^{-1}$  leads to a completeness limit of  $B \lesssim 18.7$  mag, or  $\sim 0.2L^*$ , at  $cz = 10,000 \text{ km s}^{-1}$ , and progressively better towards lower velocities (see Figure 2.1). This limit will vary depending on which major surveys include a particular region of the sky. The major contributor is whether

---

<sup>4</sup><http://irsa.ipac.caltech.edu/applications/DUST/>

<sup>5</sup>The peak for “other sources” between  $2500 \lesssim v_{\text{hel}} \lesssim 3100 \text{ km s}^{-1}$  in Figure 2.2 is due to the small (1.3 square degrees) ultra-deep Subaru/XMM-Newton Deep Sky Survey (SXDS), which reaches a  $B$ -band magnitude limit of  $B = 28.2$ . See <https://www.naoj.org/Science/SubaruProject/SXDS/>

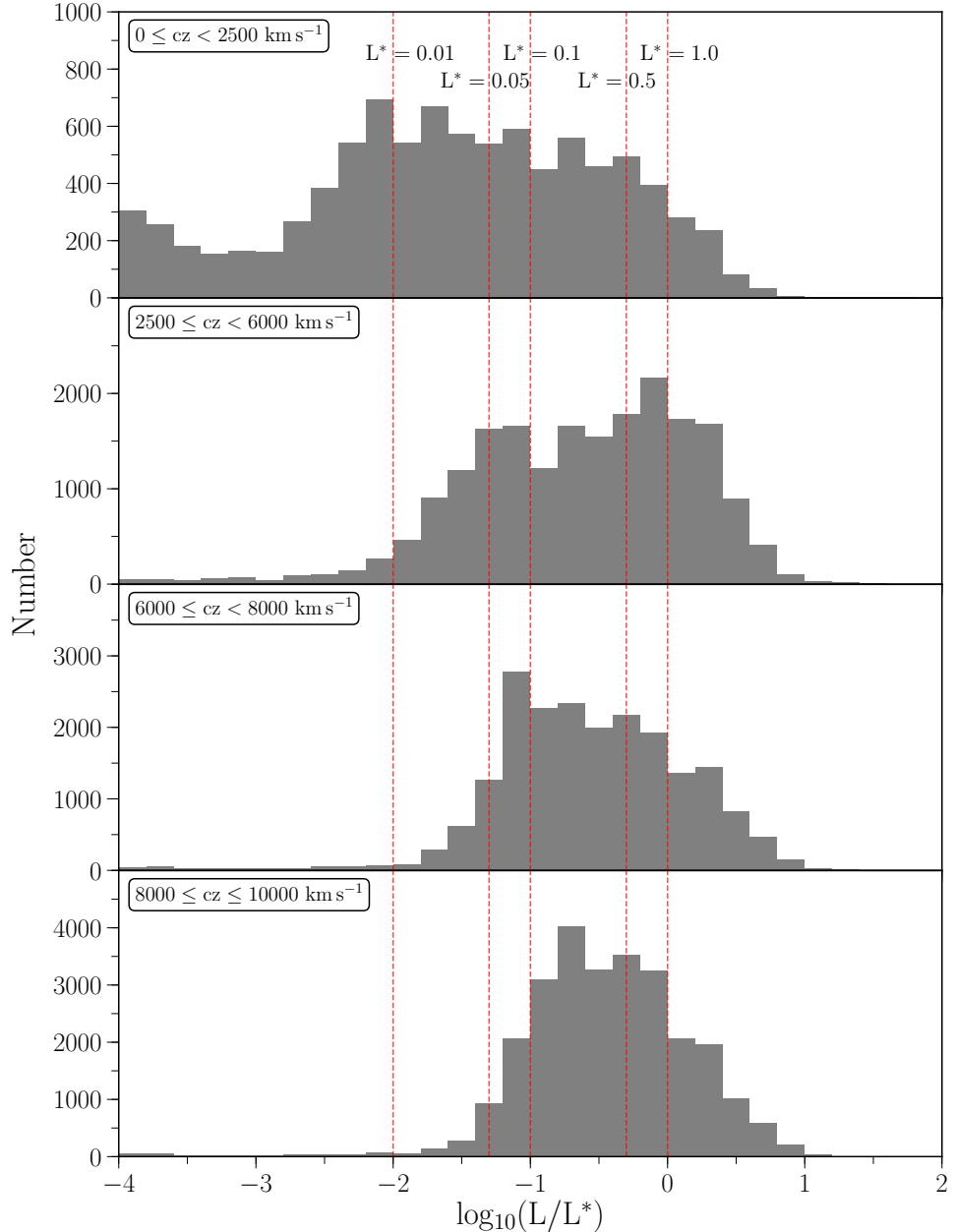


**Figure 2.1 :** Distribution of  $L/L^*$  values for all galaxies in the dataset. Black vertical lines highlight  $1$ ,  $0.5$ ,  $0.1$ ,  $0.05$  and  $0.01 L^*$ . The turnoff in the distribution for each region reveals the corresponding completeness. We are highly complete to  $0.01 L^*$  out to  $2500 \text{ km s}^{-1}$ ,  $0.05 L^*$  between  $2500 \leq cz \leq 5000 \text{ km s}^{-1}$ ,  $0.1 L^*$  between  $6000 \leq cz \leq 8000 \text{ km s}^{-1}$ , and  $0.3 L^*$  between  $8000 \leq cz \leq 10000 \text{ km s}^{-1}$ . See §3.1 for a discussion of these limits.

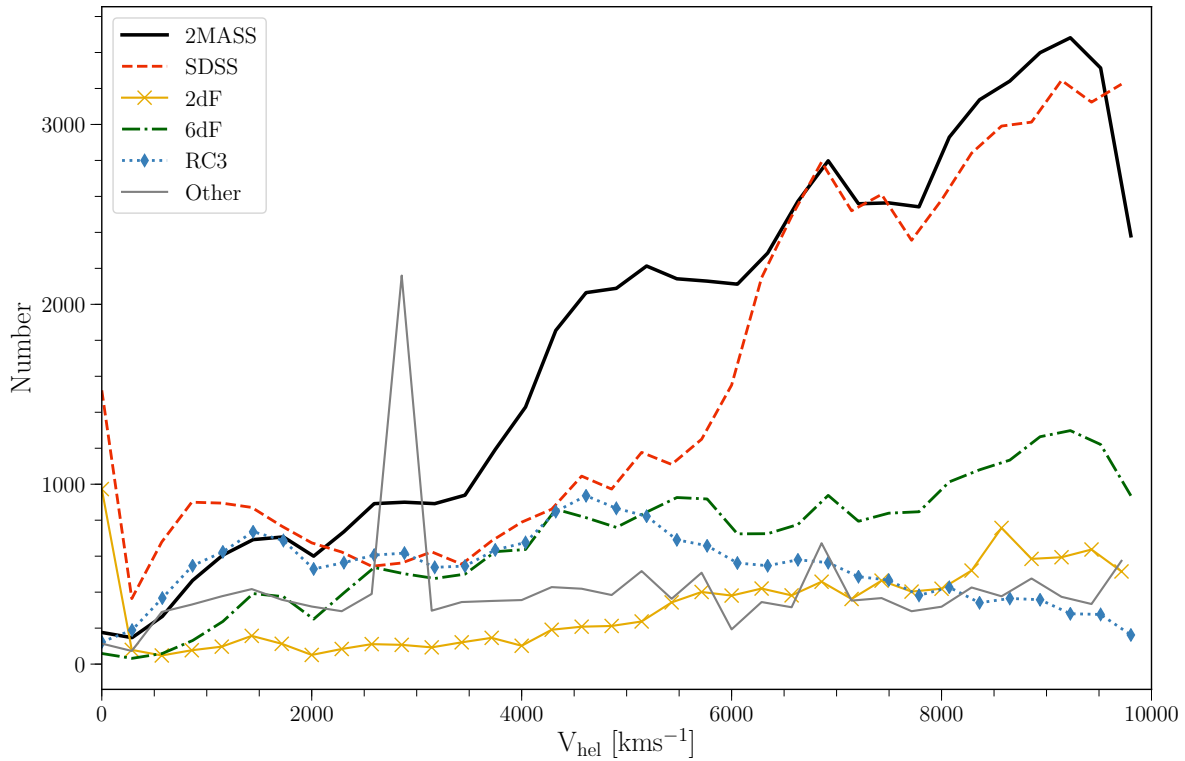


**Figure 2.2 :** Number of objects included from the major sources 2MASS (solid-black), SDSS (dashed-red), 2dF (solid-gold-crosses), 6dF (dot-dashed-green), RC3 (dotted-diamond-blue) and all other sources (solid-grey) plotted as a function of heliocentric velocity. The peak for “other sources” between  $2500 \lesssim v_{\text{hel}} \lesssim 3100 \text{ km s}^{-1}$  is due to the small (1.3 square degrees) ultra-deep Subaru/XMM-Newton Deep Sky Survey (SXDS), which reaches a *B*-band magnitude limit of  $B = 28.2$ .

or not SDSS data is available, which begins around  $cz = 5,000 \text{ km s}^{-1}$ . Figure 2.1 is split into 4 velocity bins to illustrate this. Our data has a high degree of completeness down to  $\sim 0.01L^*$  in the first bin,  $0 \leq cz \leq 2,500 \text{ km s}^{-1}$ . At slightly higher velocity,  $2500 \leq cz \leq 6000 \text{ km s}^{-1}$ , the completeness falls a bit, but is still rather complete to  $\sim 0.05L^*$  as we move past the near and well studied galaxies, but have yet to reach the footprint of deep all sky surveys. SDSS data becomes available in the last two bins,

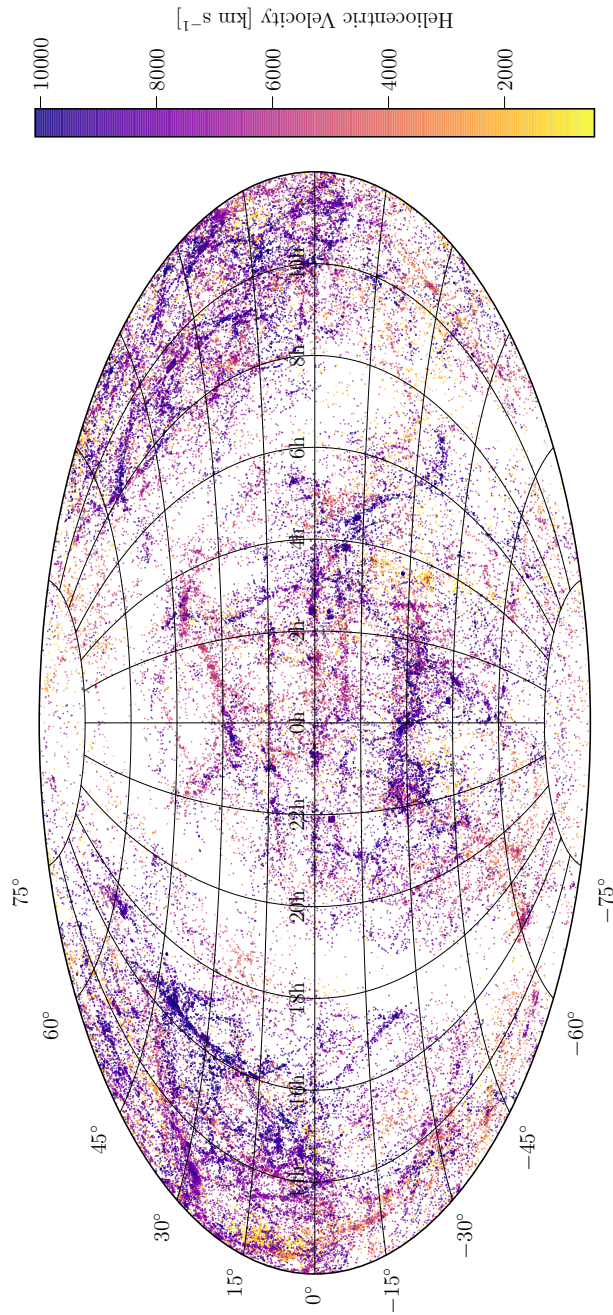


**Figure 2.3 :** The positions of all galaxies with  $flag = 0$  (see 2.3.50 below) plotted in Aitoff projection and colored according to heliocentric velocity. We include 3 maps, centered here at R.A. = 0h. See below for R.A. = 6h and R.A. = 12h centered maps.

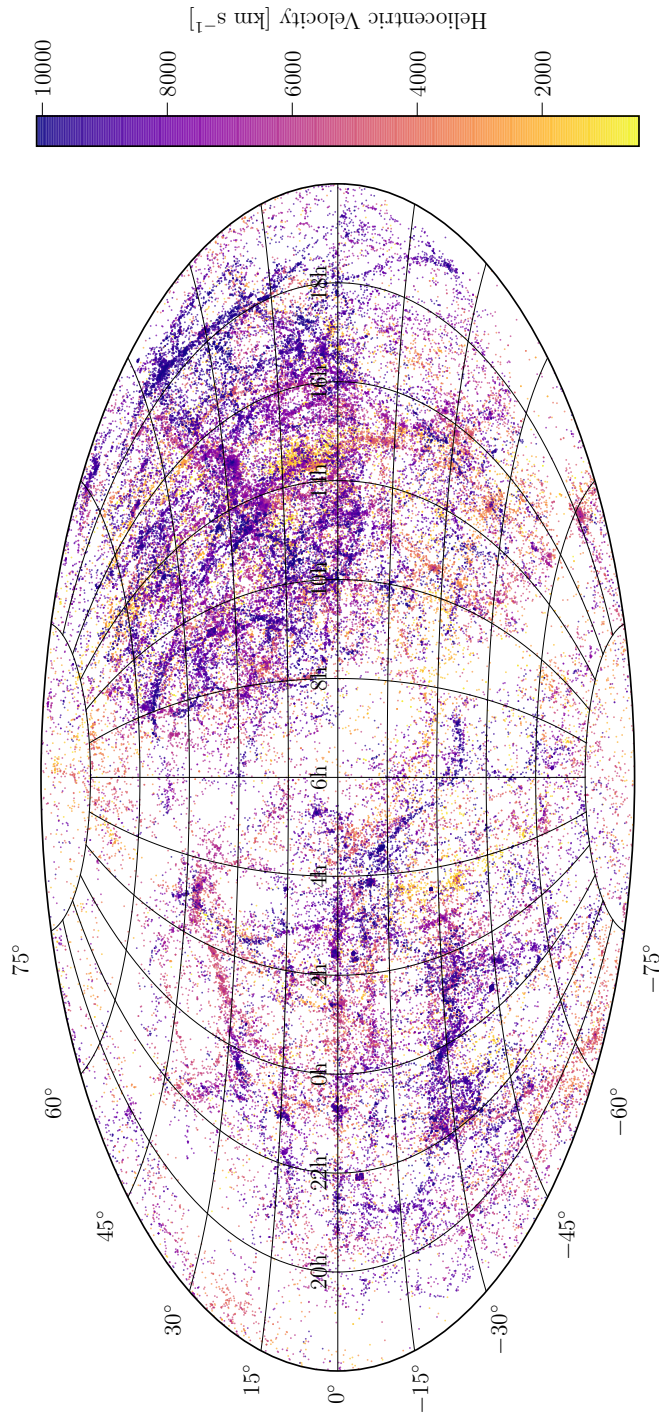


**Figure 2.3 :** The positions of all galaxies with  $flag = 0$  (see 2.3.50 below) plotted in Aitoff projection and colored according to heliocentric velocity. We include 3 maps, centered here at R.A. = 6h. See above and below for R.A. = 0h and R.A. = 12h centered maps.

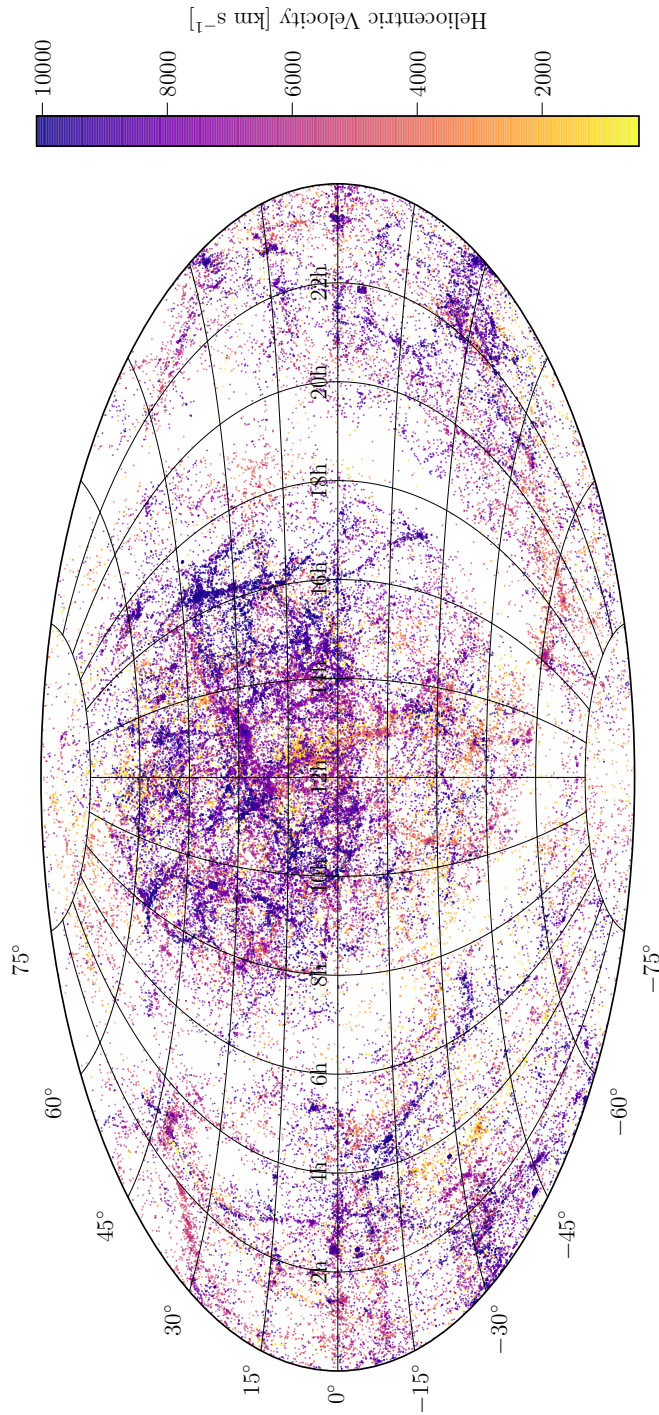


**Figure 2.3 :** The positions of all galaxies with  $flag = 0$  (see 2.3.50 below) plotted in Aitoff projection and colored according to heliocentric velocity. We include 3 maps, centered here at R.A. = 12h. See above for R.A. = 0h and R.A. = 6h centered maps.

spanning  $6000 \leq cz \leq 10,000 \text{ km s}^{-1}$ , and correspondingly completeness remains high down to the SDSS limits of  $B \lesssim 18.7$  mag, or  $\sim 0.2L^*$  at  $cz = 10,000 \text{ km s}^{-1}$ .

Additionally, we note the presence of a long super-faint tail to the distribution in the low velocity bin ( $0 \leq cz \leq 2,500 \text{ km s}^{-1}$ ). This is due to a number of pointed, ultra-deep surveys which have picked up faint dwarfs in the very local universe, which then quickly exit the observability window past  $v_{\text{hel}} \sim 2500 \text{ km s}^{-1}$ . All luminosities are calculated as described below in §2.3.63.

## 2.3 The Catalogue

The following section describes the contents of each column in the order it appears in the catalogue. Null values are marked in one of three ways. Columns containing strings have the null value of 'x', those containing integers have null value '-99', and those containing floating point entries have null value '-99.99'. The following subsection numbers correspond to the column numbers in the catalogue (i.e., §2.3.1 is the first data column, §2.3.2 is the second, etc.).

### 2.3.1 Name

Our preferred name for the galaxy. If the galaxy is in one of the following base catalogues we adopt that name, in the order of preference given below. If the galaxy is not in one of these catalogues, we use the NED-preferred name (§2.3.2).

Name preferences: NGC, IC, UGC, UGCA, Mrk, SBS, Fairall, TOLOLO, Ton, ESO, Holm, MCG, CGCG, IRAS, IRASF, KISS, KISSR, Kaz, IZw, IIIZw, IIIIZw, IVZw, VZw, VIZw, VIIIZw, SDSS, 3C, PG, HE, HS, PKS, FCC, FGC, HCG, VCC, KUG, PGC, 2MASS, 2dF, 6dF.

### 2.3.2 NEDname

The preferred name for the galaxy in the NED database.

### 2.3.3 z

The NED-preferred redshift for the galaxy.

### 2.3.4 RAdeg

Equatorial right ascension coordinate in degrees (J2000.0 epoch).

### 2.3.5 DEdeg

Equatorial declination coordinate in degrees (J2000.0 epoch).

### 2.3.6 RAh

Equatorial right ascension hour coordinate (J2000.0 epoch).

### 2.3.7 RAM

Equatorial right ascension minute coordinate (J2000.0 epoch).

### 2.3.8 RAs

Equatorial right ascension second coordinate (J2000.0 epoch).

### 2.3.9 DE-

Equatorial declination coordinate sign (J2000.0 epoch).

### 2.3.10 DEd

Equatorial declination degree coordinate (J2000.0 epoch).

### 2.3.11 DEm

Equatorial declination minute coordinate (J2000.0 epoch).

### 2.3.12 DEs

Equatorial declination second coordinate (J2000.0 epoch).

### 2.3.13 GLON

Galactic longitude coordinate.

### 2.3.14 GLAT

Galactic latitude coordinate.

### 2.3.15 Vhel

Heliocentric radial velocity in  $\text{km s}^{-1}$  units. As done by NED, we do not make any relativistic correction to these velocities.

### 2.3.16 vcorr

Virgocentric flow-corrected velocity. Following Huchra & Geller (1982); Geller & Huchra (1983), this is calculated as

$$v_{\text{corr}} = v_{\text{hel}} + 300 * [\sin(\text{decl}) \sin(12^\circ.9333)$$

+

$$\cos(\text{decl}) \cos(12^\circ.9333) \cos(R.A. - 186^\circ.7833),$$

which corresponds to a velocity of  $300 \text{ km s}^{-1}$  toward  $R.A. = 186^\circ.7833$ ,  $\text{decl.} = 12^\circ.9333$ .

### 2.3.17 distvcorr

Distance calculated from  $v_{\text{corr}}$  with a Hubble constant of  $H_0 = 71 \text{ km s}^{-1} \text{ Mpc}^{-1}$ .

### 2.3.18 RID\_mean

Mean redshift-independent distance from the NED-D catalogue (Tully et al. 2009).

This is the arithmetic mean of the available measurements and therefore does not correspond to any single measurement in particular.

### 2.3.19 RID\_median

Median redshift-independent distance from the NED-D catalogue. This is not the arithmetic median of the set, but rather the published distance value *closest* to the median. The method used for this distance estimate is given by *distIndicator* (§2.3.25).

### 2.3.20 RID\_std

Standard deviation of all redshift-independent distance measurements.

### 2.3.21 RID\_min

Minimum published redshift-independent distance.

### 2.3.22 RID\_max

Maximum published redshift-independent distance.

### 2.3.23 bestDist

Our chosen best distance estimate. This is equal to *RID\_median* when a redshift-independent distance is available, and otherwise defaults to *distvcorr*. A redshift-independent distance estimate is available for 17,361 objects, which corresponds to 13.3% of all objects in the catalogue. For these objects *bestDist* is set to the median of all available redshift-independent distance estimates, and *e\_bestDist* (§2.3.24) is set to the published observational error for this median value. If no error is available, *e\_bestDist* is instead set to the standard deviation of all available redshift-independent distance measurements.

When only a redshift is available, we set *bestDist* equal to *distvcorr* (§2.3.17), which is the the Hubble law distance as calculated with  $H_0 = 71 \text{ km s}^{-1} \text{ Mpc}^{-1}$  and a Virgocentric flow-corrected velocity (*vcorr*; §2.3.16). The associated error, *e\_bestDist*, is then set to 10% of the resulting distance estimate. At very low redshift, the uncertainty in this estimate is dominated by deviations from the Hubble Flow due to, e.g., the Local Group, and at larger distances the uncertainty in  $H_0$  becomes dominant. The distance error for any particular galaxy is difficult to ascertain, but a 10% error should contain the true  $1\sigma$  error across our full redshift range. All galaxies with zero or negative *Vhel* have *bestDist* set to 1 Mpc, and *e\_bestDist* to 0.5 Mpc (unless a redshift-independent distance is available).

### 2.3.24 e\_bestDist

The error on *bestDist*. *e\_bestDist* is equal to *RID\_std* when a redshift-independent distance is available. Otherwise, *e\_bestDist* is set to 10% of *distvcorr* when *vcorr*  $\geq 0$ , and 50% of *distvcorr* if *vcorr*  $< 0$ .

### 2.3.25 distIndicator

A key indicating which method was used to measure the redshift-independent distance for this galaxy. Table 2.1 shows the keys and their corresponding full names as compiled in the NED-D distance catalogue. This key corresponds *only* to the *RID\_median* value.

### 2.3.26 MajDiam\_ang

Major axis diameter in units of arcsec. We have homogenized the galaxy data beyond the steps taken by NED by normalizing diameter measurements to 2MASS *K*-band values. Most galaxies in NED have measures of inclination, position angle and diameter available in several different bands, so in order to make more meaningful comparisons we choose one band for all measurements. We chose 2MASS values for this because it is an all-sky

Table 2.1. Distance Indicator Keys

Key	Distance Indicator	Key	Distance Indicator
AGB	AGB	MagEn	Magnetic energy
AGNtl	AGN time lag	Mag	Magnitude
Bstar	B Stars	Maser	Maser
BCG	BCG	MassM	Mass Model
BH	Black Hole	Miras	Miras
BLLum	BL Lac Luminosity	Novae	Novae
BSG	Blue Supergiant	OBstr	OB Stars
Brstr	Brightest Stars	OrMec	Orbital Mech.
Cstar	Carbon Stars	PAGB	PAGB Stars
Ceph	Cepheids	PNLF	PNLF
CMD	CMD	propM	Proper Motion
dCO	CO ring diameter	QS	Quasar spectrum
Dsigm	D-Sigma	Radio	Radio Brightness
Scuti	Delta Scuti	RClum	Red Clump
Diam	Diameter	DRing	Ring Diameter
dwEll	Dwarf Ellipticals	RRLyr	RR Lyrae
Dwarf	Dwarf Galaxy Diameter	RSV	RSV Stars
EclBi	Eclipsing Binary	RV	RV Stars
FJ	Faber-Jackson	SDorS	S Doradus Stars
FGLR	FGLR	SBF	SBF
GLens	G Lens	SGRB	SGRB
GCFP	GC FP	SNIa	SNIa
GCKJK	GC K vs. (J-K)	SNIIo	SNII optical
GCrad	GC radius	SNIIr	SNII radio
GCLF	GCLF	SNIas	SNIa SDSS
GCSBF	GC SBF	Stat	Statistical
gamma	GeV TeV ratio	Sosie	Sosies
GSGD	Grav. Stability Gas. Disk	subDw	Subdwarf fitting
GRB	GRB	SXPS	SX Phe Stars
HIod	H I + optical distribution	SZ	SZ effect
HIILF	HII LF	Terti	Tertiary
dHII	HII region diameter	TRGB	TRGB
HB	Horizontal Branch	TFest	Tully est
IRAS	IRAS	TF	Tully-Fisher
Jet	Jet Proper Motion	CepII	Type II Cepheids
LHbs	L(H $\beta$ )- $\sigma$	WD	White Dwarfs
LSB	LSB galaxies	WR	Wolf-Rayet
Mstar	M Stars		

Note. — Distance indicators and associated keys. Full descriptions can be found at <https://ned.ipac.caltech.edu/Library/Distances/distintro.html>

survey, and represents a large fraction of available galaxy data. Physical galaxy diameters are derived from 2MASS  $K_s$  “total” angular diameter measurements and galaxy distances. 2MASS  $K_s$  “total” diameter estimates are surface brightness extrapolation measurements and were derived by the 2MASS team as

$$r_{tot} = r' + a(\ln(148))^b, \quad (2.1)$$

where  $r_{tot}$  is defined as the point where the surface brightness extends to 5 disk scale lengths,  $r'$  is the starting point radius ( $> 5'' - 10''$  beyond the nucleus, or core influence), and  $a$  and  $b$  are Sersic exponential function scale length parameters ( $f = f_0 \exp(-r/a)^{(1/b)}$ , see Jarrett et al. 2003 for a full description). Approximately 50% of all the galaxies have this 2MASS  $K_s$  “total” diameter. Of the remainder, 20% have SDSS diameters, 3% have diameters from other surveys, and 27% have no published diameter.

For galaxies with multiple published measurements from different facilities, we have derived linear fits in order to convert between them. The orthogonal distance regression (ODR) algorithm as implemented by the Fortran code ODRPACK (and the Python wrapped version included in the Scipy package) was used to derive these best fits and their associated errors. ODR, compared to the more common linear regression algorithm, assumes errors in both x- and y-coordinates and thus minimizes the orthogonal distance between both dependent and independent data and the fit. We then ranked the available surveys in order of goodness of fit to 2MASS values. The fits for each survey are listed in Table 2.2.

A significant fraction of galaxies have irregular, incomplete, or otherwise suspect diameter data as published in NED. For example, some have 2MASS  $K_s$  “total” diameters available, but the published axis ratio (i.e., the ratio of minor to major axis) is either greater than 1, or otherwise significantly deviates from that found in other surveys. Furthermore,

often our highest ranking diameter survey has incomplete data (such as a missing axis ratio or position angle measurement). For our purposes we want to choose a single, representative value for each parameter. Our method for choosing this value is as follows: 1) we choose the highest ranking diameter measurement available, and choose the largest major-axis diameter value when multiple are available from the same facility, 2) we choose the highest ranking axes ratio, preferentially selecting the value from the measurement chosen in (1), but rejecting a ratio = 1 when the average ratio of all measurements is less than 1, 3) we choose the highest ranking position angle measurement, again preferentially selecting the value included in (1).

Finally, we check to see if our initial choices are outliers using a version of the Iglewicz-Hoaglin Method, a median absolute deviation algorithm (Iglewicz & Hoaglin 1993). This works by calculating the so-called “modified z-score” for each value,  $M_i$ , as follows:

$$M_i = \frac{0.6745(x_i - \tilde{x})}{MAD}, \quad (2.2)$$

where  $\tilde{x}$  is the median of the dataset, and MAD is the median absolute deviation. This modified z-score is then compared to a threshold to determine if  $x_i$  is an outlier or not. Through trial-and-error we set our outlier thresholds at 14.0 for major axis diameters, 3.5 for position angles, and 2.0 for axis ratios. Smaller threshold values indicate a stricter outlier rejection. If our initial choice of any of these values is flagged as an outlier, we choose the next highest-ranking, non-outlier value. The decision of diameter, ratio and position angle for each galaxy is included in the *diameter\_key* (2.3.39), *ratio\_key* (2.3.40), and *pa\_key* (2.3.41) columns.

Table 2.2. Summary of Diameter, Ratio, and P.A. Sources and Fits

Source of Data	Table Key	m	b	Diameter Total	Ratio Total	P.A. Total
K_s (2MASS “Total”)	K_2mass_tot	N/A	N/A	62945	53778	57990
K_s (LGA/2MASS “total”)	K_lga2mass_tot	N/A	N/A	593	497	553
K_s (2MASS isophotal)	K_2mass_iso	1.765 ± 0.003	1.31 ± 0.06	371	0	0
POSS1 103a-O	poss_103a-O	0.87 ± 0.01	17.60 ± 0.35	3466	5151	1513
POSS1 103a-E	poss_103a-E	1.05 ± 0.04	26.22 ± 1.98	121	341	1
ESO-LV “Quick Blue” IIa-O	eso_lv	0.81 ± 0.02	-9.73 ± 1.37	1442	4858	3167
r (SDSS Isophotal)	r_sdss_iso	1.03 ± 0.01	0.84 ± 0.17	26802	19726	25004
RC3 D_0 (blue)	rc3_d0	1.04 ± 0.01	-1.29 ± 0.58	277	0	0
RC3 D_25, R_25 (blue)	rc3_dr_25	1.11 ± 0.01	-3.09 ± 0.60	1	278	139
r (SDSS Petrosian)	r_sdss_petr	4.73 ± 0.03	3.38 ± 0.21	869	0	0
r (SDSS de Vaucouleurs)	r_sdss_dev	2.70 ± 0.04	15.64 ± 0.22	51	12302	7107
R (Kron-Cousins)	R_kron_cousins	1.47 ± 0.14	-35.89 ± 14.41	0	0	3
ESO-Uppsala “Quick Blue” IIa-O	eso_upp	1.06 ± 0.02	-13.39 ± 1.38	181	180	132

Note. — Diameter fits in order of preference. (1) The source name of the data given by NED. (2) The corresponding source key given in the catalogue. (3), (4) The slope and y-intercept of the ODR best fit with errors. (5), (6), (7) The total number of diameters, diameter ratios, and position angles coming from each source.

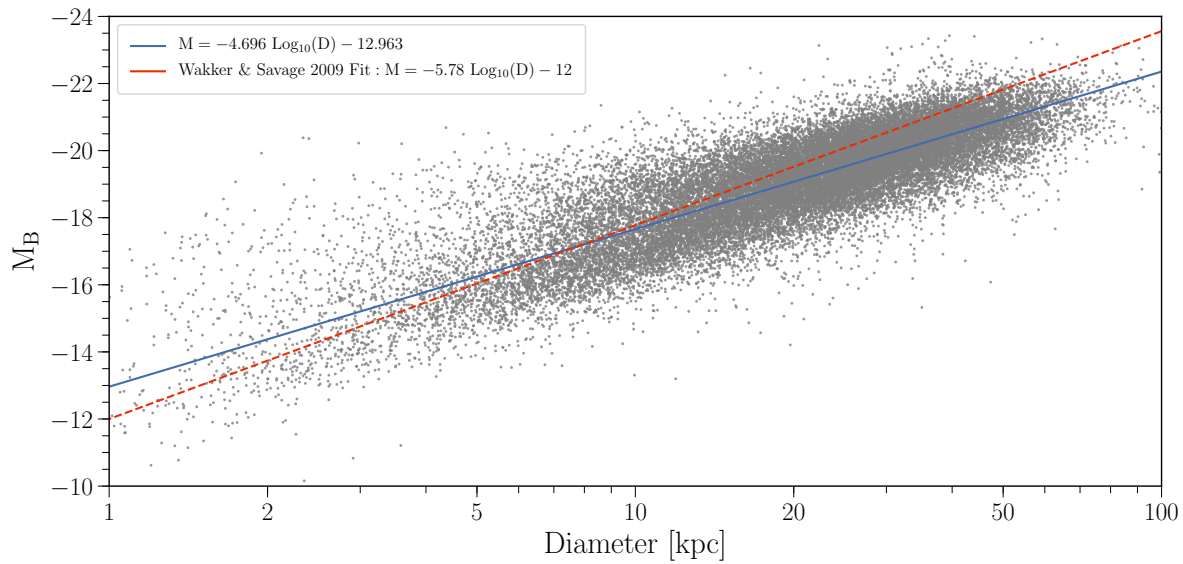


**Figure 2.4 :** Relationship between absolute  $B$ -band magnitude and physical diameter for all galaxies with available data. Data are in grey, and a least-squares fit is shown in blue. The function form of this fit is  $M = a \log_{10}(D) + b$ , with fit parameters  $a = -4.696 \pm 0.01$  and  $b = -12.963 \pm 0.01$ . We also include the fit derived by Wakker & Savage (2009) in dashed-red.

### 2.3.27 MinDiam\_ang

Minor axis diameter in units of arcsec. See 2.3.26 for a complete discussion.

### 2.3.28 e\_MajDiam\_ang

Major axis diameter error. This error is purely a result of the  $1\sigma$  fit error to K\_s (2MASS) values, and thus does not take into account any observational errors.

### 2.3.29 e\_MinDiam\_ang

Minor axis diameter error. This error is purely a result of the  $1\sigma$  fit error to K\_s (2MASS) values, and thus does not take into account any observational errors.

### 2.3.30 MajDiam

Linear major axis diameter in units of kpc, calculated using *bestDist*. See 2.3.26 for a complete discussion.

### 2.3.31 MinDiam

Linear minor axis diameter in units of kpc, calculated using *bestDist*. See 2.3.26 for a complete discussion.

### 2.3.32 e\_MajDiam

Linear major axis diameter error. This error is purely a result of the  $1\sigma$  fit error to K\_s (2MASS) values, and thus does not take into account any observational errors.

### 2.3.33 e\_MinDiam

Linear minor axis diameter error. This error is purely a result of the  $1\sigma$  fit error to K\_s (2MASS) values, and thus does not take into account any observational errors.

### 2.3.34 R\_vir

Virial radius estimate calculated as

$$\log R_{vir} = 0.69 \log D + 1.24. \quad (2.3)$$

This follows the parametrization of Stocke et al. (2013) relating a galaxy's luminosity to its virial radius, combined with the Wakker & Savage (2009) empirical relation between diameter and luminosity (see Wakker et al. 2015 and references therein for further details).

### 2.3.35 inc

Galaxy inclination calculated simply as  $inc = \cos^{-1}(MinDiam/MajDiam)$  in units of degrees.

### 2.3.36 adjustedInc

Galaxy inclination calculated assuming a finite disk thickness following Heidmann et al. (1972a):

$$\cos(i) = \sqrt{\frac{q^2 - q_0^2}{1 - q_0^2}}, \quad (2.4)$$

where  $q$  is the ratio of minor to major axes and  $q_0$  is the minimum disk thickness. We set  $q_0 = 0.2$  for all galaxies. This value is a compromise, as some galaxies (e.g., Sc type) will have intrinsic  $q_0$  closer to  $\sim 0.13$ , while highly bulged galaxies will have larger  $q_0$  (e.g., see Heidmann et al. 1972b). However, as morphologies are only available for a subset of galaxies, a generic inclination correction fits our need for homogeneity. The result is that very thin galaxies will be slightly biased towards higher inclination and vice-versa with thicker galaxies.

### 2.3.37 e\_inc

Inclination error derived from the error in major and minor axes fits (see 2.3.26). Measurement errors for diameters, axis-ratios, and position angles are inconsistently reported in NED, so this value only captures the additional error introduced by converting non-2MASS diameters. For consistency, we set 2MASS diameter errors uniformly at 5%.

### **2.3.38 PA**

Position angle in units of degrees. When multiple PA measurements are available for a given target, we choose the highest ranking measurement as outlined in 2.3.26.

### **2.3.39 diam\_key**

The chosen source of our diameter value. Published diameters are converted to an equivalent 2MASS  $K_s$  “total” value following the fits given in Table 2.2.

### **2.3.40 ratio\_key**

The chosen source of our diameter axis-ratio value. This is used to calculate the minor axis diameters and inclinations (see Table 2.2).

### **2.3.41 pa\_key**

The chosen source of our position angle value (see Table 2.2).

### **2.3.42 RC3\_type**

Galaxy morphology as published in the Third Reference Catalogue of Bright Galaxies (RC3; see Table 2 in Section 3.3.a, page 15, of the printed RC3; Corwin et al. 1994). Galaxies not included in RC3 are marked ‘x’.

### **2.3.43 RC3\_d25**

The RC3 apparent major isophotal diameter measured at the 25th magnitude surface-brightness level, in units of B-mag per arcsecond (see Section 3.4.a, page 21, of Volume I of the printed RC3; Corwin et al. 1994).

### **2.3.44 RC3\_r25**

The RC3 ratio of the major to minor axis isophotal diameter, converted from decimal logarithm to a straight ratio in order to match the units of *ratio\_key* (see Section 3.4.b, page 26, of Volume I of the printed RC3; Corwin et al. 1994).

### **2.3.45 RC3\_pa**

The RC3 position angle in units of degrees (see Section 3.5.a, page 30, of Volume I of the printed RC3; Corwin et al. 1994).

### **2.3.46 group\_num**

Group designation number taken from the Tully (2015) group catalogue.

### **2.3.47 group\_mem**

Number of members in this galaxy group taken from the Tully (2015) group catalogue.

### **2.3.48 group\_dist**

Distance to the galaxy group, taken from the Tully (2015) group catalogue.

### **2.3.49 MType**

Morphological type as homogenized by NED. We have removed extraneous space characters, and then replaced the individual spaces with underscore characters.

### **2.3.50 flag**

A flag to help identify suspected issues with a galaxy. For most objects *flag* = 0. If however, we suspect an object to be a star we set *flag* = 1. Our criteria for this is as follows:

- 1) if an object has  $V_{hel} < 500 \text{ km s}^{-1}$ , no diameter measurement, and no *MType* available,
- 2) if *MType* is found to match any of our exclude morphologies. Our full exclude list is

the following: [‘:’, ‘0.9’, ‘0.92’, ‘14.247’, ‘14.632’, ‘14.728’, ‘14.818’, ‘14.998’, ‘14’, ‘15.159’, ‘15.171’, ‘15.242’, ‘15.341’, ‘15.458’, ‘15.79’, ‘15.819’, ‘16.281’, ‘16.309’, ‘16.348’, ‘16.394’, ‘16.556’, ‘16.736’, ‘16.764’, ‘16.783’, ‘16.981’, ‘16’, ‘17.012’, ‘17.039’, ‘17.441’, ‘17.597’, ‘2\_compacts’, ‘2\_or\_3?\_spirals’, ‘2\_S0\_galaxies’, ‘2\_S0\_pec\_galaxies’, ‘2\_SB0?\_pec\_galaxies’, ‘2\_Spec?’, ‘2\_spirals’, ‘2\_symm.sp.arms’, ‘2E’, ‘2MASS\_Extended\_Ver.2’, ‘3\_S0\_galaxies’, ‘A-star’, ‘A’, ‘A0’, ‘A3\_HII’, ‘AGN:’, ‘AGN?’, ‘AGN’, ‘AGN+SF’, ‘AGN1’, ‘AGN2’, ‘ALG’, ‘Amorphous’, ‘B...’, ‘B’, ‘bright\_near\*’, ‘Cand.\_glob.\_cluster’, ‘Candidate\_AGN’, ‘Candidate\_PN’, ‘Carbon’, ‘D’, ‘DA-star’, ‘DA:’, ‘DA’, ‘DA\_auto’, ‘DA+M:;\_Cand.\_QSO’, ‘DA+M:’, ‘DA+M’, ‘DANS?’, ‘DANS?\_Sbrst’, ‘DANS’, ‘DANS\_WR?’, ‘DBA’, ‘DC:’, ‘DGTO’, ‘DISRPTD’, ‘DISTRBD’, ‘DQ;\_Cand.\_QSO’, ‘DQ:’, ‘DSa’, ‘F’, ‘F2’, ‘F6-F8;Candidate\_WD’, ‘High\_vel.\_cloud’, ‘K\_Star’, ‘K1’, ‘K4-K5;Candidate\_WD’, ‘M’, ‘M\_star’, ‘M\_Star’, ‘M0’, ‘M0V’, ‘M1’, ‘M3-M4’, ‘O’, ‘Opt.var.’, ‘Planetary’, ‘Planetary?’, ‘Planetary\_nebula’, ‘PN:’, ‘PN?’, ‘Point\_Src\_[SDSS]’, ‘Possible\_\*Cl’, ‘Possible\_star’, ‘star:’, ‘star??’, ‘star?’, ‘stellar-like’, ‘stellar:’, ‘stellar’,\_or\_galaxy’, ‘M-star’]

Secondly, we set  $flag = 2$  if the velocity implied by  $RID\_median$  (i.e.,  $RID\_median$  \*  $H_0$ ) differs from  $V_{hel}$  by more than  $1500 \text{ km s}^{-1}$ . If  $flag = 2$ , it may be wise to use  $distvcorr$  instead of  $bestDist$ . There is no overlap between flag types, so no possible stars ( $flag = 1$ ) objects have a redshift-independent distance available.

### 2.3.51 lumClass

Luminosity class as assigned by NED. Roman numerals between I, II, III, IV, and V designate galaxies in order of decreasing luminosity in an analogous fashion to the standard stellar luminosity classes.

### 2.3.52 E(B-V)

Galactic mean dust extinction in the direction of each galaxy from Schlafly & Finkbeiner (2011).<sup>6</sup>

### 2.3.53 Bmag

The median B-band magnitude. For each galaxy we retrieved all  $B$ -band and SDSS  $g$ ,  $r$ , and  $z$  measurements. Direct  $B$ -band measurements are available for  $\sim 30\%$  of galaxies, and a large fraction of the remaining objects have SDSS magnitudes. We convert SDSS magnitudes to  $B$ -band via  $B = g + 0.39(g - r) + 0.21$  (Jester et al. 2005). Per SDSS DR12 guidelines, we preferentially selected SDSS *petrosian* magnitudes when available, followed by *model* and *cmodel* values if *petrosian* was not available. We then selected the min, max and median  $B$ -band values when more than one was available for inclusion in the final data product. SDSS-converted  $B$ -band values are included as a separate estimate ( $Bmag_{sdss}$ ; §2.3.59).

### 2.3.54 Bmag\_key

The name of the source or catalog responsible for producing our chosen value of  $Bmag$ .

### 2.3.55 Bmag\_max

The brightest B-band magnitude available in NED for this object. See 2.3.53 for details.

---

<sup>6</sup>See <https://irsa.ipac.caltech.edu/applications/DUST/>

### **2.3.56 Bmag\_max\_key**

The name of the source or catalog responsible for producing  $Bmag\_max$ .

### **2.3.57 Bmag\_min**

The dimmest B-band magnitude available in NED for this object. See 2.3.53 for details.

### **2.3.58 Bmag\_min\_key**

The name of the source or catalog responsible for producing  $Bmag\_min$ .

### **2.3.59 Bmag\_sdss**

SDSS  $g$  and  $r$ -band measurements converted to  $B$ -band via  $B = g + 0.39(g - r) + 0.21$  (Jester et al. 2005). See 2.3.53 for details.

### **2.3.60 gmag\_sdss**

SDSS  $g$ -band magnitude. This value is used in the  $Bmag\_sdss$  calculation (see §2.3.53).

### **2.3.61 rmag\_sdss**

SDSS  $r$ -band magnitude. This value is used in the  $Bmag\_sdss$  calculation (see §2.3.53).

### **2.3.62 zmag\_sdss**

SDSS  $z$ -band magnitude (see §2.3.53).

### 2.3.63 Lstar\_med

The  $L/L^*$ ratio calculated using  $Bmag$  and  $bestDist$ . We compute luminosity in units of  $L^*$ for each of the min, median, max and SDSS  $B$ -band values as follows:

$$\frac{L}{L^*} = 10^{-0.4(M_B - M_{B^*})}, \quad (2.5)$$

where  $M_B$  is the galaxy absolute magnitude, calculated using the  $bestDist$  distance estimate as described above. We adopted the CfA galaxy luminosity function by (Marzke et al. 1994), which sets  $B^* = -19.57$ .

### 2.3.64 e\_Lstar\_med

$Lstar\_med$  error calculated with  $e\_Bmag$  and  $e\_bestDist$ . Combining these errors leads to the following error formula:

$$e\_Lstar\_med = 0.921\sqrt{10^{-0.8(M - M^*)}\Delta M^2}, \quad (2.6)$$

where  $\Delta m$  is the error in  $Bmag$ .

### 2.3.65 Lstar\_max

The  $L/L^*$ ratio calculated using  $B\_max$  and  $bestDist + e\_bestDist$  following Eq. 2.5.

### 2.3.66 e\_Lstar\_max

$Lstar\_max$  error calculated with  $e\_Bmag\_max$  and  $e\_bestDist$  (see §2.3.64).

### 2.3.67 Lstar\_min

The  $L/L^*$ ratio calculated using  $B\_min$  and  $bestDist - e\_bestDist$  following Eq. 2.5.

### 2.3.68 e\_Lstar\_min

*Lstar\_min* error calculated with *e\_Bmag\_min* and *e\_bestDist* (see §2.3.64).

### 2.3.69 Lstar\_sdss

The  $L/L^*$ ratio calculated using *Bmag\_sdss* and *bestDist* following Eq. 2.5.

### 2.3.70 e\_Lstar\_sdss

*Lstar\_sdss* error calculated with *e\_bestDist* and Jester et al. (2005) conversion errors (see §2.3.64).

### 2.3.71 altNames

The NED list of alternative object names for this galaxy with spaces removed. In the main catalogue we have included only NGC, IC, UGC, SDSS, and 2MASS names in this column. The associated alternative names catalogue contains the full list. Note that our preferred name, *Name*, and *NEDname* will only appear in the *altNames* list if they match these same criteria.

## 2.4 Limitations & Future

This catalogue is not meant to be entirely robust or comprehensive - rather it's purpose is to present a common batch of parameters for nearby galaxies in a easily retrievable and machine-readable manner. We have nonetheless endeavored to provide reasonable error estimates on all derivations and for as many observed quantities as possible.

Some caveats:

1. This is not the result of a targeted survey or observing program, so it's coverage and completeness is inherently non-uniform. We have endeavored to quantify this

non-uniformity in Section 3.1. A future version of this catalogue will include all-sky coverage maps for each relevant major input catalog (e.g., SDSS, 2MASS, etc.).

2. The quality of the data and observational errors are difficult to determine. We present this dataset as more of a convenient "quick-look" directory than a scientifically rigorous data product.
3. This catalogue will soon be made available online as a searchable SQL database, and downloadable in csv and ascii-fixed-width formats. Please contact the authors for details.

This research has made use of the NASA/IPAC Extragalactic Database (NED) which is operated by the Jet Propulsion Laboratory, California Institute of Technology, under contract with the National Aeronautics and Space Administration.

## References

- Corwin, Jr., H. G., Buta, R. J., & de Vaucouleurs, G. 1994, AJ, 108, 2128  
 Geller, M. J., & Huchra, J. P. 1983, ApJS, 52, 61  
 Heidmann, J., Heidmann, N., & de Vaucouleurs, G. 1972a, MmRAS, 75, 85  
 —. 1972b, MmRAS, 75, 121  
 Huchra, J. P., & Geller, M. J. 1982, ApJ, 257, 423  
 Iglewicz, B., & Hoaglin, D. 1993, How to Detect and Handle Outliers, ASQC basic references in quality control (ASQC Quality Press)  
 Jarrett, T. H., Chester, T., Cutri, R., Schneider, S. E., & Huchra, J. P. 2003, AJ, 125, 525  
 Jester, S., Schneider, D. P., Richards, G. T., et al. 2005, AJ, 130, 873  
 Marzke, R. O., Huchra, J. P., & Geller, M. J. 1994, ApJ, 428, 43  
 Schlafly, E. F., & Finkbeiner, D. P. 2011, ApJ, 737, 103  
 Stocke, J. T., Keeney, B. A., Danforth, C. W., et al. 2013, ApJ, 763, 148

Tully, R. B. 2015, AJ, 149, 171

Tully, R. B., Rizzi, L., Shaya, E. J., et al. 2009, AJ, 138, 323

Wakker, B. P., Hernandez, A. K., French, D. M., et al. 2015, ApJ, 814, 40

Wakker, B. P., & Savage, B. D. 2009, ApJS, 182, 378

## Chapter 3

# Probing Large Galaxy Halos at $z \sim 0$ with Automated Ly $\alpha$ -Absorption Matching

*A version of this chapter has previously appeared  
in the Astrophysical Journal*

D. M. French & B. P. Wakker, 2017, ApJ, 837, 2

## Abstract

We present initial results from an ongoing large-scale study of the circumgalactic medium in the nearby Universe ( $cz \leq 10,000 \text{ km s}^{-1}$ ), using archival Cosmic Origins Spectrograph spectra of background quasi-stellar objects. This initial sample contains 33 sightlines chosen for their proximity to large galaxies ( $D \geq 25 \text{ kpc}$ ) and high signal-to-noise ratios ( $\text{S/N} \geq 10$ ), yielding 48 Ly $\alpha$  absorption lines that we have paired with 33 unique galaxies, with 29 cases where multiple absorbers within a single sightline are paired with the same galaxy. We introduce a likelihood parameter to facilitate the matching of galaxies to absorption lines in a reproducible manner. We find the usual anti-correlation between Ly $\alpha$  equivalent width ( $EW$ ) and impact parameter ( $\rho$ ) when we normalize by galaxy virial radius ( $R_{\text{vir}}$ ). Galaxies associated with a Ly $\alpha$  absorber are found to be more highly-inclined than galaxies in the survey volume at a  $> 99\%$  confidence level (equivalent to  $\sim 3.6\sigma$  for a normal distribution). In contrast with suggestions in other recent papers of a correlation with azimuth angle for Mg II absorption, we find no such correlation for Ly $\alpha$ .

### 3.1 INTRODUCTION

It is well known that galaxies must continue to accrete gas throughout their lifetimes in order to sustain their observed levels of star formation (e.g., Erb 2008; Prochaska & Wolfe 2009; Putman et al. 2009a, 2009b; Bauermeister et al. 2010; Genzel et al. 2010). This additional gas must come from the diffuse intergalactic medium (IGM), where the majority of the baryons in the universe reside (Penton et al. 2002, 2004; Lehner et al. 2007; Danforth & Shull 2008; Shull et al. 2012). How exactly this IGM gas eventually falls into the halos and disks of galaxies is still highly uncertain, as observational constraints are hard to come by. Because of the diffuse nature of IGM gas, it is most readily and sensitively detected as absorption in the spectra of background quasi-stellar objects (QSOs). The advent of the sensitive ultraviolet (UV) Cosmic Origins Spectrograph (COS) on the *Hubble Space Telescope* (*HST*; Osterman et al. 2011; Green et al. 2012) has provided a wealth of information about the properties and distribution of both the ions of heavy elements as well as the Lyman series of neutral hydrogen (H I) gas around galaxies.

Individual concentrations of gas along a given sightline imprint absorption lines onto the spectrum in the direction of the QSO. The metal lines trace the star formation history within the intervening gas, and H I lines (e.g., Ly $\alpha$ ) indicate both the location and velocities of outflowing gas, as well as the presence of fuel for future star formation. Numerous studies using these observations have shown that many Ly $\alpha$  absorbers trace individual galaxy halos (e.g., Lanzetta et al 1995; Chen et al. 1998, 2001; Tripp et al. 1998; Wakker & Savage 2009; Steidel et al. 2010; Prochaska et al. 2011; Tumlinson et al. 2011, 2013; Thom et al. 2012; Stocke et al. 2013, 2014; Liang & Chen 2014; Tejos et al. 2014; Borthakur et al. 2015).

Some recent studies found that about half of Ly $\alpha$  absorbers lie within galaxy halos, at impact parameters  $\rho < 350$  kpc (Côté et al. 2005; Prochaska et al. 2006; Wakker & Savage 2009). In addition, Wakker & Savage (2009) found that an absorber lies within 400 kpc and  $400 \text{ km s}^{-1}$  for 90% of galaxies brighter than  $0.1L^*$ , and all galaxies have a Ly $\alpha$  absorber within 1.5 Mpc. Higher-redshift studies, such as Rudie et al. (2012a) at  $2 < z < 3$ , found evidence for an elevated density of absorbers up to 2 Mpc from galaxies. Wakker & Savage (2009) also discovered a correlation between Ly $\alpha$  absorption linewidth and impact parameter  $\rho$ , observing that the broadest lines ( $\text{FWHM} > 150 \text{ km s}^{-1}$ ) are only seen within 350 kpc of a galaxy, while at  $\rho > 1$  Mpc, only lines with  $\text{FWHM} < 75 \text{ km s}^{-1}$  occur. This suggests that the temperature and/or turbulence of gas increases in the presence of galaxies, a hypothesis that has been further supported by the results of Wakker et al. (2015).

Studying the enrichment of galaxy halos is necessary for constraining outflow models and informing stellar feedback prescriptions. Directly measuring the velocities and column densities of absorbers as a function of impact parameter and orientation around galaxies would provide the clearest evidence of inflow or outflow activity, but results are still uncertain. Kacprzak et al. (2011b) claimed to find that Mg II equivalent widths correlate with galaxy inclination, but Mathes et al. (2014) found no such correlation for Ly $\alpha$  and O VI absorbers. Furthermore, we should expect outflowing gas to be more highly enriched and trace the metallicity of the associated galaxy, with inflowing gas instead appearing only in H I. Both Stocke et al. (2013) and Liang & Chen (2014) found an “edge” to heavy ion absorption at  $\sim 0.5R_{\text{vir}}$ , but found Ly $\alpha$  covering fractions of  $\sim 0.75 - 1$  continuing out to  $R_{\text{vir}}$ . However, Mathes et al. (2014) measured O VI absorption out to  $\sim 3R_{\text{vir}}$ , and Savage et al. (2014) found that more than half of O VI absorption occurs beyond 1  $R_{\text{vir}}$  from the nearest galaxy. Additionally, Borthakur et al. (2015) found that Ly $\alpha$  absorption  $EW$  correlates with galaxy H I gas fraction, but only weakly with SFR, suggesting that

accretion flow from the CGM is slow and continuous.

Recent results from Kacprzak et al. (2011b, 2012a) suggest that absorbing systems have a preferred orientation with respect to the major and minor axes of the galaxies they are associated with. This could be evidence of inflows and outflows, or an effect of the global structure of galaxy halos, but the statistics are not yet good enough to provide consistent answers. A larger-scale study of inclination and azimuthal angles versus absorber properties is needed in order to elucidate the distribution of absorbing systems around galaxies. This is most easily done for the largest galaxies in the nearby universe, where it is possible to obtain inclinations and unambiguous absorber associations.

Previous studies have suffered from small sample sizes (e.g., Mathes et al. 2014 used 14 galaxies, Stocke et al. 2013 used 11, Werk et al. 2014 used 44), incompleteness due to their higher mean redshifts (e.g., the Mathes et al. 2014 sample is  $0.12 < z < 0.67$ ), and limited impact parameter reach (e.g., Werk et al. 2014 probed CGM gas only within  $\rho < 160$  kpc of galaxies). To address these shortcomings, we are conducting a large survey of the properties of intergalactic gas in the nearby universe, where we have good and relatively complete information on both faint and bright galaxies, in order to reveal how the IGM and galaxies affect each other.

We are taking advantage of the over 500 archived QSO and Seyfert spectra taken by the COS and Space Telescope Imaging Spectrograph (STIS) on *HST*, combined with the wealth of information available for the  $\sim 100,000$  galaxies with  $cz < 10,000 \text{ km s}^{-1}$  found in the NASA Extragalactic Database (NED) to probe the environment of absorbing gas systems in the nearby universe. In this paper we introduce a new, numerical method for associating absorption lines with nearby galaxies. This approach will allow for an objective understanding of the distribution of the gas around galaxies, which requires looking for both detections and non-detections of gas, both near and far from galaxies, with a robust

and reproducible metric for matching galaxies with absorption.

This paper presents our likelihood-matching method with initial results from a pilot study of 33 sight lines, chosen for their proximity to large galaxies and high signal-to-noise spectra. It is organized as follows. In Section 2 we present the data and analysis techniques, in Section 3 we present the results, in Section 4 we discuss possible interpretations of our results, and in Section 5 we present a summary.

## 3.2 DATA AND ANALYSIS

### 3.2.1 Galaxy Data

Achieving the goal of this study relies on knowing the locations and properties of all galaxies near detected Ly $\alpha$  absorption lines. To facilitate this, we have constructed a database of all  $z \leq 0.033$  ( $cz \leq 10,000 \text{ km s}^{-1}$ ) galaxies with published data available through the NASA Extragalactic Database (NED). A full description of this catalog will be presented in D. M. French & B. P. Wakker (2017, in preparation). Here we summarize its most important aspects.

The galaxy data set contains over 108,000 entries, and includes data from SDSS, 2MASS, 2dF, 6dF, RC3, and many other, smaller surveys. Our criterion for including a galaxy in this data set is only an accurate, spectroscopic redshift that places the galaxy in the  $cz \leq 10,000 \text{ km s}^{-1}$  velocity range. This restriction leads to a completeness limit of  $B \lesssim 18.7$  mag, or  $\sim 0.2L^*$ , at  $cz = 10,000 \text{ km s}^{-1}$ , and progressively better towards lower velocities (see Figure 3.1).

This limit will vary depending on which major surveys include a particular region of the sky. The major contributor is whether or not SDSS data are available, which begins around  $cz = 5000 \text{ km s}^{-1}$ . Figure 3.1 is split into four velocity bins to illustrate this. Our

data are complete down to  $\sim 0.1L^*$  in the first bin,  $0 \leq cz \leq 2500 \text{ km s}^{-1}$ . At slightly higher velocities,  $2500 \leq cz \leq 6000 \text{ km s}^{-1}$ , the completeness falls to barely better than  $\sim 1.0L^*$  as we move past the near and well studied galaxies, but have yet to reach the footprint of deep surveys. SDSS data become available in the last two bins, spanning  $6000 \leq cz \leq 10,000 \text{ km s}^{-1}$ . While the  $8000 \leq cz \leq 10,000 \text{ km s}^{-1}$  region appears to reach the expected SDSS limits of  $B \lesssim 18.7$  mag, or  $\sim 0.2L^*$ , the  $6000 \leq cz \leq 8000 \text{ km s}^{-1}$  region instead appears to flatten below  $\sim 1.0L^*$ . It is possible this is due to larger distance errors, since in this region redshift-independent distances are rare, and Hubble flow distances are

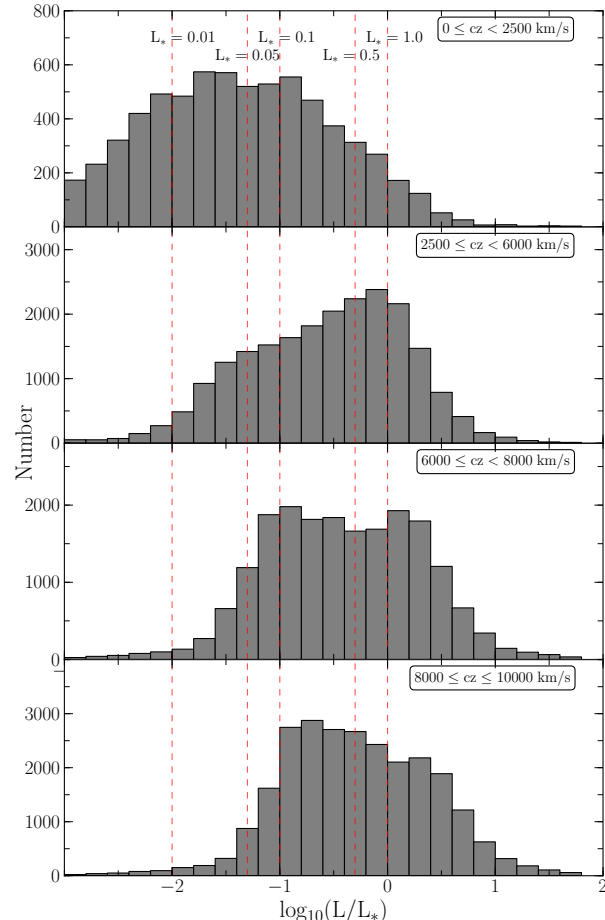


**Figure 3.1 :** Distribution of  $L/L^*$  values for all galaxies in the dataset. The red dashed vertical lines highlight  $1, 0.5, 0.1, 0.05$  and  $0.01 L^*$ .

still small enough to remain relatively uncertain.

Additionally, we have homogenized the galaxy data beyond the steps taken by NED by normalizing all measurements of galaxy inclination, position angle, and diameter to 2MASS  $K$ -band values. Most galaxies in NED have measures of inclination, position angle and diameter available in several different bands, so in order to make meaningful comparisons it is necessary to automatically choose one band for all measurements. We chose 2MASS values for this because it was an all-sky survey, and represents the largest fraction of available galaxy data. Physical galaxy diameters are derived from 2MASS  $K_s$  “total” angular diameter measurements and galaxy distances. 2MASS  $K_s$  “total” diameter estimates are surface brightness extrapolation measurements and are derived as

$$r_{\text{tot}} = r' + a(\ln(148))^b, \quad (3.1)$$

where  $r_{\text{tot}}$  is defined as the point where the surface brightness extends to 5 disk scale lengths,  $r'$  is the starting point radius ( $> 5'' - 10''$  beyond the nucleus, or core influence), and  $a$  and  $b$  are Sersic exponential function scale length parameters ( $f = f_0 \exp(-r/a)^{(1/b)}$ ; see Jarrett et al. 2003 for a full description). Approximately 50% of all the galaxies have this 2MASS  $K_s$  “total” diameter. Of the remainder, 20% have SDSS diameters, 27% have no published diameter, and 3% have diameters from other surveys. We convert values in these other bands to 2MASS  $K_s$  “total” diameters via a simple least squares linear fit when necessary.

We used  $B$ -band magnitudes to estimate each galaxy’s luminosity in units of  $L^*$  as follows:

$$\frac{L}{L^*} = 10^{-0.4(M_B - M_{B^*})}. \quad (3.2)$$

We adopt the CfA galaxy luminosity function by Marzke et al. (1994), which sets  $B^* = -19.57$ . Direct  $B$ -band measurements are available for  $\sim 30\%$  of galaxies, and most of the rest have SDSS  $g$  and  $r$  magnitudes, which can be converted to  $B$  via  $B = g + 0.39(g - r) + 0.21$  (Jester et al. 2005). Finally, we also compute an estimate of the virial radius of each galaxy as  $\log R_{\text{vir}} = 0.69 \log D + 1.24$ . This follows the parametrization of Stocke et al. (2013) relating a galaxy's luminosity to its virial radius, and the Wakker & Savage (2009) empirical relation between diameter and luminosity (see Wakker et al. 2015 and references therein for further details). Errors are propagated from the original published magnitude errors.

This homogeneous galaxy data table allows us to draw direct comparisons between the properties of the absorbers and the properties, separations, and environments of nearby galaxies with unprecedented completeness. The full dataset will be publicly released and discussed in further detail in a forthcoming paper (D. M. French & B. P. Wakker 2017, in preparation).

### 3.2.2 Spectra

This initial pilot study contains 33 sightlines to bright QSOs observed with COS. We chose sightlines by first sorting the galaxy data table described above by galaxy diameter. This sorted list is then correlated with the full list of publicly available sightlines, and only those systems with impact parameters less than 500 Mpc and galaxy diameters,  $D$ , greater than 25 kpc, are kept. Finally, we select 33 sightlines with  $S/N \geq 10$  from this list (see Table 3.1).

All COS spectra for the target sightlines were obtained through the Barbara A. Mikulski Archive for Space Telescopes (MAST), and processed with CALCOS v3.0 or later. We combined individual exposures by the method of Wakker et al. (2015), which

Table 3.1 : COS Targets in this Sample

Target	R.A.	Decl.	<i>z</i>	Program	Grating	Obs ID	Obs Date	T <sub>exp</sub> <sup>a</sup> (ks)	S/N <sup>a</sup> (1238)
(1)	(2)	(3)	(4)	(5)	(6)	(7)	(8)	(9)	(10)
1H0717+714	07 21 53.3	+71 20 36	0.5003	12025	G130M	LBG812	11-12-27	6.0	37
2dFGRS-S393Z082	02 45 00.8	-30 07 23	0.3392	12988	G130M	LC1040	13-05-27,28	17.7	10
FBQSJ1431+2442	14 31 25.8	+24 42 20	0.4069	13342	G130M	LC8903	15-03-29	16.5	17
H1101-232	11 03 37.7	-23 29 31	0.1860	12025	G130M	LBS314	13-03-08		
HE0241-3043	02 43 37.7	-30 30 48	0.6693	12988	G130M	LBG804	11-07-05	13.3	16
LBQS1230-0015	12 33 04.1	-00 31 34	0.4709	11598	G130M	LB5N15	13-06-21	7.0	14
MRC2251-178	22 54 05.9	-17 34 55	0.0661	12029	G130M	LBP250	12-04-26		
Mrk290	15 35 52.3	+57 54 09	0.0296	11524	G130M	LBGB03	11-09-29	5.5	42
Mrk876	16 13 57.2	+65 43 10	0.1290	11524	G130M	LB4Q02	09-10-28	3.9	38
Mrk1014	01 59 50.2	+00 23 41	0.1630	12569	G130M	LB4Q03	10-04-08,09	12.6	65
PG0832+251	08 35 35.9	+24 59 41	0.3310	12025	G130M	LB4F05	12-01-25	1.8	17
PG0003+158	00 05 59.3	+16 09 49	0.4509	12038	G130M	LBG808	12-04-19	6.1	14
PG1001+054	10 04 20.1	+05 13 01	0.1610	13347	G130M	LBGL17	11-10-22	10.4	25
PG1302-102	13 05 33.0	-10 33 20	0.2784	12038	G130M	LCCV02	14-06-19	5.2	14
RE81768	21 38 49.7	-38 28 40	0.1830	12936	G130M	LC9W02	14-04-04		
RX J0714.5+7408	07 14 36.2	+74 08 11	0.3710	12275	G130M	LB4P04	12-01-25	1.8	17
RX J1017.5+4702	10 17 30.9	+47 02 25	0.3354	13314	G130M	LBG808	12-04-19	6.1	14
RX J1117.6+5301	11 17 40.5	+53 01 50	0.1587	14240	G130M	LBGL17	11-10-22	10.4	25
RX J1236.0+2641	12 36 04.1	+26 41 36	0.2092	12248	G130M	LCW7M05	14-04-13	4.9	11
RX J1330.8+3119	13 30 53.2	+31 19 32	0.2423	12248	G130M	LC1201	13-06-25	7.0	24
RX J1356.4+2515	13 56 25.6	+25 15 23	0.1640	12248	G130M	LBH4O2	11-03-18	8.3	18
RX J1503.2+6810	15 03 16.5	+68 10 06	0.1140	12276	G130M	LC9M04	14-01-29	8.7	12
RX J1544.5+2827	15 44 30.5	+28 27 56	0.2314	13423	G130M	LBH087	12-01-29	4.2	11
RX J2043.1+0324	20 43 06.2	+03 24 50	0.2710	13840	G130M	LBHO85	11-07-11	4.3	11
RX J2139.7+0246	21 39 44.2	+02 46 05	0.2600	13840	G130M	LBH057	12-02-03	2.3	10
SB0957+599	10 01 02.6	+59 44 15	0.7475	12248	G130M	LBH1609	10-12-31	1.9	11
SDSSJ021218.32-073719.8	02 12 18.3	-07 37 20	0.1739	12248	G130M	LC9W08	14-02-25	2.1	10
SDSSJ080838.80+051440.0	08 08 38.8	+05 14 40	0.3606	12603	G130M	LBHO92	11-08-21		
SDSSJ091728.60+271951.0	09 17 28.6	+27 19 51	0.0756	14071	G130M	LBHO92	11-08-21		
						LBS330	12-03-17	4.7	10
						LCX202	15-11-30	15.5	11
						LCX2Z2	16-02-06		

Continued on Next Page...

Table 3.1 – Continued

Target (1)	R.A. (2)	Decl. (3)	$z$ (4)	Program (5)	Gating (6)	Obs ID (7)	Obs Date (8)	$T_{\text{exp}}^{\text{a}}$ (ks) (9)	S/N <sup>a</sup> (1238) (10)
SDSSJ112224.10+031802.0	11 22 24.1	+03 18 02	0.4753	12603	G130M	LBS318	13-03-29	7.6	13
SDSSJ130524.30+035731.0	13 05 24.3	+03 57 31	0.5457	12603	G130M	LBS321	12-06-25,26	7.6	13
SDSSJ135726.27+043541.4	13 57 26.2	+04 35 41	1.2345	12264	G130M	LBJ005	11-06-22	14.1	21
SDSSJ140428.30+335342.0	14 04 28.3	+33 53 42	0.5500	12603	G130M	LBJ007	11-06-26		
TON109	09 09 06.1	+32 36 31	0.8103	12603	G130M	LBS320	13-03-03	7.7	10
						LBS328	12-04-22	4.7	12

<sup>a</sup>Total exposure time and S/N ratio is given for multi-orbit exposures.

corrects the COS wavelength scale by cross-correlating all ISM and IGM lines in each exposure. This method addresses the up to  $\pm 40 \text{ km s}^{-1}$  misalignments produced by CALCOS, and produces a corrected error array based on Poisson noise, which better matches the measured errors than the errors delivered in the x1d files. We then combine multiple exposures by aligning Galactic absorption lines with 21 cm spectra, and adding up the total counts in each pixel before converting to flux using the original, average flux-count ratio at each wavelength.

Each absorption component is treated individually. Of our sample of 48, 13 are partially blended with another line (see Figure 3.2(a) as an example - 12 of these 13 are likewise blended with another Ly $\alpha$  line), and 35 are distinct, such that the flux returns to the continuum level between the lines. The result of this method is that 14 galaxies are associated with multiple Ly $\alpha$  systems. Equivalent widths are measured by first performing a low-order (3rd order or lower) polynomial continuum fit in the line region. Then we integrate over the absorption velocity range, and calculate errors by the method of Wakker et al. (2003), which combines the random noise errors, the uncertainty of the continuum location, fixed-pattern noise, and the uncertainty in choosing the absorption velocity edges. Finally, a Gaussian is fit to the absorption profile to determine the line centroid.

### 3.3 RESULTS

We have identified 48 Ly $\alpha$  absorption lines in the spectra of our initial 33 QSO sample, each of which has been associated with a single nearby galaxy of diameter  $D \geq 25 \text{ kpc}$ . Each absorption component is treated individually, resulting in several cases where multiple absorbers are associated with the same galaxy. In order to be considered for a pairing, a galaxy and absorption feature must appear within  $400 \text{ km s}^{-1}$  in velocity and  $500 \text{ kpc}$  in physical impact parameter from each other. When multiple galaxies pass these criteria for

a particular line, we are left with two options: (1) one galaxy is obviously far larger and closer in physical and velocity space to the sightline, and may have several satellite galaxies; or (2) there are multiple galaxies near the absorber, making any association ambiguous; we do not include these cases in the further analysis.

To facilitate this decision, we calculate the likelihood,  $\mathcal{L}$ , of every possible galaxy-absorber pairing as follows:

$$\mathcal{L} = A e^{-(\frac{\rho}{R_{\text{eff}}})^2} e^{-(\frac{\Delta v}{v_{\text{norm}}})^2}. \quad (3.3)$$

Here  $\rho$  is the physical impact parameter,  $\Delta v$  is the velocity difference between the absorber and the galaxy ( $\Delta v = v_{\text{galaxy}} - v_{\text{absorber}}$ ),  $v_{\text{norm}}$  is the velocity normalization constant, and  $A$  is a factor included to increase the likelihood in the case that  $\rho \leq R_{\text{eff}}$  (in which case  $A = 2$ , otherwise  $A = 1$ ). Many similar studies and simulations (e.g., Wakker & Savage 2009; Liang & Chen 2014; Mathes et al. 2014) suggest that Ly $\alpha$  absorbers lie within 400 km s $^{-1}$  of their associated galaxies, so throughout this paper we adopt a halfway point of  $v_{\text{norm}} = 200$  km s $^{-1}$ . Future work will explore the result of varying this normalization parameter and making refinements such as, e.g., relating  $v_{\text{norm}}$  to the galaxy's rotation velocity.

We compute  $\mathcal{L}$  for two different values of  $R_{\text{eff}}$ :  $R_{\text{vir}}$ , the virial radius of the galaxy, and  $D^{1.5}$ , the major diameter of the galaxy to the power of 1.5.  $\mathcal{L}$  computed with  $R_{\text{vir}}$  is liable to select satellite galaxies instead of the larger hosts, so including a version with  $D^{1.5}$  serves as a two-tiered selection system. An absorber separated by 200 km s $^{-1}$  in velocity and  $1R_{\text{vir}}$  in impact parameter from a  $D = 30$  kpc galaxy would have  $\mathcal{L}_{R_{\text{vir}}} = 0.27$  and  $\mathcal{L}_{D^{1.5}} = 0.11$ .

Table 3.2 : All Associated Systems Galaxy-absorber Systems

Target	Galaxy	$R_{\text{vir}}$ (kpc)	$L/L^*$ (km s $^{-1}$ )	$v_{\text{galaxy}}$ (km s $^{-1}$ )	Inc. (deg)	Az. (deg)	$\rho$ (kpc)	$v_{\text{Ly}\alpha}$ (km s $^{-1}$ )	$W_{\text{Ly}\alpha}$ (mÅ)	$\Delta v$ (km s $^{-1}$ )	$\mathcal{L}^{\text{a}}$
(1)	(2)	(3)	(4)	(5)	(6)	(7)	(8)	(9)	(10)	(11)	(12)
IH0717+714	UGC03804	173	1.9	2887	55	7	207	2870	343±6	17	0.24
IH0717+714	UGC03804	173	1.9	2887	55	7	207	2956	39±4	-69	0.21
2dFGRS S393Z082	NGC1097	304	6.1	1271	58	27	112	1239	570±21	32	1.9*
H1101-232	MCG-04-26-019	173	1.1	3623	68	26	179	3580	573±12	43	0.33
HE0241-3043	NGC1097	304	6.1	1271	58	77	219	1221	83±12	50	1.6*
HE0241-3043	NGC1097	304	6.1	1271	58	77	219	1310	184±15	-39	1.6*
LBQS1230-0015	NGC4517	208	0.5	1128	90	90	110	1127	473±16	1	1.6*
MRC2251-178	MCG-03-58-009	319	2.3	9030	61	39	320	9051	60±4	-21	1.4*
Mrk1014	NGC0768	231	3.0	7021	64	85	486	7080	117±11	-59	0.042*
Mrk290	NGC5987	322	3.0	3010	67	12	486	3105	511±5	-95	0.77**
Mrk290	NGC5987	322	3.0	3010	67	12	486	3207	319±4	-197	0.37*
Mrk876	UGC10294	165	0.1	3504	51	7	274	3478	280±3	26	0.063
PG0003+158	NGC7814	171	1.2	1050	68	47	197	833	131±15	217	0.081
PG0832+251	KUG0833+252	165	0.7	6964	62	55	294	6980	133±14	-16	0.041
PG0832+251	KUG0833+252	165	0.7	6964	62	55	294	7201	48±10	-237	0.01
PG1001+054	UGC05432	164	1.3	3995	36	78	217	4092	222±10	-97	0.14
PG1302-102	NGC4939	235	4.4	3110	48	61	265	3448	71±5	-338	0.05*
RBS1768	RFGC3781	253	1.0	9162	90	74	464	9360	364±4	-198	0.056*
RBS1768	RFGC3781	253	1.0	9162	90	74	464	9434	160±5	-272	0.024*
RX J0714.5+7408	UGC03717	202	1.2	4188	63	83	271	4074	58±7	114	0.13*
RX J0714.5+7408	UGC03717	202	1.2	4188	63	83	271	4264	410±9	-76	0.15*
RX J1017.5+4702	NGC3198	191	1.3	663	73	55	378	629	60±17	34	0.02
RX J1117.6+5301	NGC3631	187	1.9	1156	16	47	198	1131	356±20	25	0.32
RX J1117.6+5301	NGC3631	187	1.9	1156	16	47	198	1259	57±17	-103	0.25
RX J1236.0+2641	NGC4559	165	0.7	807	64	31	188	795	295±37	12	0.27
RX J1236.0+2641	NGC4565	292	1.7	1230	90	39	159	1012	337±32	218	0.54*
RX J1236.0+2641	NGC4565	292	1.7	1230	90	39	159	1188	288±24	42	1.7*
RX J1330.8+3119	UGC08492	204	2.0	7414	16	41	335	7401	330±15	13	0.081*
RX J1356.4+2515	CGCG132-055	206	1.3	8671	36	25	190	8475	126±18	196	0.35*
RX J1503.2+6810	CGCG318-012	250	2.1	9765	52	1	325	10122	44±14	-357	0.031*
RX J1544.5+2827	CGCG166-047	175	1.8	9646	43	61	326	9642	183±14	4	0.031
RX J1544.5+2827	CGCG166-047	175	1.8	9646	43	61	326	9759	169±12	-113	0.023
RX J2043.1+0324	NGC6954	166	1.4	4067	56	66	301	4080	82±10	-13	0.037
RX J2139.7+0246	UGC11785	203	0.7	4074	90	69	108	4083	490±7	-9	1.5
RX J2139.7+0246	UGC11785	203	0.7	4074	90	69	108	4181	529±7	-107	1.2*
SBS0957+599	MCG+10-14-058	261	1.1	9501	75	19	206	9469	78±12	32	1.4*
SDSSJ021218.32-073719.8	SDSSJ021315.79-	174	1.8	4800	52	10	268	4756	528±15	44	0.09

Continued on Next Page...

Table 3.2 – Continued

Target (1)	Galaxy (2)	$R_{\text{vir}}$ (kpc) (3)	$L/L^*$ (km s $^{-1}$ ) (4)	$v_{\text{galaxy}}$ (km s $^{-1}$ ) (5)	Inc. (deg) (6)	Az. (deg) (7)	$\rho$ (kpc) (8)	$v_{\text{Ly}\alpha}$ (km s $^{-1}$ ) (9)	$W_{\text{Ly}\alpha}$ (mÅ) (10)	$\Delta v$ (km s $^{-1}$ ) (11)	$\mathcal{L}^{\text{a}}$ (12)	
SDSSJ021218.32-073719.8	SDSSJ021315.79-073942.7	174	1.8	4800	52	10	268	4833	500±17	-33	0.092	
SDSSJ080838.80+051440.0	UGC04239	279	2.1	8763	45	38	378	8740	883±24	23	0.87*	
+051440.0	SDSSJ080838.80+051440.0	UGC04239	279	2.1	8763	45	38	378	8927	130±19	-164	0.45*
+051440.0	SDSSJ091728.60	UGC04895	204	2.1	7073	61	32	408	7141	374±23	-68	0.022*
+271951.0	SDSSJ112224.10	NGC3640	180	2.8	1251	38	22	139	1049	288±30	202	0.4
+031802.0	SDSSJ112224.10+031802.0	NGC3640	180	2.8	1251	38	22	139	1264	424±27	-13	1.1
+031802.0	SDSSJ130524.30	UGC08186	268	1.1	7006	82	14	249	7039	480±14	-33	1.3*
+035731.0	SDSSJ135726.27	NGC5364	211	2.4	1241	57	84	183	1124	85±11	117	0.74*
+043541.4	SDSSJ135726.27+043541.4	NGC5364	211	2.4	1241	57	84	183	1296	98±9	-55	0.97*
+043541.4	SDSSJ140428.30	KUG1402+341	204	1.1	7919	72	63	118	7884	889±28	35	1.4
+355342.0	TON1009	NGC2770	204	1.9	1947	87	41	274	1961	350±21	-14	0.19*

<sup>a</sup>The largest  $\mathcal{L}$  value is given, with a (\*) indicating that this corresponds to  $\mathcal{L}_{\text{D}^{1.5}}$ , otherwise the quoted  $\mathcal{L}$  was computed with  $R_{\text{vir}}$ .

In order for an absorber to be marked as “associated” with a particular galaxy, we require that its  $\mathcal{L}$  must be a factor of 5 larger than the next best possible association, and  $\mathcal{L} \geq 0.01$  for at least one of  $\mathcal{L}_{R_{\text{vir}}}$  or  $\mathcal{L}_{D^{1.5}}$ . We visually inspect systems with only one  $\mathcal{L}$  meeting these criteria, and decide to reject or include it based on the complexity of the nearby galaxy environment. In Table 3.2 we quote only the largest value of  $\mathcal{L}$ , and use an asterisk to denote when this corresponds to  $\mathcal{L}_{D^{1.5}}$ .

Figures 3.2(a) and 3.2(b) show an example of a Ly $\alpha$  absorption line with a map of its galaxy environment, showing an unambiguous pairing between the absorption features at  $3105, 3207 \text{ km s}^{-1}$  toward Mrk290 and galaxy NGC5987 ( $L^* = 0.37$ ). All analysis that follows concerns similarly “associated” systems.

Additionally, we split the absorber-galaxy catalog based on the velocity difference of the two,  $\Delta v$ . With this scheme, we refer to an absorber with a lower velocity than the associated galaxy as blueshifted, while an absorber with a higher velocity is referred to as redshifted. The rest of the results will be analyzed based upon this splitting. In all figures blue and redshifted absorbers are represented as blue diamonds and red circles, respectively, and red diamonds correspond to systems where both redshifted and blueshifted absorbers are detected. We use open symbols for systems with  $\rho \leq R_{\text{vir}}$ .

### 3.3.1 EW- $\rho$ Anti-correlation

Numerous previous studies have suggested that Ly $\alpha$  equivalent width ( $EW$ ) is anti-correlated with impact parameter ( $\rho$ ) to the nearest galaxy. We find a weak anti-correlation, as shown in Figure 3.3(a). However, as Churchill et al. (2013a) also found with Mg II absorption, we find a stronger anti-correlation when we normalize  $\rho$  by  $R_{\text{vir}}$ . Figure 3.3(b) shows this expected anti-correlation when plotting  $EW$  versus  $\rho/R_{\text{vir}}$ . A possible explanation for this trend is that larger galaxies host larger, more physically extended CGM

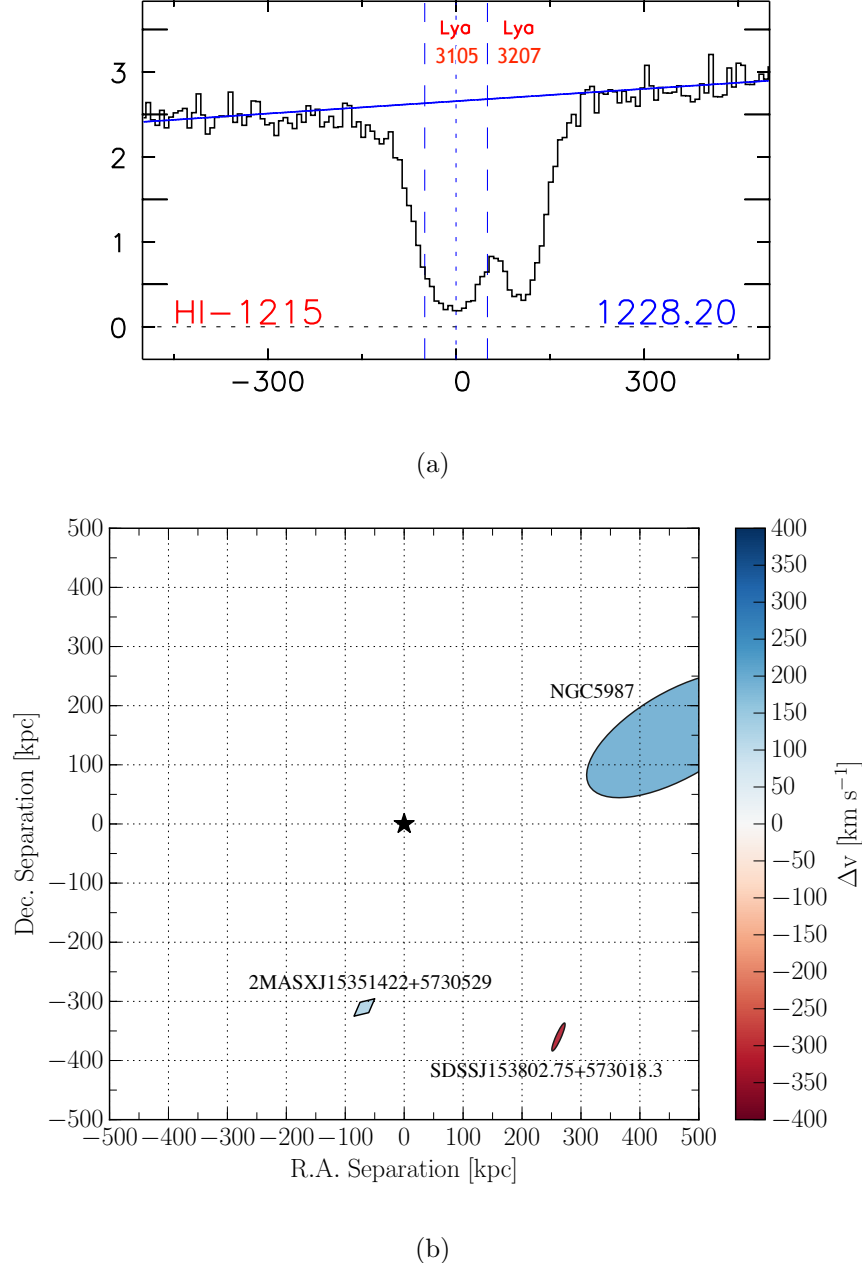


**Figure 3.2 :** (a) An example of 2 Ly $\alpha$  lines found in the Mrk290 sightline at 3105 and 3207 . (b) A map of *all* galaxies within a 500 kpc impact parameter of target Mrk290 sightline and with velocity ( $cz$ ) within  $400 \text{ km s}^{-1}$  of absorption detected at  $3207 \text{ km s}^{-1}$  (central black star). The galaxy NGC5987 ( $v = 3010 \text{ km s}^{-1}$ , inclination =  $65^\circ$ ) has been paired with the Ly $\alpha$  absorption features at  $v = 3105, 3207 \text{ km s}^{-1}$  because it is the largest and closest galaxy in both physical and velocity space to the absorption feature.

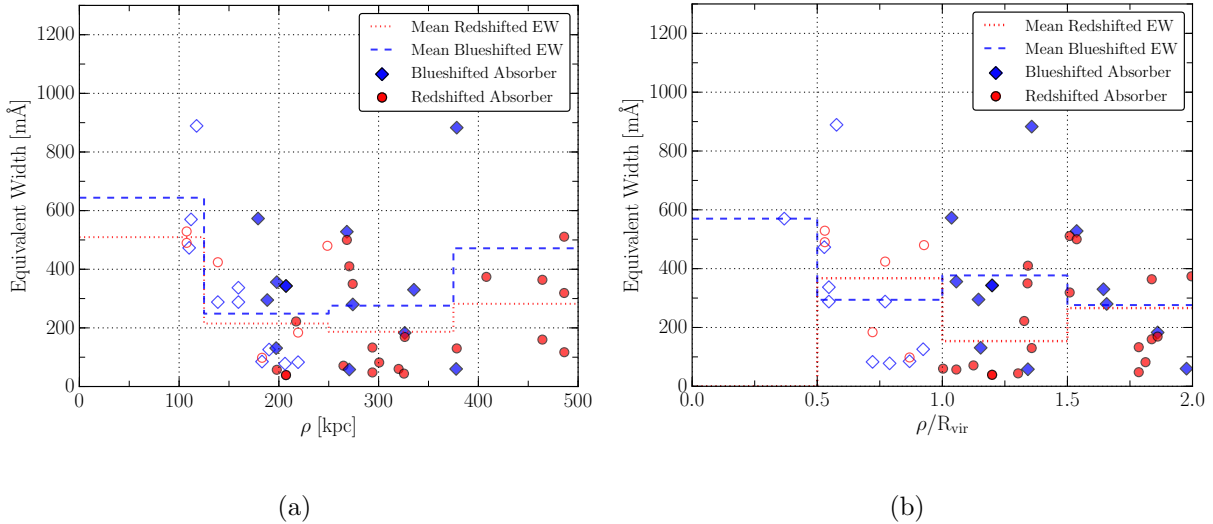


**Figure 3.3 :** (a) Equivalent width of each absorber as a function of impact parameter  $\rho$ . (b) Equivalent width as a function of  $\rho/R_{\text{vir}}$ . The anti-correlation is strongest when scaling  $\rho$  by the galaxy virial radius. Absorbers are separated into redshifted and blueshifted samples based on  $\Delta v$ . Bins of mean  $EW$  are overplotted in red dotted, and blue dashed lines for their respective samples. Open symbols correspond to systems with  $\rho \leq R_{\text{vir}}$ .

halos. We would thus expect the absorber  $EW$  to also correlate positively with  $R_{\text{vir}}$ . Figure 3.4(a) shows  $EW$  as a function of  $R_{\text{vir}}$ , with the blue-dashed and red-dotted lines showing the average  $EW$  in bins of 50 kpc of  $R_{\text{vir}}$ , showing little evidence of a correlation. However, by similarly plotting  $\rho$  as a function of  $R_{\text{vir}}$ , we instead find some evidence that absorbers around larger galaxies tend to be found at higher impact parameters. While we expect the upper-left quadrant of this figure to be sparsely populated (our likelihood-based method would tend not to choose small galaxies at large impact parameters), it is unclear to us why the lower right quadrant (large galaxies with absorbers at low impact parameter) is also sparsely populated. The full-sized sample at the completion of our study should provide a clearer picture.

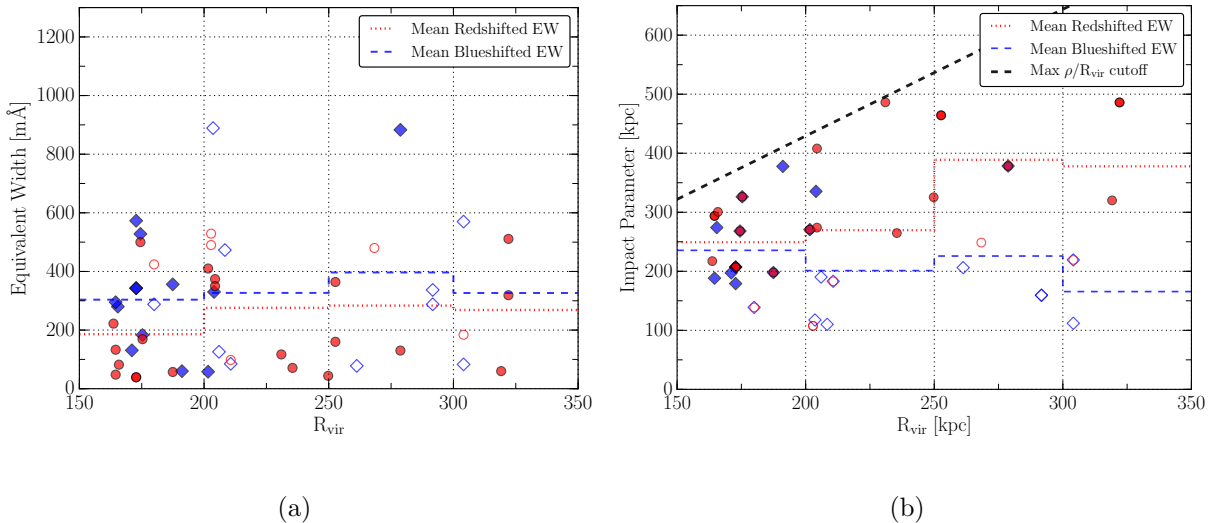


**Figure 3.4** : (a) Equivalent width of each absorber as a function of the virial radius of the associated galaxy. (b) Impact parameter to each absorber as a function of the virial radius of the associated galaxy. The black dashed line indicates the cutoff at  $\rho/R_{\text{vir}} = 2.14$  imposed by our  $\mathcal{L}$  limit. In each, the blue dashed and red dotted lines show the average  $EW$  in 50 kpc bins of impact parameter for the blueshifted and redshifted absorbers, respectively. Open symbols correspond to systems with  $\rho \leq R_{\text{vir}}$ .

### 3.3.2 Inclination

In this section we examine the inclinations of the associated galaxies compared to the distributions of absorbers. We correct for the finite thickness of galaxies, which causes  $b/a$  to deviate from  $\cos(i)$  at high inclinations, by computing galaxy inclinations with the following formula from Heidmann et al. (1972a):

$$\cos(i) = \sqrt{\frac{q^2 - q_0^2}{1 - q_0^2}}, \quad (3.4)$$

where  $q = b/a$ , the ratio of the minor to major axis, and  $q_0$  is the intrinsic axis ratio, set to  $q_0 = 0.2$  for all galaxies (e.g., Jones, Davies, and Trehewella 1996). Of the 48 total

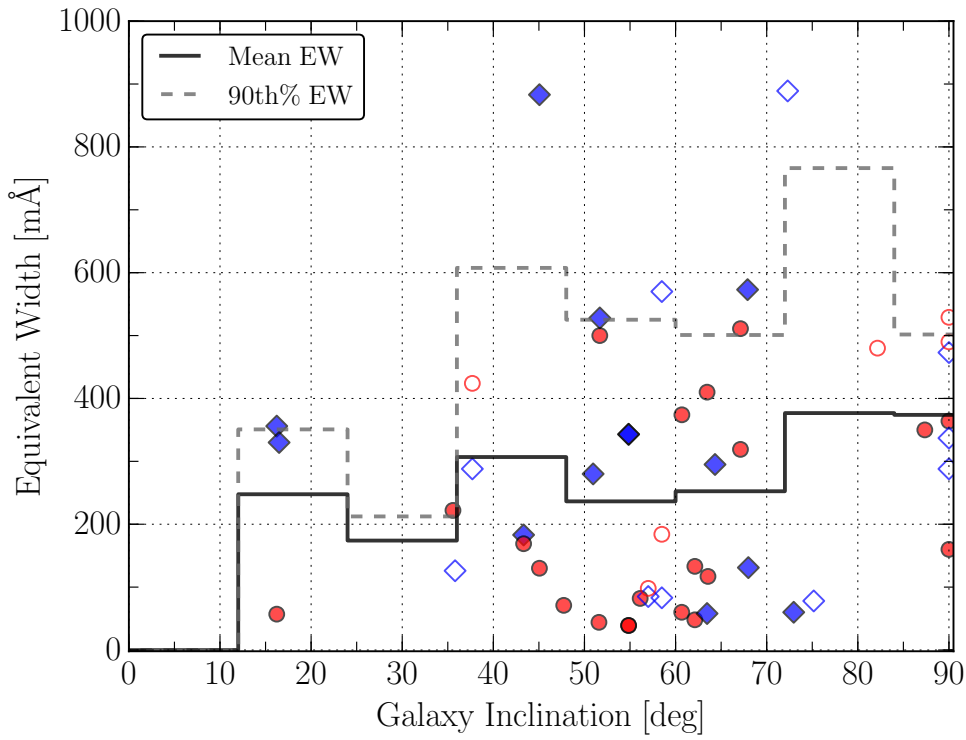


**Figure 3.5 :** Equivalent width of each absorber as a function of the inclination angle of the associated galaxy. The black and dashed gray lines show the mean and 90th percentile  $EW$  of all absorbers in bins of  $15^\circ$ . Open symbols correspond to systems with  $\rho \leq R_{\text{vir}}$ .

absorbers, 6 are associated with E or S0 type galaxies, but we have chosen to keep the value of  $q_0 = 0.2$  uniform throughout. The calculated values of  $\cos(i)$  that we use for these galaxies are thus conservative underestimates of their true inclinations.

Figure 3.5 shows red and blueshifted absorbers'  $EW$  plotted against the inclinations of their associated galaxies. We note that there is a clear excess of absorbers near galaxies of high inclination, with 77% of redshifted and 73% of blueshifted absorbers being associated with galaxies of  $i \geq 50$  deg, and only 3 absorbers being associated with a galaxy of  $i < 35$ . The black and grey-dashed lines show mean and 90th percentile histograms, respectively, in bins of 12 deg. There does not appear to be much evolution of  $EW$  across galaxy inclination, although a slight increase of mean  $EW$  is possibly present toward higher inclinations.

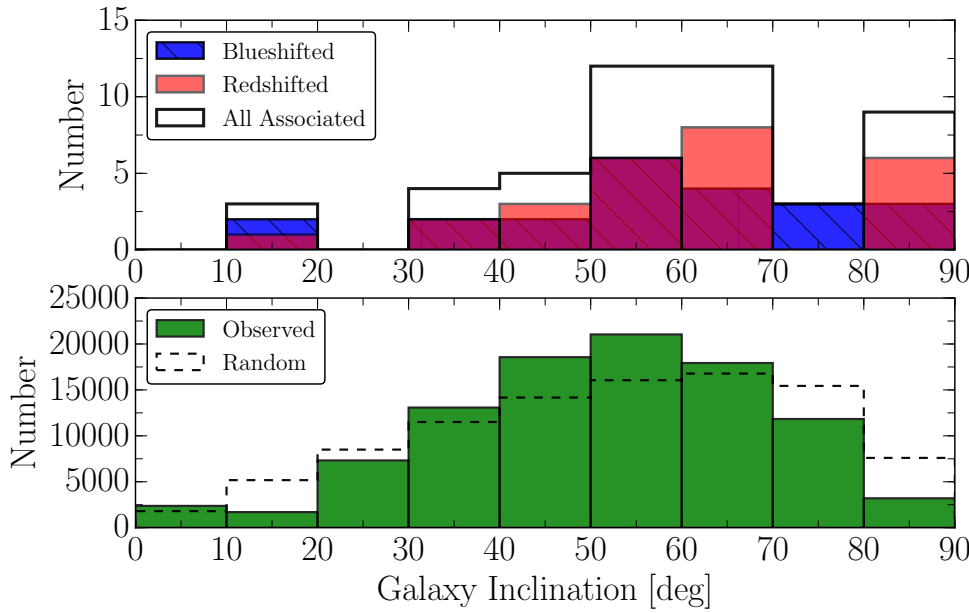


**Figure 3.6** : Top: distribution of inclinations for all associated galaxies, split into redshifted and blueshifted sets. Bottom: distribution of inclinations of all observed galaxies in the  $cz \leq 10,000$   $\text{km s}^{-1}$  redshift range. The dashed line shows the inclination distribution for a truly random sample (i.e., no observational biases).

In total, 75% of absorbers are associated with highly inclined galaxies ( $i \geq 50$  deg). Only 56% of all galaxies in the survey volume are highly inclined, indicating a preference for detecting absorption around inclined galaxies. Figure 3.6 shows the distribution of galaxy inclinations for both the red and blue-shifted associated galaxies and all galaxies within the survey volume. We tested the difference between the full distribution of inclination angles for all galaxies in our survey volume and the distribution for all associated galaxies (red + blue-shifted absorbers) using the Anderson-Darling (AD) statistical distribution test, yielding a  $p$ -value of  $AD_p = 0.00037$ . Thus at a 99.96% confidence level ( $\sim 3.6\sigma$  for a normal distribution) the inclinations of our associated galaxies are not sampled from the average distribution of observed inclinations. Hence, we take this to mean that the shape of the CGM of these galaxies is not perfectly spheroidal.

It is worth noting here that the observed distribution of galaxy inclinations is *not* flat, as one might naively expect. The dashed line in Figure 3.6 shows the distribution of observable inclinations for a random, uniform sample (i.e., a uniform distribution of  $q = b/a$  values between 0.2 and 1.0). There could be a number of effects contributing to the difference between this expected distribution and the observed (shown in green). If our sample is magnitude-limited and we assume galaxies are mostly optically thin but with a very-thin optically thick component (e.g., a dust lane), then mostly face-on and mostly edge-on galaxies would be underrepresented due to surface brightness and dust obscuration effects (e.g., see Jones, Davies and Trewhella 1996). It is possible that a similar effect is also responsible for the overabundance of Ly $\alpha$  detections around highly inclined galaxies. If we assume a disk or oblate spheroid halo shape and a covering fraction below unity for the CGM, the probability of encountering a cloud near an inclined galaxy would increase due to the increased path-length through the halo. We will produce a model to test this and other possible explanations in Paper II, when we have the much larger dataset available.

### 3.3.3 Velocity Difference ( $\Delta v$ )

We find evidence for an anti-correlation between absorber  $EW$  and the velocity difference between the galaxy and the associated absorption,  $\Delta v$ . The mean and maximal  $EW$  of absorption increases with decreasing  $\Delta v$  (see Figure 3.7). In total, 32/48 (67%) of absorbers are found within  $\pm 100 \text{ km s}^{-1}$ . This  $\pm 100 \text{ km s}^{-1}$  threshold also applies to absorber  $EW$ , with only 1 absorber of  $EW \geq 400$  found with  $\Delta v > 100 \text{ km s}^{-1}$ .

Blueshifted absorbers are on average closer both in velocity and impact parameter to their associated galaxy, with  $\overline{\Delta v}_{blue} = 68 \pm 16 \text{ km s}^{-1}$  and  $\overline{\rho_{blue}} = 218 \pm 17 \text{ kpc}$ , compared to  $\overline{\Delta v}_{red} = -108 \pm 20 \text{ km s}^{-1}$  and  $\overline{\rho_{red}} = 298 \pm 23 \text{ kpc}$  for the redshifted sample. Correspondingly, blueshifted absorbers have a slightly higher average equivalent width,

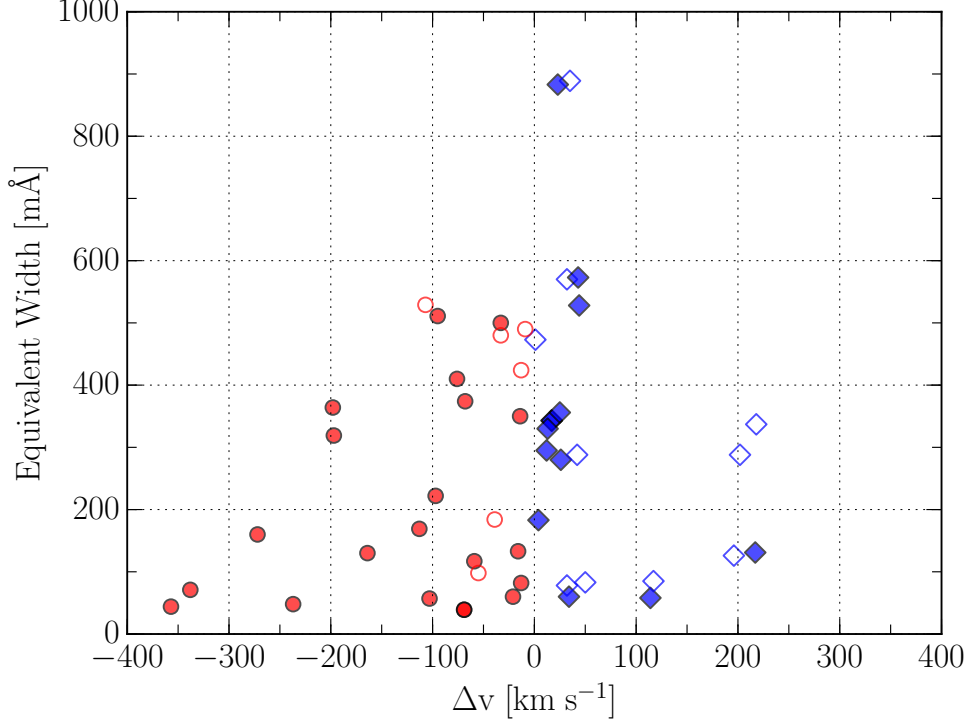


**Figure 3.7 :** Equivalent width as a function of the velocity separation between the galaxy and absorption line. Open symbols correspond to systems with  $\rho \leq R_{\text{vir}}$ .

$$\overline{EW}_{blue} = 329 \pm 52 \text{ m}\AA \text{ compared to } \overline{EW}_{red} = 245 \pm 34 \text{ m}\AA.$$

Additionally, of the 48 associated absorbers, 29 are matched with the same galaxy as another absorber (for a total of 14 unique galaxies in this subset). All but one of these cases involve two absorbers in the same sightline yet separated in velocity around a galaxy. Of these, 23 out of 29 are oriented such that the higher  $EW$  absorber has the smaller  $\Delta v$ , and the 6 others are close in either velocity or  $EW$ . The one galaxy with three associated absorbers, NGC1097, shows this trend across two sightlines as well, with absorbers at  $\Delta v = 32 \text{ km s}^{-1}$  and  $EW = 570 \text{ m}\AA$  toward 2dFGRS\_S393Z082, and  $\Delta v = -39 \text{ km s}^{-1}$  and  $EW = 184 \text{ m}\AA$  and  $\Delta v = 50 \text{ km s}^{-1}$  and  $EW = 83 \text{ m}\AA$  toward HE0241-3043.

This result is the opposite of what we might expect selection effects associated with our likelihood method to produce. Because  $\mathcal{L}$  is small for both high  $\Delta v$  and high  $\rho/R_{\text{vir}}$ ,

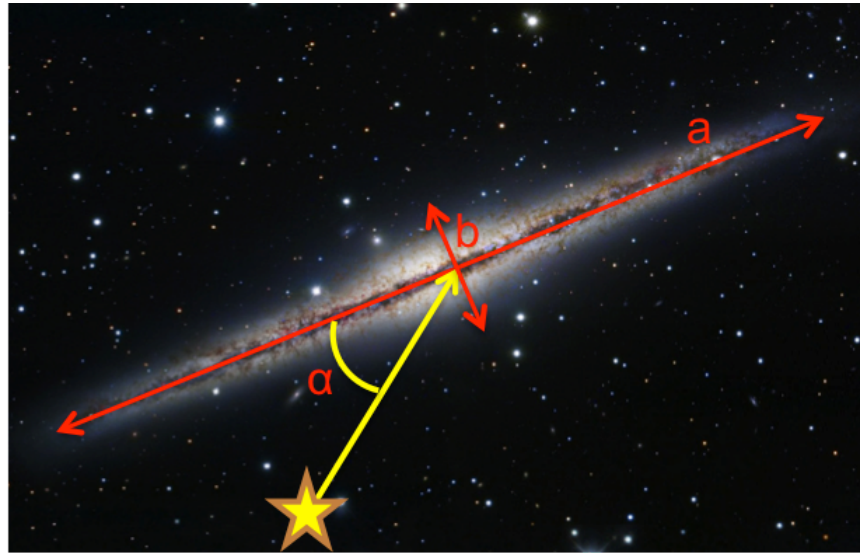


**Figure 3.8 :** Azimuth is the angle,  $\alpha$ , between the major axis of the galaxy,  $a$ , and a vector extending from the QSO target to the galaxy center. Image of NGC891 credit: composite Image Data - Subaru Telescope (NAOJ), Hubble Legacy Archive, Michael Joner, David Laney (West Mountain Observatory, BYU); Processing - Robert Gendler.

there should be mostly low  $\rho/R_{\text{vir}}$  systems at high  $\Delta v$ . Low  $\rho/R_{\text{vir}}$  systems should also have higher  $EW$  on average, as evidenced in the  $EW - \rho$  anti-correlation discussed above. Figure 3.7 shows the opposite, however, with only low- $EW$  systems at high  $\Delta v$ . It must therefore be the case that  $EW$  tends to anti-correlate with both  $\Delta v$  and  $\rho/R_{\text{vir}}$ . Disentangling the relative strengths of the correlations between  $EW$  and  $\rho$ ,  $R_{\text{vir}}$ , and  $\Delta v$  will require a larger data set, and thus we defer this discussion to our forthcoming Paper II of this series.

### 3.3.4 Azimuth

In this section we examine properties of absorbers as a function of their azimuthal angle with respect to their associated galaxy. Azimuth is defined as the angle between the major axis of a galaxy and the vector connecting the absorption feature and the midpoint of the galaxy plane. Figure 3.8 illustrates this.

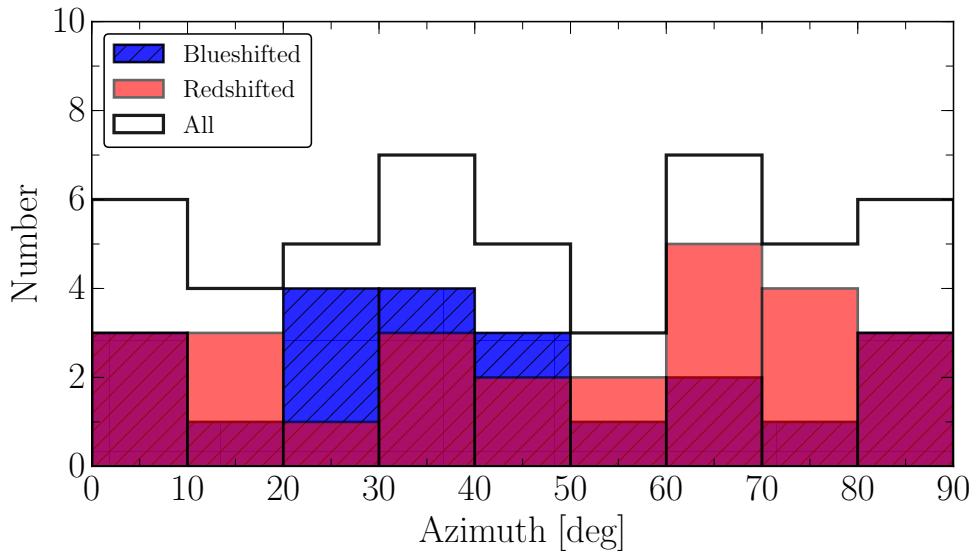


**Figure 3.9 :** The distributions of azimuth angles for red and blue-shifted samples, with the combined sample plotted in black. Azimuth = 0 corresponds to absorption detected along the projected major axis of the galaxy, and Azimuth = 90 is along the minor axis.

The mean azimuth angle for blueshifted absorbers is  $43 \pm 5^\circ$ , and  $49 \pm 5^\circ$  for redshifted absorbers. Figure 3.9 shows the distribution of azimuth angles for both red and blueshifted absorbers. Unlike the findings of Kacprzak et al. (2011b, 2012a), who find a bimodal distribution of Mg II absorbers around galaxies, our distributions of Ly $\alpha$  absorbers are generally consistent with a flat, or random distribution. There is possibly a slight overabundance of redshifted absorbers around  $0^\circ$  (minor axis) and blueshifted absorbers between  $20$  and  $50^\circ$  (just off major axis), but we cannot assign this observation much significance yet, given the small sample size. We additionally find no significant correlation between azimuth angle and  $EW$  or  $\Delta v$ . See Figure 3.10 for a map of the locations of absorbers relative to their associated galaxies, split between redshifted and blueshifted absorbers and into three bins of inclination.

These contrasting results may indicate a genuine difference between the properties of

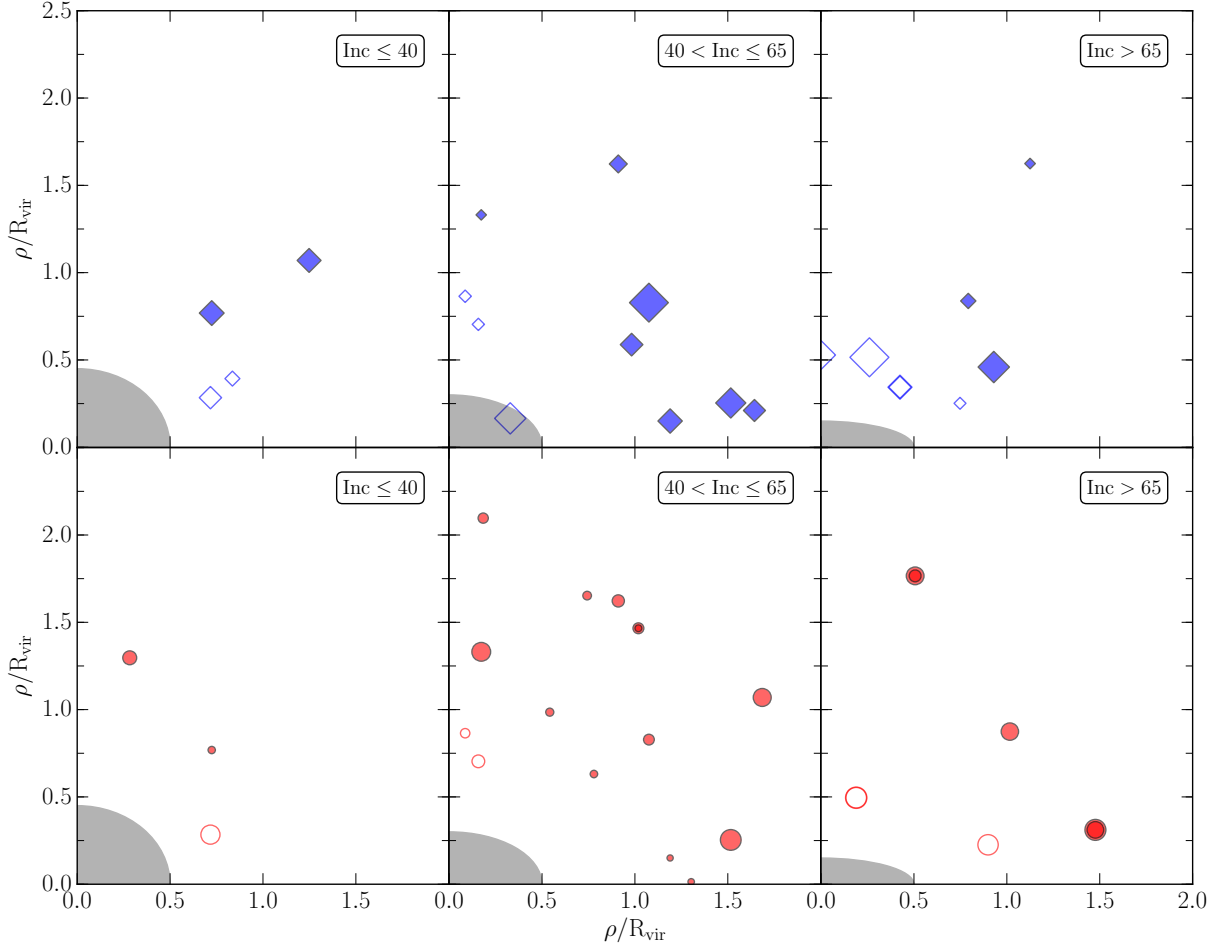


**Figure 3.10 :** A map of where each absorber was detected with respect to the associated galaxies, separated into three bins of inclination (illustrated by the gray ellipse in the bottom left corner of each plot). Left: absorbers associated with galaxies of inclination  $0 \leq \text{Inc} \leq 40$ ; center:  $40 \leq \text{Inc} \leq 65$ ; and right:  $65 \leq \text{Inc}$ . Blueshifted and redshifted absorbers are separated into the top (diamonds) and bottom (circles) panels, and the marker size is scaled with  $EW$ . The sightlines containing multiple absorbers associated with the same galaxy can be identified by their darker colors. Open symbols correspond to systems with  $\rho \leq R_{\text{vir}}$ .

Ly $\alpha$  and metal lines, since the distributions of the latter are thought to be influenced by outflows, which may be focused along the minor axis.

### 3.4 DISCUSSION

In this paper we have chosen to separate absorption systems into their individual components, whereas many comparable CGM studies have instead chosen to group together absorption components within some velocity window. While making the assumption that absorbers within some velocity interval are physically linked certainly has merit, it is also possible that absorption components close in velocity may in fact be physically distinct (see, e.g., Churchill et al. 2015). Indeed, in Section 3.3.3 we identified several systems where the  $EW$  of components of a possible Ly $\alpha$  system individually anti-correlated with  $\Delta v$ . We will thus explore both methods in Paper II, where the much larger sample size will allow for a meaningful comparison.

Restricting ourselves to low-redshift systems has several benefits and consequences. We are able to extend our search for associated galaxies to larger impact parameters than many related, higher-redshift CGM studies, because of the availability of galaxy data. However, due to the observed anti-correlation between  $EW$  and impact parameter, this results in a larger fraction of low- $EW$  and low-column density absorbers in our sample. Hence, we are likely tracing a region of the CGM not entirely analogous to that traced by, e.g., Kacprzak et al. (2011b), Mathes et al. (2014), and Borthakur et al. (2015).

Studies focusing on metal lines (e.g., Mg II and O VI) are generally associated with high column density Lyman Limit Systems (LLS), which, again, tend to originate closer to their host galaxies. Most of the Ly $\alpha$  absorbers in this work are low column density (generally  $\log N(\text{H I}) \leq 14$ ), and originate near or beyond  $1 R_{\text{vir}}$ . At these distances we may actually be probing the interface between CGM associated with individual galaxies and the larger-scale network of intergalactic gas filaments, thus the lack of any correlation

with azimuth angle is not wholly unexpected.

We do, however, detect an inclination effect on the density, and possibly  $EW$ , of Ly $\alpha$  absorbers. The combination of no azimuthal dependence and increased absorber density with inclination leads us to conclude that these galaxies have disk-like, oblate-spheroidal halos. A perfectly spheroidal halo would show no correlation for either, and an extremely flattened halo would show up as enhanced number density along the major axis. These results are consistent with a picture where the H I covering fraction steadily decreases from  $\sim$ unity very near to galaxy disks out to at least 1 Mpc, where gas associated with galaxies merges with the general IGM. Our larger upcoming dataset will provide the statistics necessary to probe this in finer detail, as well as give clues regarding the exact shape of this fall-off and the level of clumpiness or filamentary structure in galaxies' H I halos.

Table 3.3. Average properties of the associated galaxy sample split into red and blue-shifted bins based on  $\Delta v$

Statistic	Blueshifted Absorbers	Redshifted Absorbers
Number	22	26
Mean $EW$ [mÅ]	$329 \pm 52$	$245 \pm 34$
Median $EW$ [mÅ]	$292 \pm 16$	$177 \pm 10$
Mean $R_{vir}$ [kpc]	$215 \pm 10$	$224 \pm 10$
Mean $\rho$ [kpc]	$218 \pm 17$	$298 \pm 23$
Mean $\Delta v$ [ $\text{km s}^{-1}$ ]	$68 \pm 16$	$-108 \pm 20$
Mean Inc. [deg]	$58 \pm 4$	$61 \pm 4$
Mean Az. [deg]	$43 \pm 5$	$49 \pm 5$

Note. — All reported errors are standard errors in the mean.

### 3.5 SUMMARY

We have introduced a novel likelihood method for associating absorption systems with nearby galaxies, and explored its implementation with a small subsample of 33 COS sightlines. Associating CGM absorbers with individual galaxies remains a difficult and ambiguous affair, but with this new metric we can at least do so in a reproducible and numerical manner.

In this pilot sample we have measured 48 Ly $\alpha$  absorption lines in the spectra of 33 COS targets and matched each to a single, large ( $D \geq 25$  kpc) galaxy. Table 3.3 presents a breakdown of our results when separating absorber-galaxy pairs into red and blue-shifted samples. The following summarizes our findings:

1. We introduce a likelihood parameter,  $\mathcal{L}$ , based on Gaussian profiles centered around  $\rho/R_{\text{eff}}$  and  $\Delta v/v_{\text{norm}}$  to automate the matching of absorbers with associated galaxies. The response of  $\mathcal{L}$  can be tailored by choosing different values for  $R_{\text{eff}}$  and  $v_{\text{norm}}$  (we used  $R_{\text{eff}} = [R_{\text{vir}}, D^{1.5}]$  and  $v_{\text{norm}} = 200$  km s $^{-1}$  in this work, and will explore other parameterizations in a future paper).
2. Equivalent width ( $EW$ ) anti-correlates most strongly with  $\rho$  when normalized by  $R_{\text{vir}}$ . It follows that  $EW$  weakly correlates and anti-correlates with  $R_{\text{vir}}$  and  $\rho$ , respectively.
3. The mean and maximal  $EW$  of absorbers increase with decreasing  $\Delta v$ . The strongest absorbers are nearly all found within  $\Delta v = \pm 100$  km s $^{-1}$  of their associated galaxies.
4. Ly $\alpha$  absorbers are most commonly associated with inclined galaxies. 73% of blueshifted and 77% of redshifted absorbers are associated with galaxies with  $i \geq 50$  deg, whereas 56% of all galaxies in the survey volume have similarly high inclinations.

The distributions of associated versus all galaxy inclinations differ at a greater than 99% confidence, or  $\sim 3.6\sigma$  level, according to the Anderson-Darling distribution test.

5. We find no strong evidence for azimuth preference for absorption - Ly $\alpha$  absorbers appear to be distributed uniformly around galaxy major and minor axes.

In a future paper we will apply this method to a sample of hundreds of COS sightlines in an effort to produce the most statistically robust CGM study to date.

We would like to thank the referee for his/her valuable comments and suggestions. This research has made use of the NASA/IPAC Extragalactic Database (NED) which is operated by the Jet Propulsion Laboratory, California Institute of Technology, under contract with the National Aeronautics and Space Administration. This work is based on observations with the NASA/ESA *Hubble Space Telescope*, obtained at the Space Telescope Science Institute (STScI), which is operated by the Association of Universities for Research in Astronomy, Inc., under NASA contract NAS 5-26555. Spectra were retrieved from the Barbara A. Mikulski Archive for Space Telescopes (MAST) at STScI. Over the course of this study, D.M.F. and B.P.W. were supported by grant AST-1108913, awarded by the US National Science Foundation, and by NASA grants *HST*-AR-12842.01-A, *HST*-AR-13893.01-A, and *HST*-GO-14240 (STScI).

## References

- Bauermeister, A., Blitz, L., & Ma, C.-P. 2010, The Astrophysical Journal, 717, 323  
 Borthakur, S., Heckman, T., Tumlinson, J., et al. 2015, ApJ, 813, 46  
 Chen, H.-W., Lanzetta, K. M., Webb, J. K., & Barcons, X. 1998, ApJ, 498, 77  
 —. 2001, ApJ, 559, 654  
 Churchill, C. W., Nielsen, N. M., Kacprzak, G. G., & Trujillo-Gomez, S. 2013, ApJL, 763, L42

- Churchill, C. W., Vander Vliet, J. R., Trujillo-Gomez, S., Kacprzak, G. G., & Klypin, A. 2015, ApJ, 802, 10
- Côté, S., Wyse, R. F. G., Carignan, C., Freeman, K. C., & Broadhurst, T. 2005, ApJ, 618, 178
- Danforth, C. W., & Shull, J. M. 2008, ApJ, 679, 194
- Erb, D. K. 2008, ApJ, 674, 151
- Genzel, R., Tacconi, L. J., Gracia-Carpio, J., et al. 2010, Monthly Notices of the Royal Astronomical Society, 407, 2091
- Green, J. C., Froning, C. S., Osterman, S., et al. 2012, ApJ, 744, 60
- Heidmann, J., Heidmann, N., & de Vaucouleurs, G. 1972, MmRAS, 75, 85
- Jarrett, T. H., Chester, T., Cutri, R., Schneider, S. E., & Huchra, J. P. 2003, AJ, 125, 525
- Jester, S., Schneider, D. P., Richards, G. T., et al. 2005, AJ, 130, 873
- Jones, H., Davies, J. I., & Trewhella, M. 1996, MNRAS, 283, 316
- Kacprzak, G. G., Churchill, C. W., Evans, J. L., Murphy, M. T., & Steidel, C. C. 2011, MNRAS, 416, 3118
- Kacprzak, G. G., Churchill, C. W., & Nielsen, N. M. 2012, ApJL, 760, L7
- Lanzetta, K. M., Bowen, D. V., Tytler, D., & Webb, J. K. 1995, ApJ, 442, 538
- Lehner, N., Savage, B. D., Richter, P., et al. 2007, ApJ, 658, 680
- Liang, C. J., & Chen, H.-W. 2014, MNRAS, 445, 2061
- Marzke, R. O., Huchra, J. P., & Geller, M. J. 1994, ApJ, 428, 43
- Mathes, N. L., Churchill, C. W., Kacprzak, G. G., et al. 2014, ApJ, 792, 128
- Osterman, S., Green, J., Froning, C., et al. 2011, Ap&SS, 335, 257
- Penton, S. V., Stocke, J. T., & Shull, J. M. 2002, ApJ, 565, 720
- . 2004, ApJS, 152, 29
- Prochaska, J. X., Weiner, B., Chen, H.-W., Mulchaey, J., & Cooksey, K. 2011, ApJ, 740, 91
- Prochaska, J. X., Weiner, B. J., Chen, H.-W., & Mulchaey, J. S. 2006, ApJ, 643, 680
- Prochaska, J. X., & Wolfe, A. M. 2009, The Astrophysical Journal, 696, 1543
- Putman, M. E., Peek, J. E. G., & Heitsch, F. 2009a, ArXiv e-prints, arXiv:0907.1023

- Putman, M. E., Henning, P., Bolatto, A., et al. 2009b, in *Astronomy, Vol. 2010, astro2010: The Astronomy and Astrophysics Decadal Survey*, 241
- Rudie, G. C., Steidel, C. C., Trainor, R. F., et al. 2012, *ApJ*, 750, 67
- Savage, B. D., Kim, T.-S., Wakker, B. P., et al. 2014, *ApJS*, 212, 8
- Shull, J. M., Smith, B. D., & Danforth, C. W. 2012, *ApJ*, 759, 23
- Steidel, C. C., Erb, D. K., Shapley, A. E., et al. 2010, *ApJ*, 717, 289
- Stocke, J. T., Keeney, B. A., Danforth, C. W., et al. 2013, *ApJ*, 763, 148
- . 2014, *ApJ*, 791, 128
- Tejos, N., Morris, S. L., Finn, C. W., et al. 2014, *MNRAS*, 437, 2017
- Thom, C., Tumlinson, J., Werk, J. K., et al. 2012, *ApJL*, 758, L41
- Tripp, T. M., Lu, L., & Savage, B. D. 1998, *ApJ*, 508, 200
- Tumlinson, J., Werk, J. K., Thom, C., et al. 2011, *ApJ*, 733, 111
- Tumlinson, J., Thom, C., Werk, J. K., et al. 2013, *ApJ*, 777, 59
- Wakker, B. P., Hernandez, A. K., French, D. M., et al. 2015, *ApJ*, 814, 40
- Wakker, B. P., & Savage, B. D. 2009, *ApJS*, 182, 378
- Wakker, B. P., Savage, B. D., Sembach, K. R., et al. 2003, *ApJS*, 146, 1
- Werk, J. K., Prochaska, J. X., Tumlinson, J., et al. 2014, *ApJ*, 792, 8

## Chapter 4

# EVIDENCE FOR A ROTATIONAL COMPONENT IN THE CGM OF NEARBY GALAXIES

*To be submitted to the Astrophysical Journal*

## Abstract

We present results of a study comparing the velocity of Ly $\alpha$  absorbers relative to the rotation direction and velocity of nearby galaxy disks in the nearby Universe ( $z \leq 0.03$ ). We have obtained rotation curves via long-slit spectroscopy of 12 galaxies with the Southern African Large Telescope, and combine this dataset with an additional 17 galaxies with published rotation curves from the literature. Each galaxy appears within  $3R_{\text{vir}}$  of a QSO with available Cosmic Origin Spectrograph (COS) data covering the relevant Ly $\alpha$  wavelength range. We present a simple cylindrical galaxy halo rotation model to interpret these data in the context of probing three-dimensional galaxy halos via 1-dimensional QSO absorption-line spectroscopy. Relative to this model we find that up to 63% of Ly $\alpha$  absorbers are consistent with co-rotation. Intriguingly, the Ly $\alpha$  co-rotation fraction decreases with both virial radius, scaled impact parameter ( $\rho/R_{\text{vir}}$ ), and galaxy luminosity ( $L^*$ ) in a model independent fashion. Finally, we report that both anti-rotating absorbers and those found near luminous galaxies ( $L \gtrsim 0.6L^*$ ) mostly have low Doppler b-parameters ( $b \lesssim 50 \text{ km s}^{-1}$ ). Co-rotating absorbers show a wide range of b-parameters. These results are broadly in agreement with the co-rotation fractions predicted by the Stewart et al. (2011b) simulations, and furthermore provides some of the first observational evidence for cold-mode accretion onto sub- $L^*$  galaxies in the low- $z$  Universe.

## 4.1 INTRODUCTION

Our current Lambda Cold-Dark-Matter ( $\Lambda$ CDM) cosmology picture describes galaxies forming hierarchically out of overdensities in the underlying dark matter distribution. As the surrounding intergalactic medium (IGM) is funneled toward a growing galaxy, simulations predict the angular momentum of the inflowing gas is redistributed onto the disk and seeds the overall rotation of the galaxy (e.g., Stewart et al. 2011a; Chen et al. 2003; Sharma & Steinmetz 2005; Brook et al. 2011; Kimm et al. 2011; Pichon et al. 2011; Stewart et al. 2013). As this infalling gas is responsible for birthing and continuing to feed the galaxies throughout their lifetimes, it is expected that the extended gaseous halos should rotate in the same sense as both the galactic disks and dark matter halos.

In the  $\Lambda$ CDM picture, accretion falls broadly into two types. In the so-called “hot-mode”, gas shock-heats at the virial radius as it encounters the galaxy halo. The inner, more dense region of this hot gaseous halo then rains down onto the disk as it radiatively cools (e.g., Fillmore & Goldreich 1984; Bertschinger 1985; Danovich et al. 2012; Shen et al. 2013). However, most gas arrives cold ( $T \sim 10^4$  K) from the IGM, and the proposed radiative shock is unstable to cooling. Thus this hot-halo scenario may not actually be created (Birnboim & Dekel 2003; Kereš et al. 2005; Ocvirk et al. 2008; Brooks et al. 2009; Dekel et al. 2009).

In contrast, as part of the alternative “cold-mode” accretion model, filaments of gas from the IGM should merge smoothly with the disk, thus converting a significant fraction of their infall velocity to rotational velocity of the galaxy (Kereš et al. 2005; Stewart et al. 2017). The simulations of Powell et al. (2011) agreed with these conjectures by showing that indeed, the accreting filaments connect rather smoothly to the disc, even in the presence

of strong supernova driven winds. This cold-mode of accretion likely dominates the global growth of all but the most massive halos at high redshifts ( $z \gtrsim 3$ ), and the growth of lower mass ( $M_{\text{halo}} \leq 5 \times 10^{11} M_*$ ) objects at late times (Dekel & Birnboim 2006; van de Voort et al. 2011). Furthermore, cosmological SPH simulations such as those by Stewart et al. (2011b, 2013) suggests that halo gas should co-rotate with disk-gas out to at least 100 kpc, and that absorption in intervening QSO sightlines should be able to accurately capture this rotation signature.

Some observational evidence of cold-mode accretion has been obtained at higher redshifts. In pioneering studies focusing on the Mg II absorber kinematics and their connection with neighboring galaxies, Charlton & Churchill (1998); Steidel et al. (2002), and later Kacprzak et al. (2010); Ho et al. (2017), find tantalizing evidence that a significant fraction of Mg II absorbers have velocities that can be explained by an extended gaseous disk. Additionally, Diamond-Stanic et al. (2016) detect co-rotating H $\alpha$  emission and Mg II and Fe II absorption toward a Milky Way-like galaxy at  $z = 0.413$ . However, as noted by Steidel et al. (2002), a simple extended disk model is insufficient to explain the observed bulk motion implied by their sample of 5 Mg II absorber-galaxy systems, and a rotating *halo* may be a better model.

Additionally, the picture may have changed since  $z \sim 0.5$ , the epoch 5 Gyr ago that most of these Mg II systems are probing. By  $z \sim 0$  simulations (e.g., Kereš et al. 2005; Stewart et al. 2017) predict a drop-off in cold-mode accretion and a decrease in the density of IGM filaments. Observational confirmation has been even more inconclusive in this low-redshift regime. In the largest such study, involving Ly $\alpha$  absorber-galaxy kinematics, Côté et al. (2005) probed the halos of nine galaxies using *HST* observed background QSOs, and found that large warps would be needed to explain the velocity of H I absorbers by an extended rotating disk. Wakker & Savage (2009) compiled a sample of 76 sightlines,

which included only 4 galaxy-QSO systems for which the galaxy’s rotation curve was known from the literature, and finding only 1/4 of Ly $\alpha$  absorbers appeared to co-rotate with the associated galaxy disk. Similarly, Kacprzak et al. (2011) claim a reduction in Mg II co-rotation around  $\sim L^*$  galaxies between  $z \sim 0.5$  and  $z \sim 0.1$ . Approaching the question from a different angle, Bowen et al. (2016) probed the halo of a single galaxy, NGC1097, with 4 nearby QSO sightlines, and suggests that an extended, slowly rotating disk with additional inflowing IGM material best matches observations.

To significantly improve observational statistics in this low-redshift regime, we have obtained rotation curves from the Souther African Large Telescope (SALT) for 12 nearby spiral galaxies which are located within  $3R_{\text{vir}}$  kpc of a background QSO observed by the Cosmic Origins Spectrograph (COS) on *HST*. A literature search yielded an additional 17 galaxies with published rotation curves and known orientations. Each of these is probed by at least one QSO within  $3R_{\text{vir}}$ .

In Section 4.2 we describe the selection and reduction of both SALT and COS spectra. In Section 4.3 we present a new rotating halo model we have developed to aid in the interpretation of our observations. In Section 4.4 we discuss the overall results of this exercise and present a physically-motivated interpretation of these results. See Section 4.5 for a summary of our results and conclusions. Each galaxy-QSO system is discussed in detail in Appendix A.

Table 4.1. SALT Galaxy Observations

Galaxy	R.A.	Dec.	Measured $v_{\text{sys}}$ (km s $^{-1}$ )	Published $v_{\text{sys}}$ (km s $^{-1}$ )	Type	$v_{\text{rot}}$ (km s $^{-1}$ )	$v_{\text{rot}}/\sin(i)$ (km s $^{-1}$ )	Obs. Date	$T_{\text{exp}}$ (ks)
(1)	(2)	(3)	(4)	(5)	(6)	(7)	(8)	(9)	(10)
CGCG039-137	11 21 27.0	+03 26 41.7	6918 ± 24	6902 ± 52 <sup>a</sup>	Scd	132 ± 16	139 ± 26	05 11 2016	700
ESO343-G014	21 37 45.2	-38 29 33.2	9139 ± 32	9162 ± 45 <sup>b</sup>	S	203 ± 32	203 ± 32	05 16 2016	1000
IC5325	23 28 43.4	-41 20 00.5	1512 ± 8	1503 ± 7 <sup>c</sup>	SAB(rs)bc	53 ± 5	125 ± 39	05 17 2016	600
MCG-03-58-009	22 53 40.9	-17 28 44.0	9015 ± 19	9030 ± 10 <sup>d</sup>	Sc	150 ± 12	171 ± 23	05 16 2016	1200
NGC1566	04 20 00.4	-54 56 16.1	1502 ± 15	1504 ± 2 <sup>e</sup>	SAB(rs)bc	64 ± 8	195 ± 47	10 18 2016	400
NGC3513	11 03 46.1	-23 14 43.8	1204 ± 12	1194 ± 7 <sup>c</sup>	SB(s)c	11 ± 10	22 ± 24	05 26 2016	600
NGC3633	11 20 26.2	+03 35 08.2	2587 ± 7	2600 ± 2 <sup>f</sup>	SAa	149 ± 6	157 ± 9	05 11 2016	1200
NGC4536	12 34 27.1	+02 11 17.3	1867 ± 33	1808 ± 19 <sup>g</sup>	SAB(re)bc	129 ± 9	148 ± 41	05 11 2016	1300
NGC4939	13 04 14.4	-10 20 22.6	3093 ± 33	3110 ± 4 <sup>e</sup>	SA(s)bc	204 ± 25	275 ± 66	05 14 2016	500
NGC5364	13 56 12.0	+05 00 52.1	1238 ± 17	1241 ± 4 <sup>c</sup>	SA(rs)bc pec	130 ± 13	155 ± 22	05 11 2016	700
NGC5786	14 58 56.3	-42 00 48.1	2975 ± 22	2998 ± 5 <sup>h</sup>	SAB(s)bc	156 ± 10	172 ± 25	05 11 2016	250
UGC09760	15 12 02.4	+01 41 55.5	2094 ± 16	2023 ± 2 <sup>i</sup>	Sd	46 ± 10	46 ± 16	05 11 2016	500

Note. — SALT targeted galaxies. Columns are as follows: 1) the galaxy name, 2), 3) R.A., Dec. in J2000, 4) measured galaxy systemic velocity, 5) published galaxy systemic velocity, 6) morphological type (RC3), 7) approaching side velocity, 8) receding side velocity, 9) observation date, and 10) exposure time. All observations used the RSS PG2300 grating.

References. — a. Abazajian et al. (2005); b. Jones et al. (2009); c. Corwin et al. (1994); d. Mathewson & Ford (1996); e. Koribalski et al. (2004); f. Lu et al. (1993); g. Grogan et al. (1998); h. di Nella et al. (1996); i. Giovanelli et al. (1997)

Table 4.2. Summary of QSO Sample

Target	Galaxy	R.A.	Dec.	z	Program	$T_{\text{exp}}$ (ks)
1H0419-577	NGC1566	04 26 00.7	-57 12 02.0	0.10400	11686	20429
2E1530+1511	NGC5951	15 33 14.3	+15 01 03.0	0.09000	14071	9348
3C232	NGC3067	09 58 20.9	+32 24 02.0	0.53060	8596	44662
3C273.0	NGC4536	12 29 06.7	+02 03 09.0	0.15834	12038	4002
CSO295	NGC3432	10 52 05.6	+36 40 40.0	0.60900	14772	1088
CSO1208	NGC3726	11 40 47.9	+46 22 05.0	0.11500	14729	3052
FBQSJ0908+3246	NGC2770	09 08 38.8	+32 46 20.0	0.25989	14240	7430
H1101-232	NGC3513	11 03 37.7	-23 29 31.0	0.18600	12025	13341
HE0429-5343	NGC1566	04 30 40.0	-53 36 56.0	0.04001	12275	2067
HE1228+0131	NGC4536	12 30 50.0	+01 15 23.0	0.11700	11686	11036
MRC2251-178	MCG-03-58-009	22 54 05.9	-17 34 55.0	0.06609	12029	5515
MRK335	NGC7817	00 06 19.5	+20 12 11.0	0.02578	11524	5122
MRK771	NGC4529	12 32 03.6	+20 09 30.0	0.06301	12569	1868
MRK876	NGC6140	16 13 57.2	+65 43 11.0	0.12900	11524	12579
PG0804+761	UGC04238	08 10 58.7	+76 02 43.0	0.10200	11686	5510
PG1259+593	UGC08146	13 01 12.9	+59 02 07.0	0.47780	11541	9200
PG1302-102	NGC4939	13 05 33.0	-10 33 19.0	0.27840	12038	5979
QSO1500-4140	NGC5786	15 03 34.0	-41 52 23.0	0.33500	11659	9258
RBS1503	NGC5907	15 29 07.5	+56 16 07.0	0.09900	12276	1964
RBS1768	ESO343-G014	21 38 49.9	-38 28 40.0	0.18299	12936	6962
RBS2000	IC5325	23 24 44.7	-40 40 49.0	0.17359	13448	5046
RX_J1017.5+4702	NGC3198	10 17 31.0	+47 02 25.0	0.33544	13314	8655
RX_J1054.2+3511	NGC3432	10 54 16.2	+35 11 24.0	0.20300	14772	533
RX_J1117.6+5301	NGC3631	11 17 40.5	+53 01 51.0	0.15871	14240	4943
RX_J1121.2+0326	CGCG039-137, NGC3633	11 21 14.0	+03 25 47.0	0.15200	12248	2695
RX_J1142.7+4625	NGC3726	11 42 41.2	+46 24 36.0	0.11500	14772	2368
RX_J1236.0+2641	NGC4565	12 36 04.0	+26 41 36.0	0.20920	12248	4235
SBS1116+523	NGC3631	11 19 47.9	+52 05 53.0	0.35568	14240	4949

## 4.2 DATA AND ANALYSIS

### 4.2.1 SALT Data

Our sample contains 12 galaxies observed with the Southern African Large Telescope (SALT) Robert Stobie Spectrograph (RSS) in longslit mode (Burgh et al. 2003; Kobulnicky et al. 2003; Buckley et al. 2006; O’Donoghue et al. 2006). These 12 were selected from a larger pool of 48 submitted targets by the SALT observing queue. These 48 possible targets were chosen for their proximity to background QSOs whose spectra contained promising Ly $\alpha$  lines. Finally, we only included galaxies with  $z \leq 0.33$  ( $cz \leq 10,000$  km s $^{-1}$ ), angular sizes less than 6' to enable easy sky subtraction without taking additional exposures, and surface brightnesses sufficient to keep exposure times below  $\sim 1300$ s. Table 4.1 summarizes these observations. Data was taken for 2 additional galaxies, NGC3640 and NGC2962, but proved unusable due to issues with spectral identification and low signal-to-noise (respectively).

All SALT galaxy spectra were reduced and extracted using the standard PySALT reduction package (Crawford et al. 2010)<sup>1</sup>, which includes procedures to prepare the data, correct for gain, cross-talk, bias, and overscan, and finally mosaic the images from the 3 CCDs. Next, we rectify the images with wavelength solutions found via Ne and Ar arc lamp spectra line identification. Finally, we perform a basic sky subtraction using an off-sky portion of the spectrum, and extract 5-10 pixel wide 1-D strips from the reduced 2-D spectrum.

For each 1-D spectrum, we identify the H $\alpha$  emission lines and perform a non-linear

---

<sup>1</sup><http://pysalt.salt.ac.za/>

Table 4.2 (cont'd)

Target	Galaxy	R.A.	Dec.	z	Program	$T_{\text{exp}}$ (ks)
SBS1503+570	NGC5907	15 04 55.6	+56 49 20.0	0.35894	12276	5163
SDSSJ091052.80+333008.0	NGC2770	09 10 52.8	+33 30 08.0	0.11631	14240	7442
SDSSJ091127.30+325337.0	NGC2770	09 11 27.3	+32 53 37.0	0.29038	14240	10028
SDSSJ095914.80+320357.0	NGC3067	09 59 14.8	+32 03 57.0	0.56462	12603	2273
SDSSJ104335.90+115129.0	NGC3351	10 43 35.9	+11 05 29.0	0.79400	14071	4736
SDSSJ111443.70+525834.0	NGC3631	11 14 43.7	+52 58 34.0	0.07921	14240	13440
SDSSJ112439.50+113117.0	NGC3666	11 24 39.4	+11 31 17.0	0.14300	14071	10427
SDSSJ112448.30+531818.0	UGC06446, NGC3631	11 24 48.3	+53 18 19.0	0.53151	14240	7920
SDSSJ135726.27+043541.4	NGC5364	13 57 26.3	+04 35 41.0	1.23453	12264	14148
SDSSJ151237.15+012846.0	UGC09760	15 12 37.2	+01 28 46.0	0.26625	12603	7590
TON1009	NGC2770	09 09 06.2	+32 36 30.0	0.81028	12603	4740
TON1015	NGC2770	09 10 37.0	+33 29 24.0	0.35400	14240	4774

Note. — Summary of COS targets in this sample.  $T_{\text{exp}}$  gives the total G130M integration time if multiple exposures were taken.

least-squares Voigt profile fit using the Python package LMFIT<sup>2</sup>. The line centroid and  $1\sigma$  standard errors are returned, and these fits are then shifted to rest-velocity based on the galaxy systemic redshift and heliocentric velocity corrections are calculated with the IRAF rvcorrect procedure. The final rotation velocity is calculated by then applying the inclination correction,  $v_{rot} = v / \sin(i)$ . Final errors are calculated as a quadrature sum of  $1\sigma$  fit errors, systemic redshift error, and inclination uncertainty as follows:

$$\begin{aligned}\sigma^2 = & \left( \frac{\partial v_{rot}}{\partial \lambda_{obs}} \right)^2 (\Delta \lambda_{obs})^2 + \\ & \left( \frac{\partial v_{rot}}{\partial v_{sys}} \right)^2 (\Delta v_{sys})^2 + \\ & \left( \frac{\partial v_{rot}}{\partial i} \right)^2 (\Delta i)^2,\end{aligned}\quad (4.1)$$

where  $\Delta \lambda_{obs}$ ,  $\Delta v_{sys}$ , and  $\Delta i$  are the errors in observed line center, galaxy redshift, and inclination, respectively.

We determine the inclination error by calculating the standard deviation of the set of all axis ratio values available in NED for each galaxy. The final physical scale is calculated using the SALT image scale of 0.1267 arcsec/pixel, multiplied by the 4-pixel spatial binning, and converted to physical units using a redshift-independent distance if available, and a Hubble flow estimate if not. We adopt a Hubble constant of  $H_0 = 71 \text{ km s}^{-1} \text{ Mpc}^{-1}$  throughout.

Finally, we calculate our approaching and receding velocities via a weighted mean of the outer 1/2 of each rotation curve, with errors calculated as weighted standard errors in the mean. Our final redshifts are calculated by forcing symmetric rotation, such that the outer 1/2 average velocity for each side matches in magnitude. The upper-left panel

---

<sup>2</sup><http://cars9.uchicago.edu/software/python/lmfit/contents.html>

of Figure 4.1 shows an example of this; the black points and error bars are the observed rotation measurements, the dark green lines show the average rotation velocity for the outer 1/2 edge of each rotation curve, and the green shading shows the  $1\sigma$  error for this average value. See Appendix A for rotation curves and slit-position charts for each observed galaxy.

#### 4.2.2 COS Spectra

The Barbara A. Mikulski Archive for Space Telescopes (MAST) archives yield 19 QSO targets observed by COS which lie within 500 kpc of our SALT galaxies. These targets vary widely in signal-to-noise from approximately 5 to 100 due to our choosing them based only on their proximity to galaxies with known rotation. The reduction procedure for these spectra follow those described by Wakker et al. (2015) and French & Wakker (2017). In short, spectra are processed with CALCOS v3.0 or higher and are aligned using a cross-correlation, and then shifted to make sure that (a) the velocities of the interstellar lines match the 21-cm HI profile, and (b) the velocities of lines in a single absorption system line up properly. Multiple exposures are combined by summing total counts per pixel before converting to flux. The COS instrument is described in detail by Green et al. (2012).

Once reduced we make a fourth-order or lower polynomial continuum fit in the region around each absorption line (typically within a  $4000 \text{ km s}^{-1}$  window around each line) and measure integrated equivalent widths. To recover accurate Doppler  $b$ -parameter measurements, we then fit a Voigt profile to each line using the VoigtFit package by Krogager (2018). The VoigtFit routine takes into account instrumental broadening by assuming a Gaussian with FWHM equal to the instrument spectral resolution (typically  $17 \text{ km s}^{-1}$  for these COS spectra).

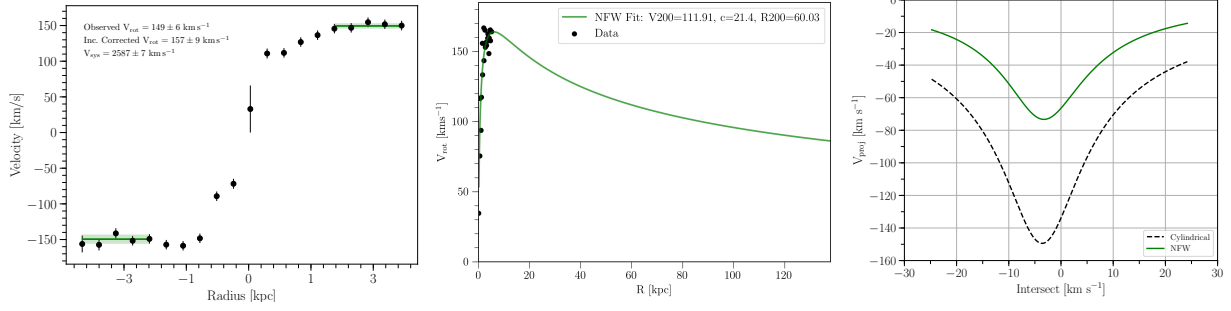


**Figure 4.1 :** Left: The rotation curve for NGC3633 is shown in black, with the outer 1/2 mean rotation velocity indicated in green. Our cylindrical model simply extends this green average velocity out to  $3R_{\text{vir}}$ . Middle: The observed rotation curve is again shown in black, with an NFW profile fit overlaid in green. Right: The model velocity predictions for the cylindrical and NFW models are shown in dashed-black and solid-green (respectively).

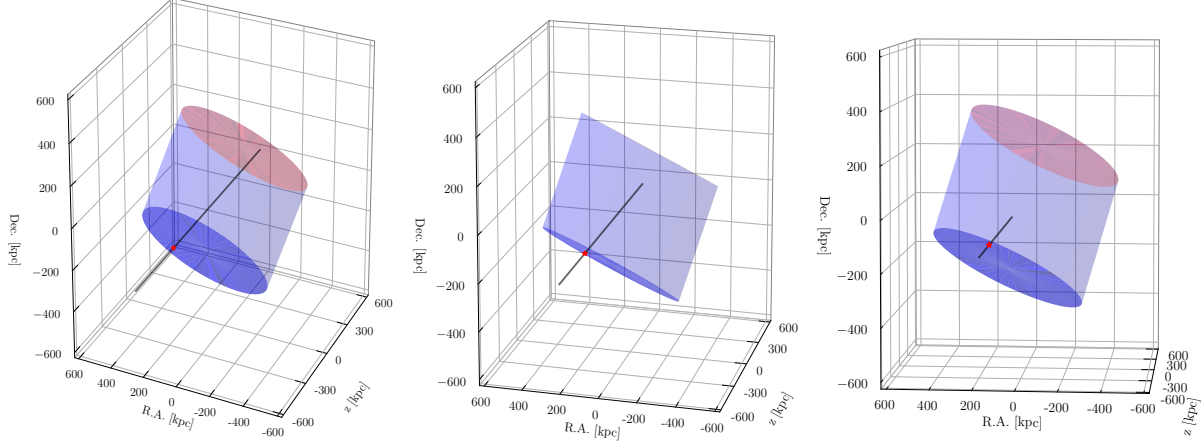


**Figure 4.2 :** A 3D example mockup of our halo rotation model showing the orientation and extent of the NGC3633 model from 3 different viewing angles. The approaching extreme edge of the NGC3633 cylindrical halo is shown by dark-blue oval, with the far edge shown in red. The dark-grey line shows the location of the sightline toward RX\_J1121.2+0326 as it penetrates the halo, with a red star marking the first intercept point.

### 4.3 Halo Rotation Model

In order to better understand how QSO sightlines probe the intervening velocity structure we have developed a simple halo gas rotation model. This model is seeded by an observed rotation curve, which is then extrapolated out to a radius of  $3R_{\text{vir}}$  and height of  $2R_{\text{vir}}$  to form a coherently rotating halo. For each galaxy-QSO pair we created 2 rotation models: 1) a purely cylindrical halo with constant velocity, and 2) a cylindrical model with rotation velocities which smoothly decline based on a Navarro-Frenk-White (NFW) profile fit (Navarro et al. 1996, 1997) as a function of radius.

For the first, purely cylindrical model, the input rotation curve is interpolated via linear spline and extended out to  $3R_{\text{vir}}$  based on the average velocity of the outer 1/2 radius (see Figure 4.1). For the second model, we fit an NFW rotation velocity profile to the input rotation curve. The form of this fit is as follows:

$$V(R) = V_{200} \left[ \frac{\ln(1 + cx) - cx/(1 + cx)}{x[\ln(1 + c) - c/(1 + c)]} \right]^{\frac{1}{2}}, \quad (4.2)$$

where  $x = R/R_{200}$ , with  $R_{200}$  being the radius at which the density contrast with respect to the critical density of the universe exceeds 200,  $c = R_{200}/R_s$ , with  $R_s$  being the characteristic radius of the halo, and  $V_{200}$  being the characteristic velocity at  $R_{200}$ . We have taken this form from de Blok et al. (2008). The resulting NFW fits tend to be somewhat poor toward the inner parts of the rotation curve (as has been noted by others, e.g., Côté et al. 2005). Regardless, we are most interested in achieving a physically-motivated velocity profile in the outer halo regions, for which these fits are certainly adequate.

Next, we project this interpolated rotation curve onto a plane oriented to a mock QSO sightline identically to the input galaxy-QSO pair orientation. By stacking multiple rotation-planes in the galaxy z-axis direction, we then create a simple cylindrical halo

model embedded with the fit and extrapolated rotation curve. Finally, each rotation-plane in the stack is projected onto the mock sightline. The result is a function representing the rotation velocity encountered by the sightline as a function of velocity (i.e., distance) along it. Each model produces the velocity a co-rotating absorber would project onto the spectrum as a function of velocity along the sightline. We then collapse this into the range of possible observed velocities by summing the x- and y-components along the allowed range. This has the effect of combining *both* the projected rotation velocity *and* the physical velocity separation between an absorber and the galaxy’s heliocentric velocity ( $\Delta v = v_{\text{absorber}} - v_{\text{galaxy}}$ ) into a single velocity range, which we then can compare to the measured absorption velocity ( $v_{\text{Ly}\alpha}$ ).

Figures 4.1 and 4.2 illustrate an example rotation curve for our SALT galaxy NGC3633 with our linear-spline and NFW fits, a 3-dimension halo mockup from 3 different viewing angles, and the resulting cylindrical and NFW model output velocity distributions. In most cases, and as seen in this example, the two model outputs have similar *shape*, but the NFW profile fit usually results in a lower velocity range (i.e., closer to systemic). Because we combine projected velocity with velocity along the sightline, many models allow for an absorber to have the wrong sign of  $\Delta v$ . For example, an absorber on the approaching side of a halo but at the distant edge would end up with a range of positive  $\Delta v$  consistent with co-rotation because the relatively positive redshift component overcomes the relatively negative rotation component. The result is that some absorbers with the “wrong” on-sky velocity for co-rotation are indeed consistent with co-rotation based on our model results.

Table 4.3. Halo Model Results and Ly $\alpha$  Absorption Properties

#	Galaxy	Target	$\rho$ (kpc)	Az. (deg)	$v_{\text{sys}}$ (km s $^{-1}$ )	$v_{\text{rot}}^{\text{a}}$ (km s $^{-1}$ )	$v_{\text{Ly}\alpha}$ (km s $^{-1}$ )
1	CGCG039-137	RX_J1121.2+0326	99	71	6918	139	6975
2	ESO343-G014	RBS1768	466	74	9139	205	9308
2	ESO343-G014	RBS1768	466	74	9139	205	9360
2	ESO343-G014	RBS1768	466	74	9139	205	9434
3	IC5325	RBS2000	314	64	1512	-125	1598
4	MCG-03-58-009	MRC2251-178	355	71	9015	171	9029
5	NGC1566	1H0419-577	303	10	1502	86	1075
5	NGC1566	1H0419-577	303	10	1502	86	1123
5	NGC1566	1H0419-577	303	10	1502	86	1188
5	NGC1566	1H0419-577	303	10	1502	86	1264
5	NGC1566	1H0419-577	303	10	1502	86	2020
6	NGC1566	HE0429-5343	256	60	1502	-86	1167
6	NGC1566	HE0429-5343	256	60	1502	-86	1358
7	NGC2770	FBQSJ0908+3246	204	59	1948	150	1915
7	NGC2770	FBQSJ0908+3246	204	59	1948	150	1982
8	NGC2770	TON1009	267	41	1948	150	1908
8	NGC2770	TON1009	267	41	1948	150	1980
9	NGC2770	TON1015	218	61	1948	150	1833
9	NGC2770	TON1015	218	61	1948	150	1985
10	NGC2770	SDSSJ091052.80+333008.0	239	66	1948	150	1824
10	NGC2770	SDSSJ091052.80+333008.0	239	66	1948	150	1975
11	NGC2770	SDSSJ091127.30+325337.0	234	30	1948	150	2063
12	NGC3067	3C232	11	74	1465	148.2	1408
12	NGC3067	3C232	11	74	1465	148.2	1510
12	NGC3067	3C232	11	74	1465	148.2	1641
13	NGC3067	SDSSJ095914.80+320357.0	128	43	1465	148.2	1493
14	NGC3198	RX_J1017.5+4702	370	55	660	152	629
15	NGC3351	SDSSJ104335.90+115129.0	31	43	778	198	717
15	NGC3351	SDSSJ104335.90+115129.0	31	43	778	198	882
15	NGC3351	SDSSJ104335.90+115129.0	31	43	778	198	1030
16	NGC3432	CSO295	20	82	616	122	600
16	NGC3432	CSO295	20	82	616	122	662

Table 4.3 (cont'd)

#	Galaxy	Target	$\rho$ (kpc)	Az. (deg)	$v_{\text{sys}}$ (km s $^{-1}$ )	$v_{\text{rot}}^{\text{a}}$ (km s $^{-1}$ )	$v_{\text{Ly}\alpha}$ (km s $^{-1}$ )	$W_{\text{Ly}\alpha}$ (mÅ)
17	NGC3432	RX_J1054.2+3511	290	57	616	122	703	184
18	NGC3513	H1101-232	60	67	1204	20	1182	635
19	NGC3631	RX_J1117.6+5301	78	75	1156	145	1131	374
19	NGC3631	RX_J1117.6+5301	78	75	1156	145	1259	62
20	NGC3631	SBS1116+523	163	40	1156	145	-99	-99
21	NGC3631	SDSSJ111443.70+525834.0	145	72	1156	145	1163	232
22	NGC3631	SDSSJ112448.30+531818.0	86	74	1156	145	1019	71
22	NGC3631	SDSSJ112448.30+531818.0	86	74	1156	145	1141	165
23	NGC3633	RX_J1121.2+0326	184	58	2587	-157	2605	180
24	NGC3666	SDSSJ112439.50+113117.0	58	83	1060	131.8	1047	345
24	NGC3666	SDSSJ112439.50+113117.0	58	83	1060	131.8	1099	272
25	NGC3726	CSO1208	369	88	866	167.2	731	470
25	NGC3726	CSO1208	369	88	866	167.2	874	506
26	NGC3726	RX_J1142.7+4625	440	86	866	167.2	818	375
27	NGC4529	MRK771	159	23	2536	106.4	2553	240
28	NGC4536	3C273.0	349	11	1867	139	1580	369
28	NGC4536	3C273.0	349	11	1867	139	2156	42
28	NGC4536	3C273.0	349	11	1867	139	2267	27
29	NGC4536	HE1228+0131	338	51	1867	139	1495	160
29	NGC4536	HE1228+0131	338	51	1867	139	1571	23
29	NGC4536	HE1228+0131	338	51	1867	139	1686	321
29	NGC4536	HE1228+0131	338	51	1867	139	1721	303
29	NGC4536	HE1228+0131	338	51	1867	139	1854	78
30	NGC4565	RX_J1236.0+2641	147	41	1230	253	1009	365
30	NGC4565	RX_J1236.0+2641	147	41	1230	253	1166	305
30	NGC4565	RX_J1236.0+2641	147	41	1230	253	1254	122
31	NGC4939	PG1302-102	254	61	3093	-275	3448	72
32	NGC5364	SDSSJ135726.27+043541.4	165	84	1238	55	967	348
32	NGC5364	SDSSJ135726.27+043541.4	165	84	1238	55	1124	83
33	NGC5786	QSO1500-4140	453	1	2975	172	3138	177
34	NGC5907	SBS1503+570	413	47	667	227.4	708	301
35	NGC5907	RBS1503	478	63	667	227.4	-99	-99

## 4.4 Discussion

We present data on 41 QSO-galaxy systems, representing 65 individual Ly $\alpha$  component-galaxy matchups, for which we have galaxy information including kinematics, inclination, size and luminosity. This is the largest sample of this kind to date and provides the best yet opportunity to study the kinematic connection between galaxies and their neutral H I halos.

Table 4.4 summarizes our galaxy-absorber sample and the predicted velocity range given by each model for co-rotation. Unfortunately our sample contains a large number of high-azimuth targets (i.e., the QSO lies close to the projected galaxy minor axis). These high-azimuth systems are inherently uncertain. For even the most edge-on galaxies,

Table 4.3 (cont'd)

#	Galaxy	Target	$\rho$ (kpc)	Az. (deg)	$v_{\text{sys}}$ (km s $^{-1}$ )	$v_{\text{rot}}^{\text{a}}$ (km s $^{-1}$ )	$v_{\text{Ly}\alpha}$ (km s $^{-1}$ )	$W_{\text{Ly}\alpha}$ (mÅ)
36	NGC5951	2E1530+1511	55	85	1780	127.9	1795	50
36	NGC5951	2E1530+1511	55	85	1780	127.9	1953	13
37	NGC6140	MRK876	113	21	910	138.11	939	37
38	NGC7817	MRK335	343	90	2309	180.4	1954	21
38	NGC7817	MRK335	343	90	2309	180.4	2274	15
39	UGC04238	PG0804+761	148	59	1544	91.6	1526	6
39	UGC04238	PG0804+761	148	59	1544	91.6	1593	3
40	UGC06446	SDSSJ112448.30+531818.0	143	22	645	79.4	664	33
41	UGC08146	PG1259+593	114	50	670	82.4	646	13
41	UGC08146	PG1259+593	114	50	670	82.4	683	16
42	UGC09760	SDSSJ151237.15+012846.0	123	90	2094	-46	2029	50

Note. —

reasonable values for the position angle can vary by at least  $\sim 5^\circ$ , and this becomes even more uncertain for lower inclination galaxies. Because of this inherent uncertainty in every position angle measurement, we have automatically designated every system with an azimuth of  $85^\circ$  or higher as “uncertain.” We do not include these when calculating co-rotation fractions or otherwise separating systems into co- and anti-rotating subsets.

For the remaining sample we designate each system as co-rotating or anti-rotating firstly based on the on-sky apparent velocity orientation. For example, an absorber with positive  $\Delta v$  which is detected on the receding side of a galaxy is labeled “co-rotating” (recall  $\Delta v = v_{\text{absorber}} - v_{\text{galaxy}}$ , hence a positive value corresponds to absorption with velocity higher than the galaxy systemic). Next, we compare  $\Delta v$  of each absorber to our cylindrical and NFW profile fit model predictions. For example, an absorber with  $\Delta v = 50$  and model ranges of (cylindrical = [0, 35], NFW = [10, 55]) would be labeled “anti-rotating” for the cylindrical and “co-rotating” for the NFW models, because  $\Delta v = 50 \text{ km s}^{-1}$  is inside the NFW range and outside the cylindrical range. In order to broadly account for both velocity uncertainties and absorber linewidth, we allow for an  $\pm 10 \text{ km s}^{-1}$  error with respect to these model ranges (i.e., if  $\Delta v$  is within  $10 \text{ km s}^{-1}$  of the edge of either model velocity range we count it as “co-rotating”). This is a conservative underestimate of the true errors in the sense that larger errors would allow for *more* absorbers to be labeled “co-rotating.” The majority of our “co-rotating” sample fall well within the model ranges, so few would be thrown into uncertainty with a larger error, whereas many “anti-rotators” are close to the allowed ranges.

#### 4.4.1 Co-rotation Fraction

Here we consider in aggregate our sample of Ly $\alpha$  absorbers, and the fraction consistent with co-rotation under various cuts and constraints.

To start we consider the fraction of absorbers which appear to be rotating in the same sense as the nearby galaxy. With no cuts of any kind, we find 54% of absorbers to be co-rotating with the nearby galaxy based on apparent velocity only. Figure 4.3 presents an map of the locations of each absorber relative to it's assumed host galaxy. In this figure we have rotated every system such that the galaxy major axes are horizontal with the approaching side on the left. Blue-diamonds indicate the absorber has the appropriate velocity sign for co-rotation, red-crosses indicate an anti-alignment, grey circles indicate uncertain systems due to their high azimuth angles, and open grey circles indicate non-detections. We have also scaled the size of each marker according to it's relative EW, and

Table 4.4. Summary of Results

Sub-sample	Co-rotating	Anti-rotating	Uncertain	Co-rotating	Anti-rotating
				$\rho \leq 1$	$\rho \leq 1$
Apparent Vel.	30	26	9	13	9
Cyl. Model	22	34	9	9	13
NFW Model	24	32	9	9	13
<hr/>					
NFW w/ Constraint: $\Delta v \leq v_{\text{rot}}$	24	14	5	9	6
NFW w/ Constraint: Nearest $\rho \geq 20$ kpc	13	13	6	3	3
NFW w/ Both Constraints	13	8	2	3	1
<hr/>					
NFW w/ $\Delta v$ Constraint: $[0 \leq L^* \leq 0.6]$	12	1	0	5	1
NFW w/ $\Delta v$ Constraint: $[L^* > 0.6]$	12	13	5	4	5

Note. — Comments.

annotated each with a number corresponding to the appropriate system number given in Column (1) of Table 4.3. Figure 4.4 shows the same map zoomed in to a radius of  $1R_{\text{vir}}$ .

A cursory look at Figures 4.3 and 4.4 reveals several interesting results. First, the highest EW absorbers are all found within  $1R_{\text{vir}}$ . This is not surprising, given the results by numerous groups claiming an impact parameter - equivalent width anti-correlation (see e.g., French & Wakker 2017, and references therein). Second, many of our absorbers, and many co-rotating ones, lie in the  $1 - 2R_{\text{vir}}$  region. Previously, most groups have concentrated on studying the sub- $1R_{\text{vir}}$  regime, but doing so clearly does not reveal the whole physical picture. Third, most (52%) of galaxy-QSO systems reveal multiple distinct velocity components, and they tend to be oriented such that one component is co- and one anti-rotating with the nearby galaxy.

However, a more in-depth look at the underlying data reveals that many of these absorbers have  $\Delta v$  much larger than the inclination-corrected galaxy rotation velocity ( $v_{\text{rot}}$ ). In other words, the velocity of the absorber relative to galaxy systemic is much greater than the rotation velocity of the galaxy disk. This results in a much smaller fraction of co-rotating absorbers when compared to our cylindrical and NFW profile models (39% and 43%, respectively), which will never output a velocity higher than  $v_{\text{rot}}$ . In undertaking this study we necessarily must begin by assuming that absorption within some velocity limit and impact parameter from a galaxy is likely associated with that galaxy. To start with we set these limits at  $\Delta v_{\text{max}} = 400 \text{ km s}^{-1}$  and  $\rho_{\text{max}} = 3R_{\text{vir}}$ .

Let us now instead consider only absorbers with  $\Delta v \leq v_{\text{rot}} \pm 10 \text{ km s}^{-1}$ , or absorbers with velocities differences no greater than the maximal galaxy rotation velocity (including a  $\pm 10 \text{ km s}^{-1}$  buffer to account for velocity and linewidth uncertainties; in other words the we are only considering absorbers where  $|v_{\text{Ly}\alpha} - v_{\text{sys}}| \leq v_{\text{rot}} \pm 10 \text{ km s}^{-1}$ , which are those absorbers within the velocity range of  $\pm$  rotation – this constraint removes 22 from

our original sample of 65 absorbers). This constraint thus focuses only on absorbers whose velocity falls within the range of possible rotation-related velocities. While this could be interpreted as a bias in the sample, we are really only setting the  $\Delta v$  velocity separation limit on a case-by case basis instead of globally given the additional information available to us. We could just as easily have started this study by looking for only absorbers within  $\Delta v = 150 \text{ km s}^{-1}$  of a galaxy instead of  $\Delta v = 400 \text{ km s}^{-1}$ , which would have a similar overall effect. This criteria instead narrows the focus to only those absorbers kinematically close enough to a galaxy to test for a co-rotation fraction with minimal contamination from Ly $\alpha$  forest lines.

With this rotation-based velocity constraint in place the co-rotating fractions for our cylindrical and NFW models increase to 58% and 63%, while the apparent co-rotation fraction decreases slightly to 50%. Consistently, we find our cylindrical model to predict an  $\sim 8 - 10\%$  higher co-rotation fraction than the straight apparent velocity analysis yields, and our NFW model tends to predict an additional  $\sim 5\%$  increase. This is a not wholly unexpected, and yet refreshing result; simulations have predicted that galaxies are strongly linked to their surroundings and share angular momentum, which should result in a higher than 50% halo-gas co-rotation fraction. However, the simple apparent on-sky velocity method ignores the complexities of sampling a 3-dimensional structure with a 1-dimensional QSO sightline. It appears then that the NFW model, the most physically motivated of the three, systematically recovers a higher fraction of this co-rotating gas. For brevity's sake we will concentrate only on the NFW model results from here onwards. Figure 4.5 shows another absorber location map, this time colored according to our NFW model results.

One additional constraining step we consider is to only include galaxies which have no neighbors within at least 20 kpc. The disruptions caused by near neighbors to both

galaxy H I disks and halos has been well established observationally, so a 20 kpc minimum separation should at least remove the systems most likely to be disrupted. This constraint alone leads to a co-rotating fraction of 50%. Combining both constraints results in a 62% co-rotating fraction.

#### 4.4.2 Co-rotation as a function of $L^*$

Next, we consider the effect of galaxy luminosity. We separate our sample around  $0.6L^*$ , while keeping our  $\Delta v \leq v_{\text{rot}} \pm 10 \text{ km s}^{-1}$  constraint and relaxing the 20 kpc nearest-neighbor criteria in order to maximize the sample size. This results in 13 absorbers near  $L \leq 0.6L^*$  galaxies and 30 around more luminous galaxies. The co-rotating fraction around luminous galaxies is then 48%, compared to 92% around  $L \leq 0.6L^*$  galaxies. Figure 4.7 shows an absorber map for these  $L \leq 0.6L^*$  galaxies only. In fact, the co-rotating absorber fraction smoothly decreases as a function of  $L^*$ , as shown in Figure 4.6(a). In this figure we have binned galaxy-absorber systems into the following 4 ranges:  $[0 - 0.5]$ ,  $(0.5 - 1.0]$ ,  $(1.0 - 1.7]$ , and  $(1.7 - \infty)$ . This uneven bin spacing was chosen to produce as evenly occupied bins as possible, and does not affect the overall trend. Unfortunately there are a large number of systems between  $1.7 - 1.8 L^*$ , so no splitting exists to produce perfectly even bins. The co-rotation fraction is labeled explicitly underneath each data point for clarity.

In Figure 4.6(b) we consider the co-rotation fraction as a function of the cumulative  $L^*$  distribution (i.e., every consecutive  $L^*$  bin includes all previous bins' data as well). Here, bins are evenly distributed in  $0.25L^*$  increments with the final bin containing all systems. Thus, nearly 90% of absorbers near  $L^*$  or fainter galaxies are co-rotating based on our NFW model results, but this fraction decreases to  $\sim 80\%$  for  $1.5L^*$  or fainter galaxies, and to 63% for all galaxies. As seen in Figure 4.6(b), this trend is also model independent; it

appears nearly identically but offset downward in both the cylindrical model (red-rhombus) and apparent velocity only (grey-square) samples.

Given recent simulation results suggesting that co-rotating accretion gas is predominately cold-mode for low-mass galaxies in the local Universe, this may be a signature of this co-rotating, cold-mode accreting gas. Additionally, Lutz et al. (2018) find that galaxies with high H<sub>I</sub> mass compared to their stellar mass have higher halo angular momentum, which may be impeding their ability to efficiently form stars. While we do not have independent measures of H<sub>I</sub> and stellar mass for our galaxies, it may not be unreasonable to think that these high angular momentum galaxies reside toward the lower luminosity end of our sample.

#### 4.4.3 Doppler *b*-parameters

Finally, we consider the Doppler *b*-parameters of our absorber sample. Figure 4.8(a) shows the distribution of *b*-parameters for all velocity-constrained Ly $\alpha$  absorbers ( $\Delta v \leq v_{\text{rot}} \pm 10 \text{ km s}^{-1}$ ). In the top panel of Figure 4.8(a) we separate them into co-rotating and anti-rotating subsets, in the middle panel we do the same but only for  $\rho \leq 1R_{\text{vir}}$ , and on the bottom we separate based on absorbers near  $L^* \leq 0.6$  and  $L^* > 0.6$  galaxies. Interestingly, we find that *lower* *b*-parameter absorbers tend to be both anti-rotating and found near  $L^* > 0.6$  galaxies. As we've previously discussed however, the picture described by the simulations of Stewart et al. (2011b) and others describes a scenario where co-rotating gas is predominately the product of cold-mode accretion. Hotter, outflowing gas would likely carry angular momentum from the disk with it, but this would be quickly lost as the outflows expand into the halo and result in negligible observable rotation.

In Figure 4.8(b) we show how the *b*-parameters vary as a function of  $\Delta v$  for co-rotating versus anti-rotating absorbers. We would expect the co-rotating sample to occupy

a narrower  $\Delta v$  space based on their definition ( $\Delta v$  fitting within the velocity bounds given by our NFW model), but the elevated  $b$ -parameters for these compared to the relatively flat distribution for anti-rotators is intriguing. Aside from a single Ly $\alpha$  line toward SDSSJ104335.90+115129.0 and NGC3351, all the anti-rotators have  $b \lesssim 50 \text{ km s}^{-1}$ . As these are higher than expected for purely thermal motions within a single Ly $\alpha$  structure, we may be observing either a number of clouds that are close in velocity space or a filament with a range of turbulent, internal velocities. In this scenario these high  $b$ -parameters would be consistent with filamentary inflows versus around higher  $L^*$  galaxies where virial shocks are perhaps breaking larger structures into smaller, more isolated cloudlets and producing lower  $b$ -parameter absorption.

## 4.5 Summary

We have presented complimentary COS Ly $\alpha$  absorption-line and nearby galaxy rotation curve analysis for a sample of 42 galaxy-QSO pairs, resulting in the largest yet sample of its kind. Our main conclusions are the following:

1. The fraction of Ly $\alpha$  absorbers appearing to co-rotate with the nearby galaxy smoothly declines as a function galaxy luminosity ( $L^*$ ). Our overall co-rotation fraction is consistent with the simulation results of Stewart et al. (2011b, 2013), and effect of galaxy luminosity on halo gas co-rotation is consistent with predicted cold-mode filamentary accretion schemes.
2. Based on our NFW halo model, 92% of absorbers co-rotate around  $\leq 0.6L^*$  galaxies, which falls to 77% around  $\leq 1.5 L^*$  galaxies, and down to 63% around all galaxies at  $z \sim 0$ .
3. Two thirds of all Ly $\alpha$  absorbers are found with velocity separations less than

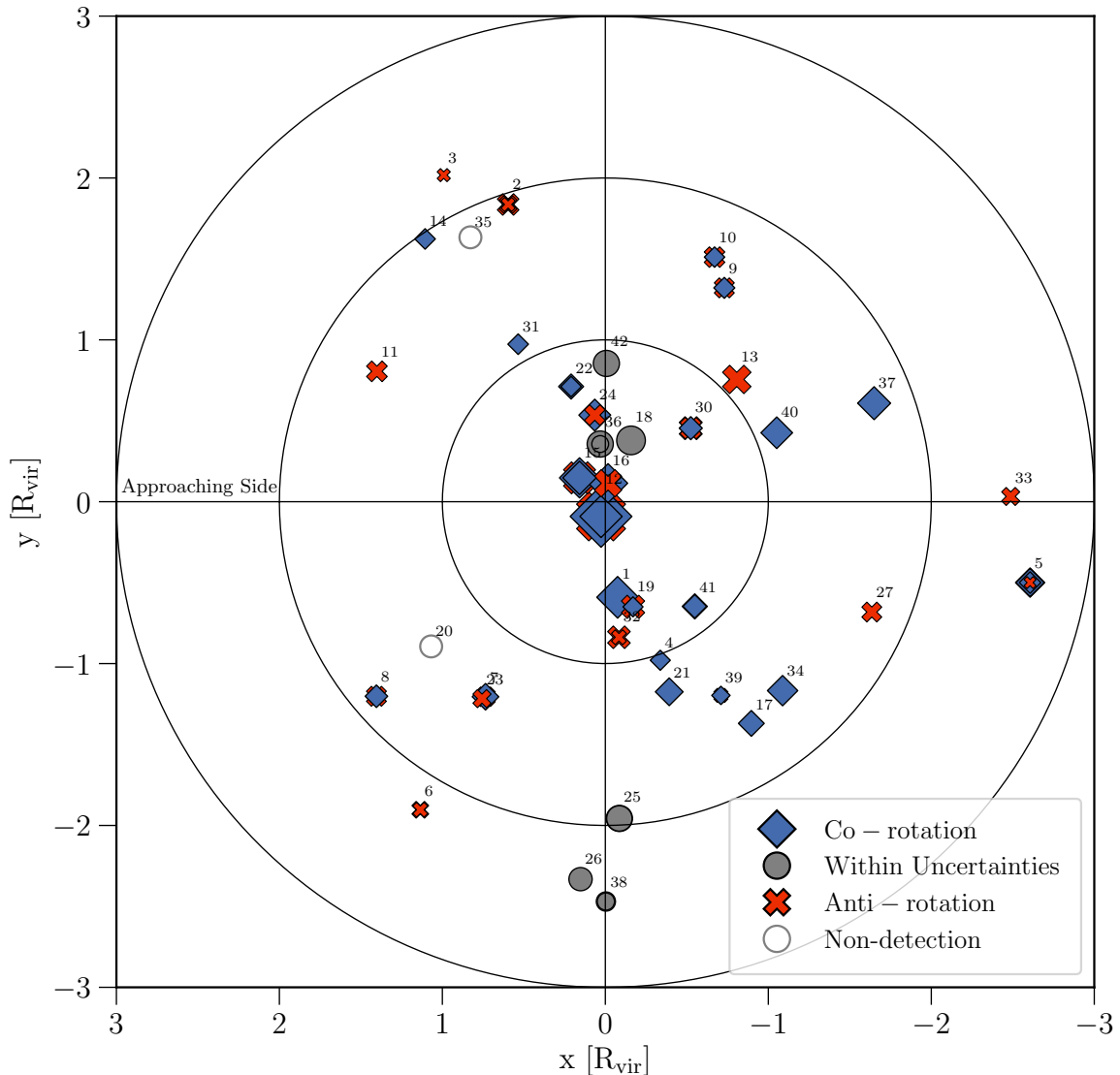
or equal to the nearby galaxy rotation velocity ( $\Delta v \leq |v_{\text{rot}}| \pm 10 \text{ km s}^{-1}$ ). This includes systems with multiple galaxies and undoubtedly complex velocity fields. Restricting this study to only isolated galaxy-QSO systems would likely result in an even higher fraction.

4. A simple cylindrical halo model with rotation velocities smoothly declining based on an NFW rotation curve fit results in the highest co-rotation fraction for Ly $\alpha$  absorbers (63%).

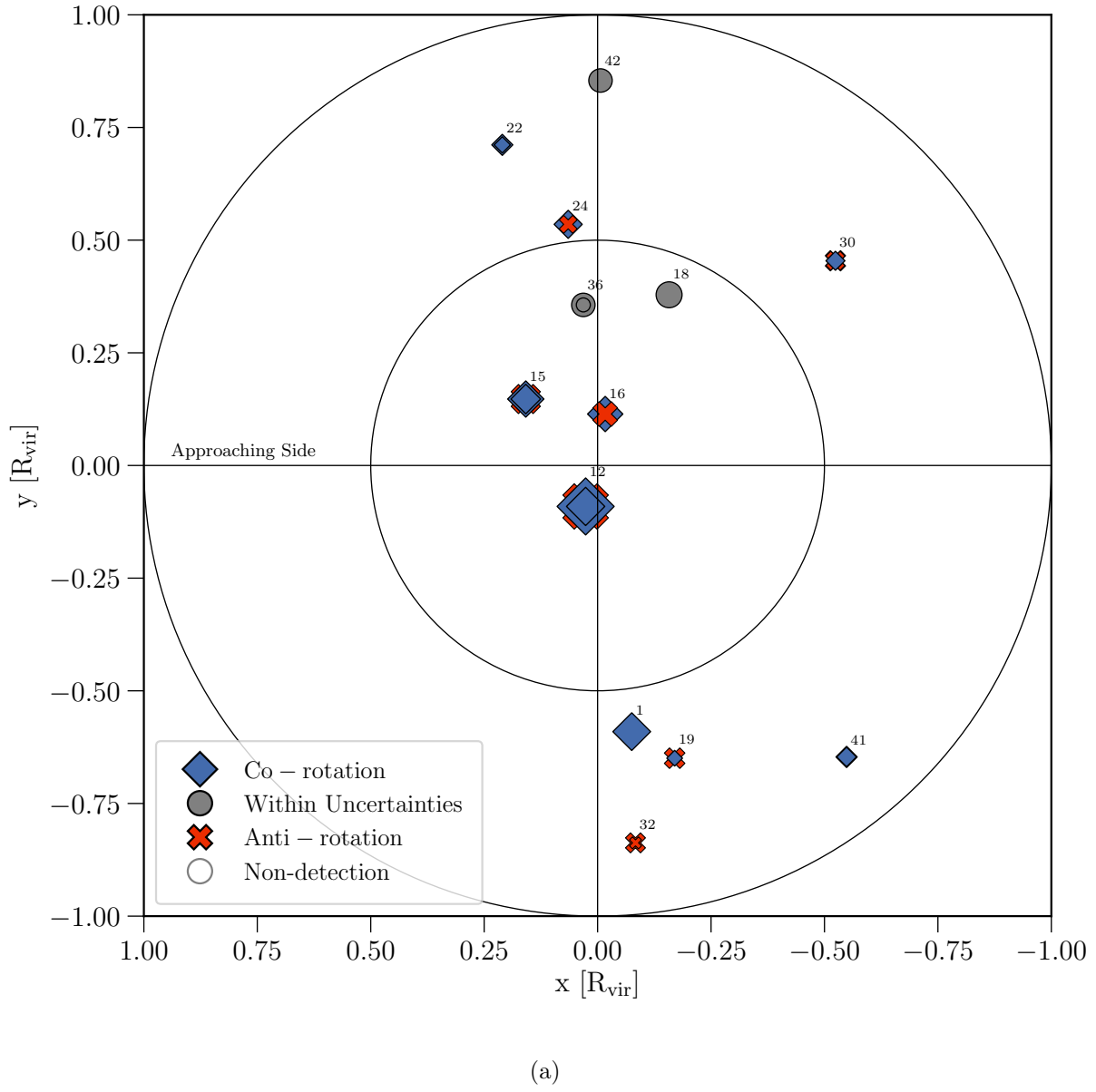
5. Co-rotating absorbers (when chosen from the sample restricted to  $\Delta v \leq |v_{\text{rot}}| \pm 10 \text{ km s}^{-1}$ ) occupy a wide range in Doppler  $b$ -parameter, while anti-rotators have mostly  $b \leq 50 \text{ km s}^{-1}$ . A remarkably similar split is found for absorbers near  $L \leq 0.6L^*$  vs  $L > 0.6L^*$  galaxies. This could add further evidence for our proposed cold-mode accretion explanation if these enhanced  $b$ -parameters are caused by the blending of multiple absorption components close in velocity space within a filament.

D. M. F. thanks Claire Murray for useful insights, particularly related to our halo model, and Julie Davis for invaluable SALT data reduction pointers. This research has made use of the NASA/IPAC Extragalactic Database (NED) which is operated by the Jet Propulsion Laboratory, California Institute of Technology, under contract with the National Aeronautics and Space Administration. Based on observations with the NASA/ESA *Hubble Space Telescope*, obtained at the Space Telescope Science Institute (STScI), which is operated by the Association of Universities for Research in Astronomy, Inc., under NASA contract NAS 5-26555. Spectra were retrieved from the Barbara A. Mikulski Archive for Space Telescopes (MAST) at STScI. Some of the observations reported in this paper were obtained with the Southern African Large Telescope (SALT) under program 2016-1-SCI-062 (PI: Wakker). Over the course of this study, D.M.F. and B.P.W. were supported by

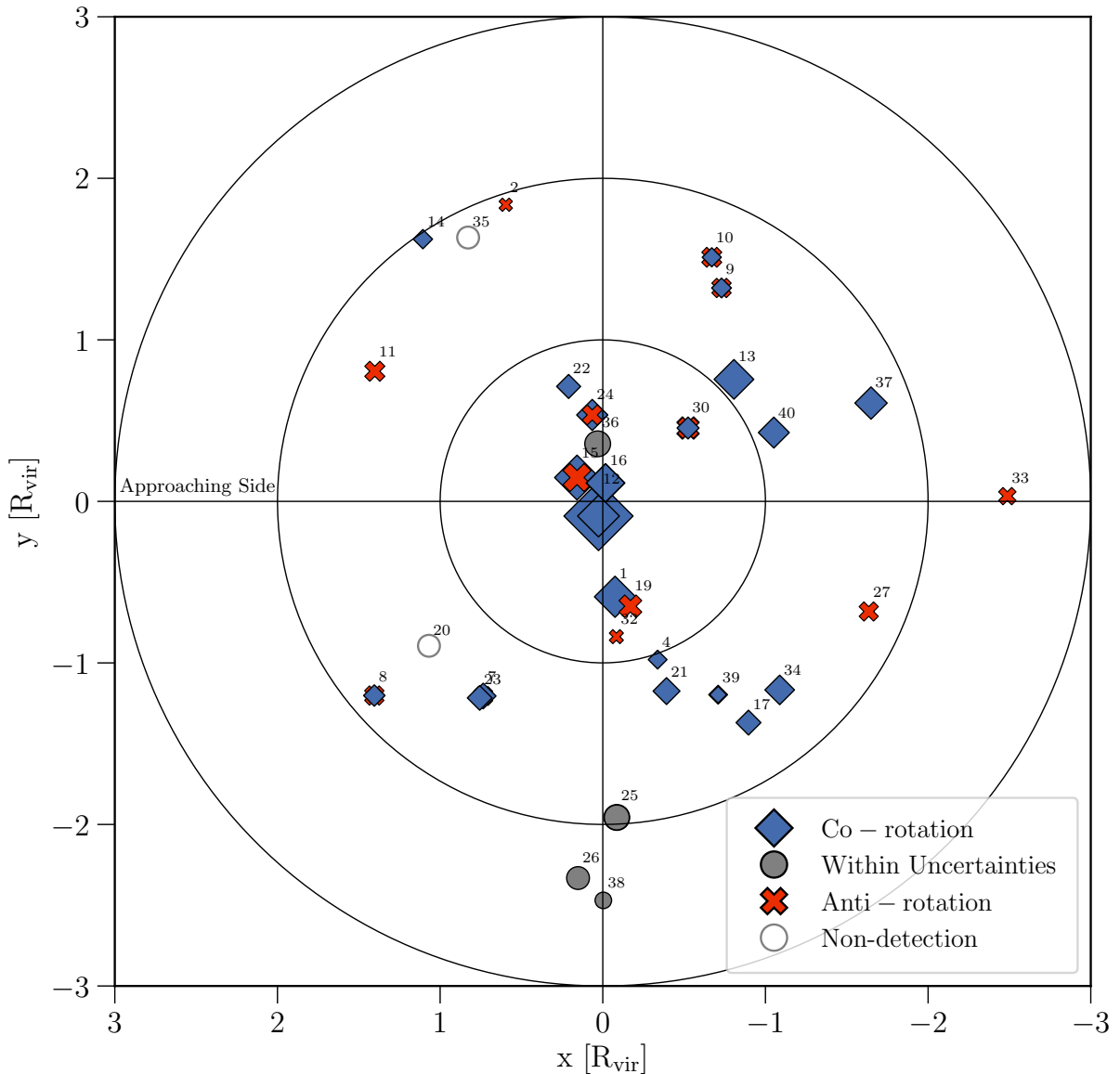
grant AST-118913 from the National Science Foundation and GO-14240, GO-14268, and GO-14588 from the Space Telescope Science Institute.



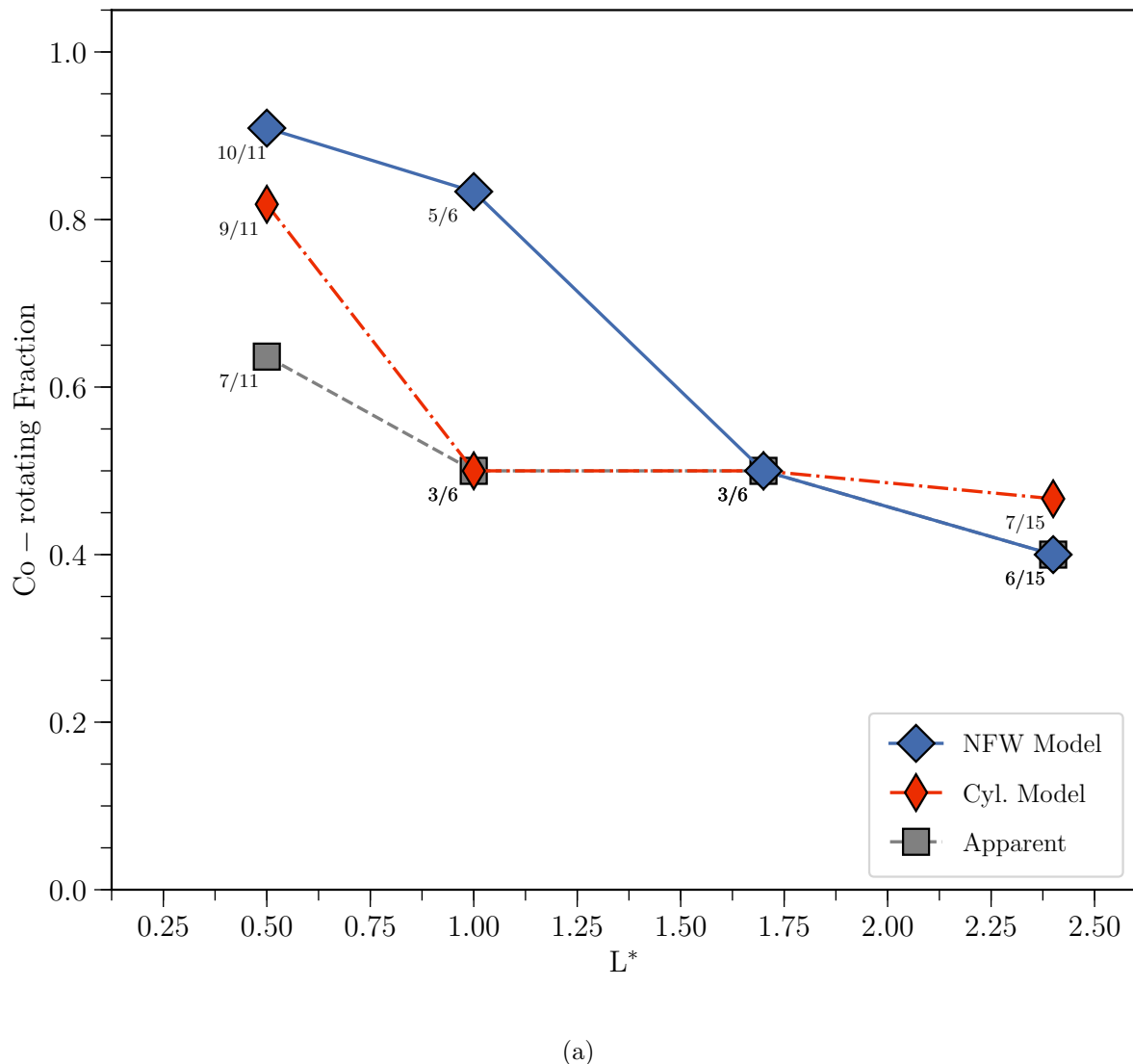
**Figure 4.3 :** A map of the locations of each absorber normalized with respect to the galaxy virial radius, with *no* additional constraints. The color and style of each point indicates the line-of-sight velocity compared to that of the rotation of the nearby galaxy. Blue diamonds indicate co-rotation, red crosses indicate anti-rotation, and grey circles indicate cases where either is possible due to a combination of orientation and velocity uncertainties. The size of each point is scaled to reflect the EW of the absorber. Concentric rings indicate distances of 1, 2, and 3  $R_{\text{vir}}$ . All galaxies are rotated to PA = 90 or 270, such that their major axis' are horizontal and their approaching side is on the left as indicated. The number identifiers correspond to the system number given in column (1) of Table 4.3.



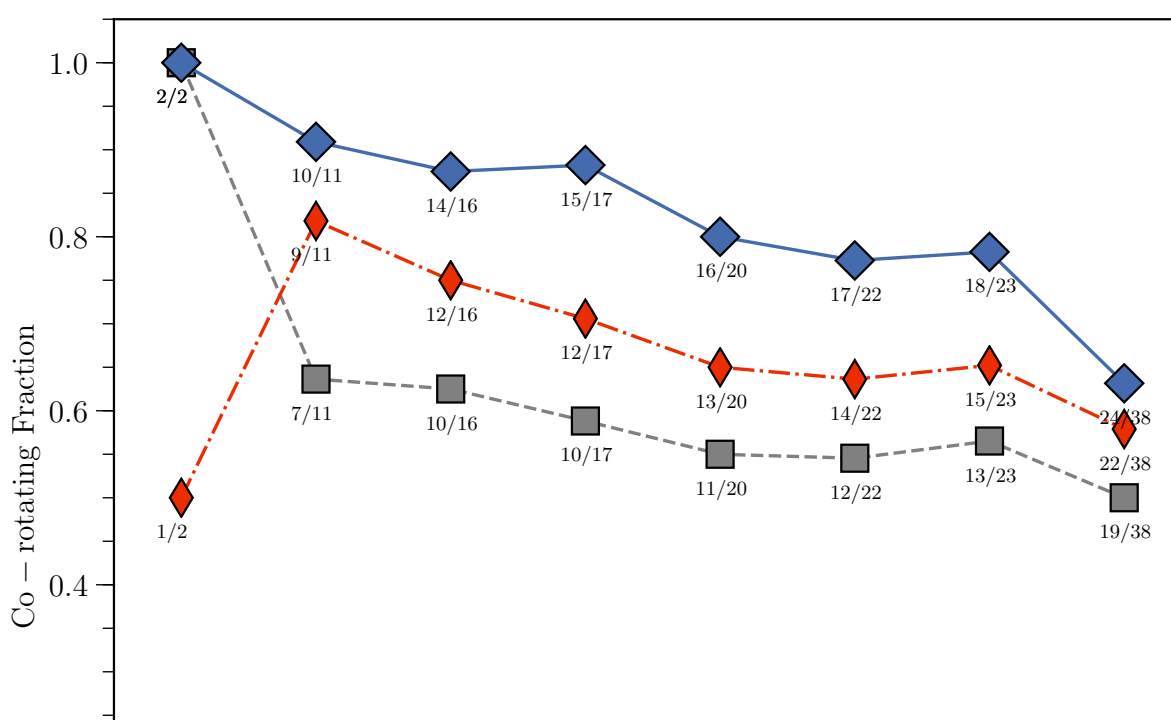
**Figure 4.4 :** A map of the locations of each absorber normalized with respect to the galaxy virial radius. A zoom in showing only those systems within  $1R_{\text{vir}}$  (exactly the same as Figure 4.3 within  $1R_{\text{vir}}$ ). The color and style of each point indicates the line-of-sight velocity compared to that of the rotation of the nearby galaxy. Blue diamonds indicate co-rotation, red crosses indicate anti-rotation, and grey circles indicate cases where either is possible due to a combination of orientation and velocity uncertainties. The size of each point is scaled to reflect the EW of the absorber. All galaxies are rotated to PA = 90 or 270, such that their major axis' are horizontal and their approaching side is on the left as indicated. The number identifiers correspond to the system number given in column (1) of Table 4.3.



**Figure 4.5 :** A map of the locations of each absorber normalized with respect to the galaxy virial radius. The color and style of each point indicates the NFW rotation model results for each absorber with a  $v_{\text{Ly}\alpha} \leq v_{\text{rot}}$  constraint imposed. Concentric rings indicate distances of 1, 2, and 3  $R_{\text{vir}}$ . Blue diamonds indicate co-rotation, red crosses indicate anti-rotation, and grey circles indicate cases where either is possible due to a combination of orientation and velocity uncertainties. The size of each point is scaled to reflect the EW of the absorber. All galaxies are rotated to PA = 90 or 270, such that their major axis' are horizontal and their approaching side is on the left as indicated. The number identifiers correspond to the system number given in column (1) of Table 4.3.



(a)



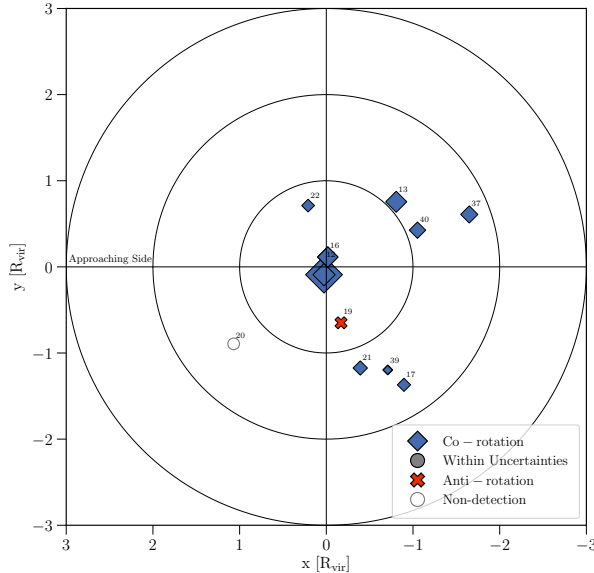
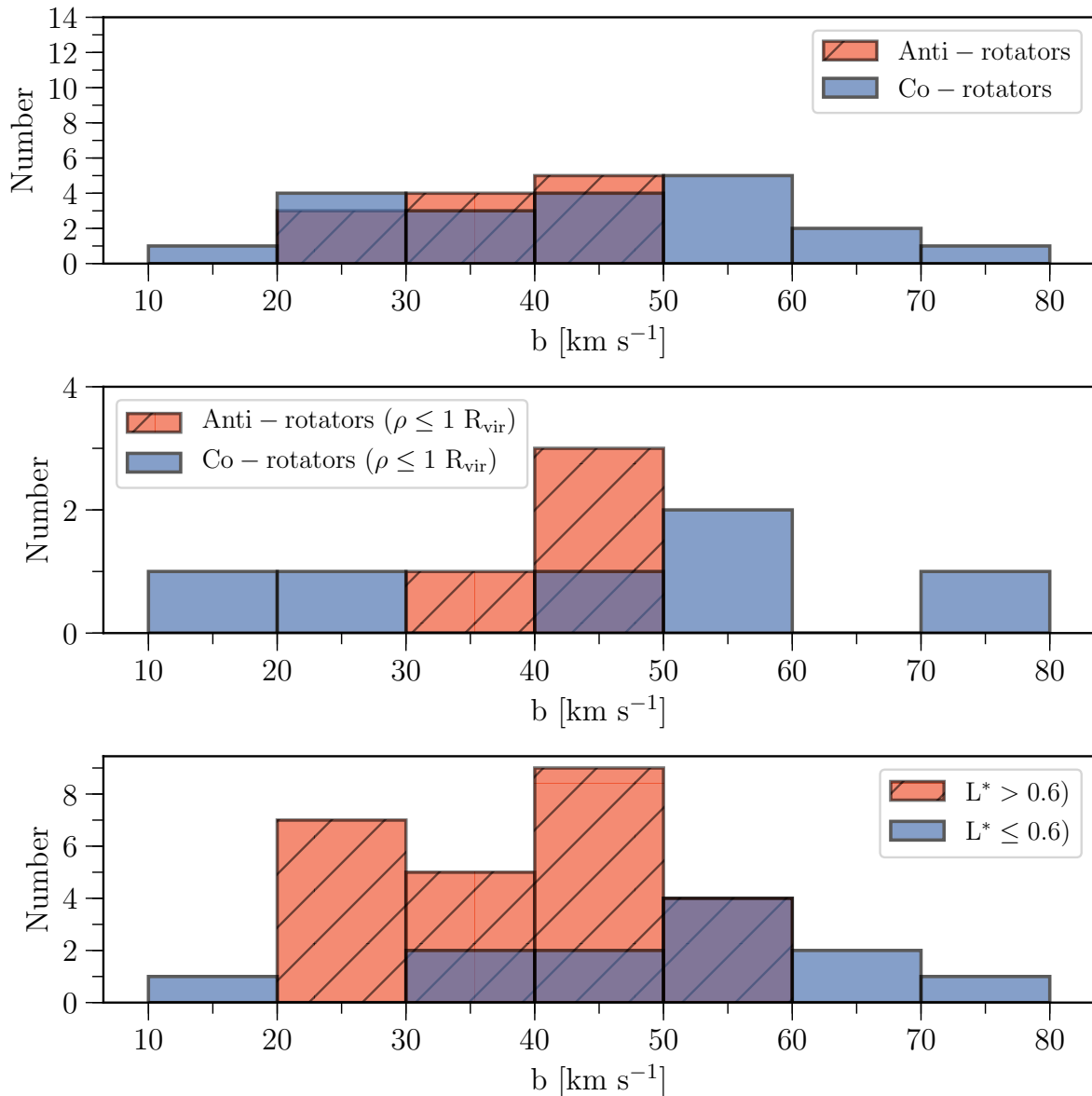
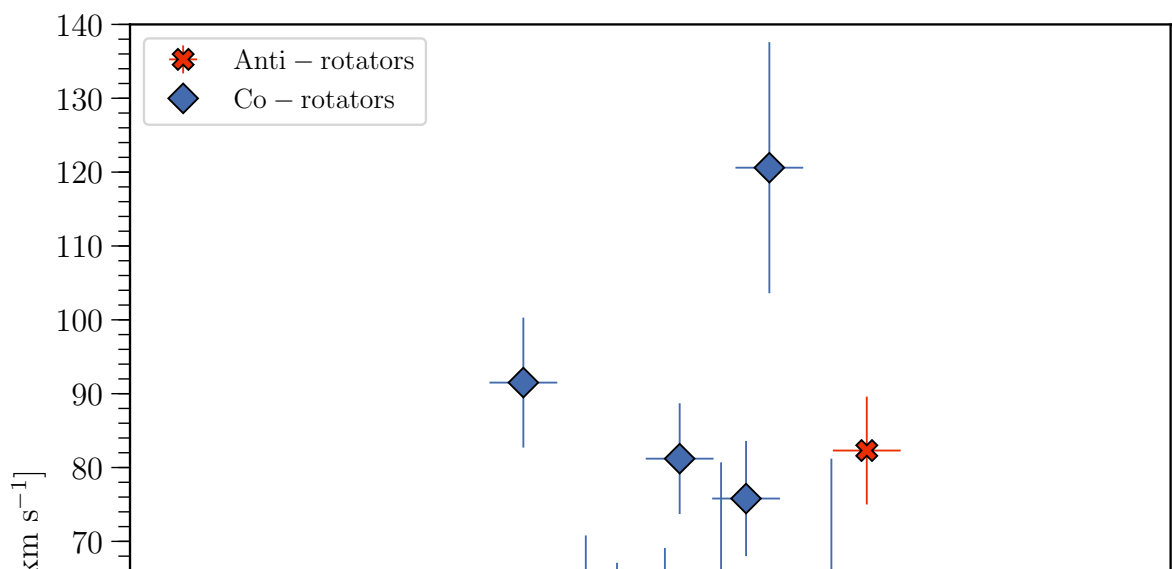


**Figure 4.7 :** A map of the locations of each absorber normalized with respect to the galaxy virial radius. The color and style of each point indicates the NFW rotation model results for each absorber with  $\Delta v \leq v_{rot}$  and  $L^* \leq 0.6$  constraints imposed. Blue diamonds indicate co-rotation, red crosses indicate anti-rotation, and grey circles indicate cases where either is possible due to a combination of orientation and velocity uncertainties. The size of each point is scaled to reflect the EW of the absorber. Concentric rings indicate distances of 1, 2, and 3  $R_{vir}$ . All galaxies are rotated to PA = 90 or 270, such that their major axis' are horizontal and their approaching side is on the left as indicated. The number identifiers correspond to the system number given in column (1) of Table 4.3.



(a)



## References

- Abazajian, K., Adelman-McCarthy, J. K., Agüeros, M. A., et al. 2005, AJ, 129, 1755
- Bertschinger, E. 1985, ApJS, 58, 39
- Birnboim, Y., & Dekel, A. 2003, MNRAS, 345, 349
- Bowen, D. V., Chelouche, D., Jenkins, E. B., et al. 2016, ApJ, 826, 50
- Brook, C. B., Governato, F., Roškar, R., et al. 2011, MNRAS, 415, 1051
- Brooks, A. M., Governato, F., Quinn, T., Brook, C. B., & Wadsley, J. 2009, ApJ, 694, 396
- Buckley, D. A. H., Swart, G. P., & Meiring, J. G. 2006, in Proc. SPIE, Vol. 6267, Society of Photo-Optical Instrumentation Engineers (SPIE) Conference Series, 62670Z
- Burgh, E. B., Nordsieck, K. H., Kobulnicky, H. A., et al. 2003, in Proc. SPIE, Vol. 4841, Instrument Design and Performance for Optical/Infrared Ground-based Telescopes, ed. M. Iye & A. F. M. Moorwood, 1463–1471
- Carilli, C. L., van Gorkom, J. H., & Stocke, J. T. 1989, Nature, 338, 134
- Charlton, J. C., & Churchill, C. W. 1998, ApJ, 499, 181
- Chen, D. N., Jing, Y. P., & Yoshikawa, K. 2003, ApJ, 597, 35
- Corwin, Jr., H. G., Buta, R. J., & de Vaucouleurs, G. 1994, AJ, 108, 2128
- Côté, S., Wyse, R. F. G., Carignan, C., Freeman, K. C., & Broadhurst, T. 2005, ApJ, 618, 178
- Crawford, S. M., Still, M., Schellart, P., et al. 2010, in Proc. SPIE, Vol. 7737, Observatory Operations: Strategies, Processes, and Systems III, 773725
- Danovich, M., Dekel, A., Hahn, O., & Teyssier, R. 2012, MNRAS, 422, 1732
- de Blok, W. J. G., Walter, F., Brinks, E., et al. 2008, AJ, 136, 2648
- Dekel, A., & Birnboim, Y. 2006, MNRAS, 368, 2
- Dekel, A., Birnboim, Y., Engel, G., et al. 2009, Nature, 457, 451
- di Nella, H., Paturel, G., Walsh, A. J., et al. 1996, A&AS, 118, 311
- Diamond-Stanic, A. M., Coil, A. L., Moustakas, J., et al. 2016, ApJ, 824, 24
- Dicaiare, I., Carignan, C., Amram, P., et al. 2008, MNRAS, 385, 553
- Falco, E. E., Kurtz, M. J., Geller, M. J., et al. 1999, PASP, 111, 438
- Fillmore, J. A., & Goldreich, P. 1984, ApJ, 281, 1

- French, D. M., & Wakker, B. P. 2017, ApJ, 837, 138
- Giovanelli, R., Avera, E., & Karachentsev, I. D. 1997, AJ, 114, 122
- Green, J. C., Froning, C. S., Osterman, S., et al. 2012, ApJ, 744, 60
- Grogin, N. A., Geller, M. J., & Huchra, J. P. 1998, ApJS, 119, 277
- Ho, S. H., Martin, C. L., Kacprzak, G. G., & Churchill, C. W. 2017, ApJ, 835, 267
- Jones, D. H., Read, M. A., Saunders, W., et al. 2009, MNRAS, 399, 683
- Kacprzak, G. G., Churchill, C. W., Barton, E. J., & Cooke, J. 2011, ApJ, 733, 105
- Kacprzak, G. G., Churchill, C. W., Ceverino, D., et al. 2010, ApJ, 711, 533
- Keeney, B. A., Momjian, E., Stocke, J. T., Carilli, C. L., & Tumlinson, J. 2005, ApJ, 622, 267
- Kereš, D., Katz, N., Weinberg, D. H., & Davé, R. 2005, MNRAS, 363, 2
- Kimm, T., Slyz, A., Devriendt, J., & Pichon, C. 2011, MNRAS, 413, L51
- Knapen, J. H. 1997, MNRAS, 286, 403
- Kobulnicky, H. A., Nordsieck, K. H., Burgh, E. B., et al. 2003, in Proc. SPIE, Vol. 4841, Instrument Design and Performance for Optical/Infrared Ground-based Telescopes, ed. M. Iye & A. F. M. Moorwood, 1634–1644
- Koribalski, B. S., Staveley-Smith, L., Kilborn, V. A., et al. 2004, AJ, 128, 16
- Krogager, J.-K. 2018, ArXiv e-prints, arXiv:1803.01187
- Lu, N. Y., Hoffman, G. L., Groff, T., Roos, T., & Lamphier, C. 1993, ApJS, 88, 383
- Lutz, K. A., Kilborn, V. A., Koribalski, B. S., et al. 2018, MNRAS, 476, 3744
- Mathewson, D. S., & Ford, V. L. 1996, ApJS, 107, 97
- Narayanan, A., Wakker, B. P., Savage, B. D., et al. 2010, ApJ, 721, 960
- Navarro, J. F., Frenk, C. S., & White, S. D. M. 1996, ApJ, 462, 563
- . 1997, ApJ, 490, 493
- Ocvirk, P., Pichon, C., & Teyssier, R. 2008, MNRAS, 390, 1326
- O'Donoghue, D., Buckley, D. A. H., Balona, L. A., et al. 2006, MNRAS, 372, 151
- Pichon, C., Pogosyan, D., Kimm, T., et al. 2011, MNRAS, 418, 2493
- Powell, L. C., Slyz, A., & Devriendt, J. 2011, MNRAS, 414, 3671

- Rhee, M.-H., & van Albada, T. S. 1996, A&AS, 115, 407
- Rubin, V. C., Thonnard, N. T., & Ford, Jr., W. K. 1982, AJ, 87, 477
- Sharma, S., & Steinmetz, M. 2005, ApJ, 628, 21
- Shen, S., Madau, P., Guedes, J., et al. 2013, ApJ, 765, 89
- Sofue, Y. 1996, ApJ, 458, 120
- Steidel, C. C., Kollmeier, J. A., Shapley, A. E., et al. 2002, ApJ, 570, 526
- Stewart, K. R., Brooks, A. M., Bullock, J. S., et al. 2013, ApJ, 769, 74
- Stewart, K. R., Kaufmann, T., Bullock, J. S., et al. 2011a, ApJL, 735, L1
- . 2011b, ApJ, 738, 39
- Stewart, K. R., Maller, A. H., Oñorbe, J., et al. 2017, ApJ, 843, 47
- Stocke, J. T., Keeney, B. A., & Danforth, C. W. 2010, PASA, 27, 256
- Swaters, R. A., Sancisi, R., van Albada, T. S., & van der Hulst, J. M. 2009, A&A, 493, 871
- van de Voort, F., Schaye, J., Booth, C. M., Haas, M. R., & Dalla Vecchia, C. 2011, MNRAS, 414, 2458
- Verheijen, M. A. W., & Sancisi, R. 2001, A&A, 370, 765
- Wakker, B. P., Hernandez, A. K., French, D. M., et al. 2015, ApJ, 814, 40
- Wakker, B. P., & Savage, B. D. 2009, ApJS, 182, 378
- Yim, K., Wong, T., Xue, R., et al. 2014, AJ, 148, 127

## A SALT Galaxies

In this section we summarize each galaxy-QSO system observed by SALT. We calculate impact parameters to QSOs and galaxy-absorber velocity separations ( $\Delta v = v_{\text{Ly}\alpha} - v_{\text{sys}}$ ) based on our measured  $v_{\text{sys}}$  values. Both measured and previously published values for  $v_{\text{sys}}$  are given in Table 4.1 for reference. We provide rotation curves and finder chart images for the sub-sample of galaxies with newly observed SALT data.

### A.1 CGCG039-137

CGCG039-137 is an isolated Scd type galaxy with a measured systemic velocity  $v_{\text{sys}} = 6918 \pm 24 \text{ km s}^{-1}$  and inclination of  $i = 63^\circ$ . The QSO RX\_J1121.2+0326 is located nearby at an impact parameter of 99 kpc and azimuth angle of  $71^\circ$  on the receding side. The data for RX\_J1121.2+0326 has low signal-to-noise ( $\sim 4.2$ ), but we are able to detect Ly $\alpha$  at  $6975 \text{ km s}^{-1}$ , which, at  $\Delta v = 57 \text{ km s}^{-1}$ , lies well within the range of projected velocities consistent with co-rotation (cylindrical model = [-36, 137], NFW = [-37, 164]  $\text{km s}^{-1}$ ).

### A.2 ESO343-G014

ESO343-G014 is an edge-on spiral galaxy with a measured systemic velocity  $v_{\text{sys}} = 9139 \pm 32 \text{ km s}^{-1}$ . It has a smaller neighboring galaxy, 2MASXJ21372816-3824412, located north of its major axis at a projected distance of 216 kpc and velocity of  $9129 \text{ km s}^{-1}$ . The nearest sightline is towards RBS1768 at  $\rho = 466 \text{ kpc}$  and  $74^\circ$  azimuth angle on the approaching side. We detect 3 blended Ly $\alpha$  absorption components toward RBS1768 at  $v_{\text{Ly}\alpha} = 9308, 9360, 9434 \text{ km s}^{-1}$  ( $\Delta v = 169, 221, 295 \text{ km s}^{-1}$ ). This system is highly blended with galactic S II, and therefore their widths are not reliable. All of these are anti-aligned

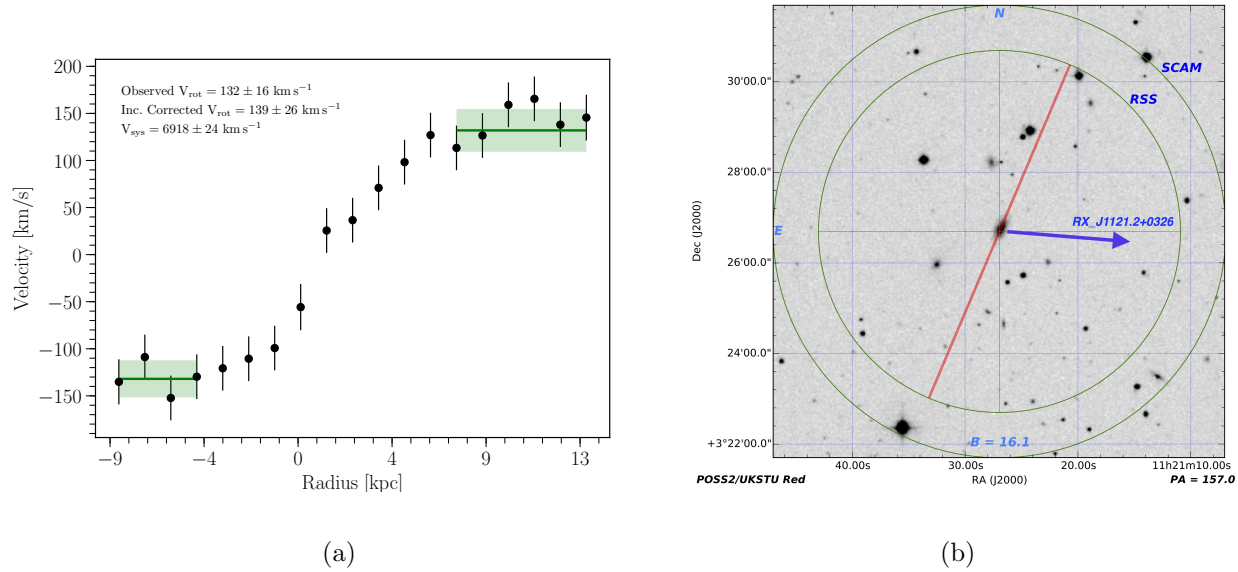


**Figure 4.9** : a) Rotation curve of CGCG039-137. The solid green line indicates the weighted mean velocity over the corresponding x-axis region, and the shaded green indicates the  $1\sigma$  error in the mean. b) SALT finder chart for CGCG039-137 showing the position of the slit in red.

with the rotation of ESO343-G014 relative to the models (cylindrical = [-203, 10], NFW = [-122, 31]  $\text{km s}^{-1}$ ). Unfortunately the presence of 2MASXJ21372816-3824412 makes it difficult to attribute this gas solely to ESO343-G014. Additionally, this gas could be attributed to either the approaching or receding side of the disk due to the large impact parameter and high azimuth angle of the sightline.

### A.3 IC5325

IC5325 is a mostly face-on SAB(rs)bc type galaxy with a measured systemic velocity  $v_{sys} = 1512 \pm 8 \text{ km s}^{-1}$ . Its inclination is just high enough ( $i = 25^\circ$ ) to obtain a reasonable rotation curve. The closest neighboring galaxy is ESO347-G020 to the southeast at 306 kpc and  $v_{sys} = 1745 \text{ km s}^{-1}$ . Three other much smaller galaxies are also located  $\sim 450$  kpc to the southwest. The background QSO RBS2000 is located northeast at  $\rho = 314$  kpc

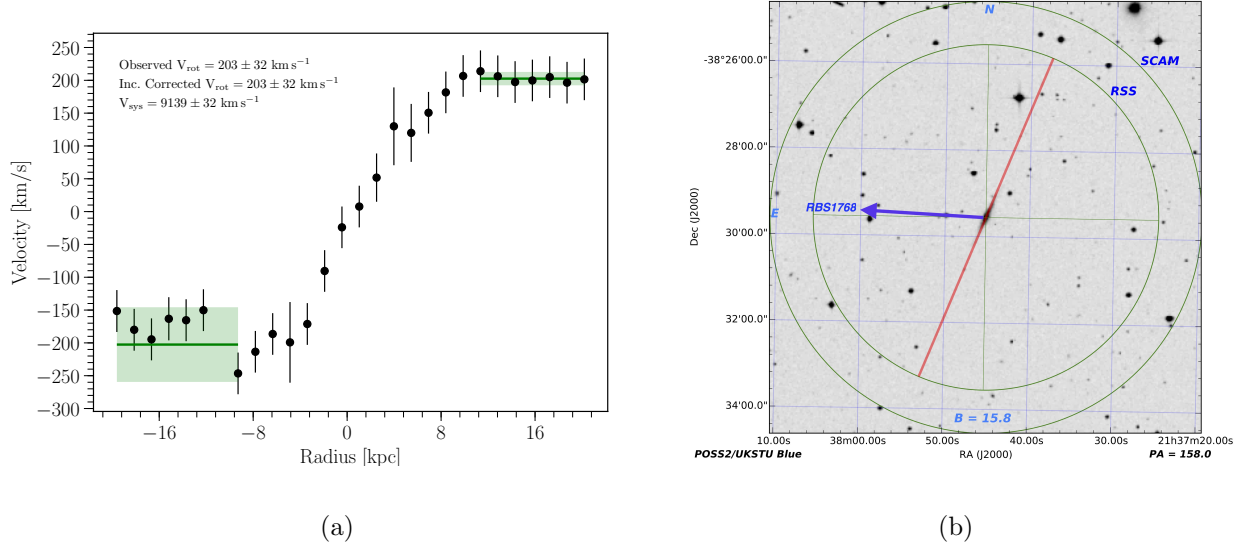


**Figure 4.10 :** a) Rotation curve of ESO343-G014. The solid green line indicates the weighted mean velocity over the corresponding x-axis region, and the shaded green indicates the  $1\sigma$  error in the mean. b) SALT finder chart for ESO343-G014 showing the position of the slit in red.

and  $64^\circ$  azimuth angle on the approaching side of IC5325. We detect Ly $\alpha$  at  $v_{\text{Ly}\alpha} = 1598 \text{ km s}^{-1}$  ( $\Delta v = 86 \text{ km s}^{-1}$ ) towards RBS2000. While this velocity is anti-aligned with the rotation the disk gas relative to our model predictions (cylindrical = [-41, -20], NFW = [-29, 1]  $\text{km s}^{-1}$ ), the low inclination angle of IC5325 leads to a highly uncertain position angle. Without additional observations, we cannot say for certain if the location of RBS2000 actually lies on the approaching or receding side. This position angle uncertainty also means our SALT rotation curve is a lower limit on the true rotation velocity of IC5325.

#### A.4 MCG-03-58-009

MCG-03-58-009 is a massive and very isolated Sc type galaxy at a measured systemic velocity of  $v_{\text{sys}} = 9015 \pm 19 \text{ km s}^{-1}$  and inclination angle of  $i = 49^\circ$ . The background QSO MRC2251-178 is located southeast at  $\rho = 355 \text{ kpc}$  at an azimuth angle of  $71^\circ$  on the receding side. We detect a weak Ly $\alpha$  absorber at  $v_{\text{Ly}\alpha} = 9029 \text{ km s}^{-1}$  ( $\Delta v = 14 \text{ km s}^{-1}$ ) towards

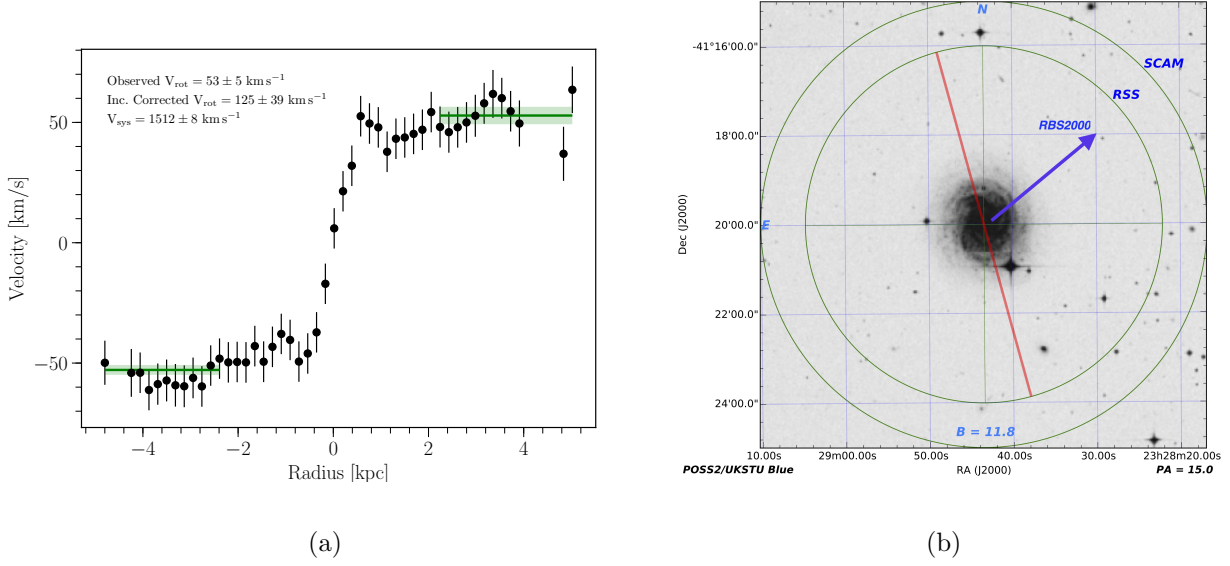


**Figure 4.11 :** a) Rotation curve of IC5325. The solid green line indicates the weighted mean velocity over the corresponding x-axis region, and the shaded green indicates the  $1\sigma$  error in the mean. b) SALT finder chart for IC5325 showing the position of the slit in red.

MRC2251-178. This absorber velocity falls well within the expected range for co-rotation relative to our models (cylindrical = [-26, 137], NFW = [-42, 83]  $\text{km s}^{-1}$ ). Although this absorber matches the velocity expected for co-rotation, the velocity difference ( $\Delta v = 14 \text{ km s}^{-1}$ ) is also within the systemic velocity uncertainty for MCG-03-58-009. The relative weakness of this absorber ( $\text{EW} = 62 \pm 4 \text{ m}\text{\AA}$ ) is somewhat unusual given it's proximity (just outside of  $1 R_{\text{vir}}$ ) to a massive galaxy. If this is representative of an isolated system such as MCG-03-58-009, then we should expect the halo rotational velocity to approach systemic by  $1 R_{\text{vir}}$ .

### A.5 NGC1566

NGC1566 is a SAB(rs)bc type galaxy with measured systemic velocity of  $v_{\text{sys}} = 1502 \pm 15 \text{ km s}^{-1}$  and inclination angle of  $i = 46^\circ$ . There are several other large galaxies at  $\rho \gtrsim 200 \text{ kpc}$  from NGC1566 (e.g., NGC1549, NGC1596, and NGC1581). The closest

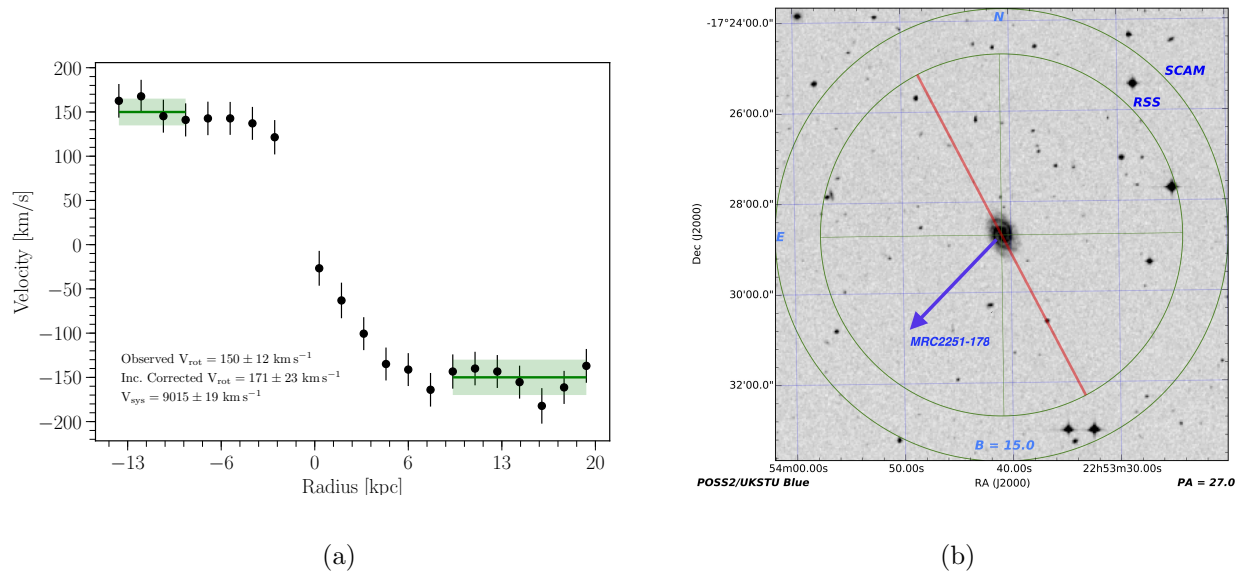


**Figure 4.12 :** a) Rotation curve of MCG-03-58-009. The solid green line indicates the weighted mean velocity over the corresponding x-axis region, and the shaded green indicates the  $1\sigma$  error in the mean. b) SALT finder chart for MCG-03-58-009 showing the position of the slit in red.

QSO sightline is toward HE0429-5343, northeast of NGC1566 at  $\rho = 256$  kpc and  $60^\circ$  azimuth angle. We detect Ly $\alpha$  absorption toward HE0429-5343 at  $v_{\text{Ly}\alpha} = 1167, 1358 \text{ km s}^{-1}$  ( $\Delta v = -335, -144 \text{ km s}^{-1}$ ). Both of these absorbers have the correct velocity *sign*, but we would expect a smaller velocity for co-rotation based on our model results (cylindrical = [-53, -2], NFW = [-22, 17]  $\text{km s}^{-1}$ ). Unfortunately NGC1617 is slightly closer to this sightline than NGC1566, at  $\rho = 233$  kpc and  $v_{\text{sys}} = 1063 \text{ km s}^{-1}$ , so it is not possible to confidently attribute these absorbers to NGC1566.

A more distant QSO sightline toward 1H0419-577 is located to the south at  $\rho = 303$  kpc and just east of the receding side of the major axis at an azimuth angle of  $10^\circ$ . We detect Ly $\alpha$  at  $v_{\text{Ly}\alpha} = 1123, 1188, 1264 \text{ km s}^{-1}$  ( $\Delta v = -379, -314, -238 \text{ km s}^{-1}$ ), all of which are the wrong sign for co-rotation relative to our models (cylindrical = [48, 76], NFW = [-2, 31]  $\text{km s}^{-1}$ ). This sightline is *also* actually closer to a small group of galaxies

including NGC1549, NGC1546 and NGC1536, all with systemic velocities near  $\sim 1200 \text{ km s}^{-1}$ . Additionally, this absorber system contains C III, C IV, Si II, Si III, Si IV lines. These lines likely are associated with this group rather than with NGC1566.

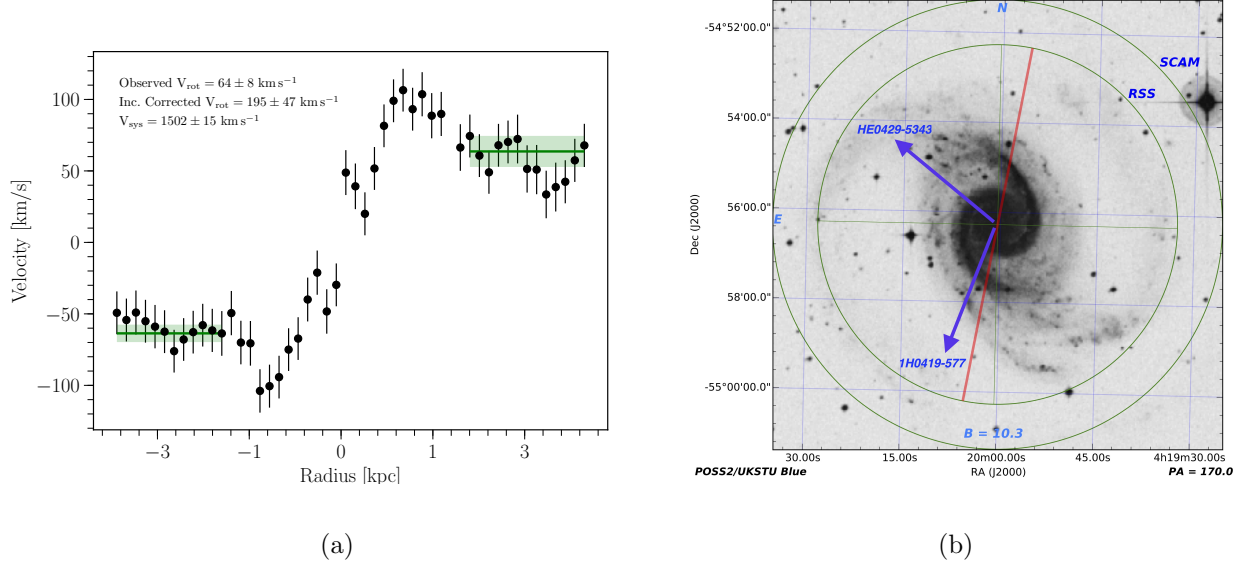


**Figure 4.13 :** a) Rotation curve of NGC1566. The solid green line indicates the weighted mean velocity over the corresponding x-axis region, and the shaded green indicates the  $1\sigma$  error in the mean. b) SALT finder chart for NGC1566 showing the position of the slit in red.

## A.6 NGC3513

NGC3513 a mostly face-on SB(rs)c galaxy with measured systemic velocity  $v_{\text{sys}} = 1204 \pm 12 \text{ km s}^{-1}$ . It has a companion galaxy in NGC3511 at  $\rho = 44 \text{ kpc}$  and  $v_{\text{sys}} = 1109 \text{ km s}^{-1}$  (NGC3513 diameter  $D = 22.1 \text{ kpc}$ , NGC3511 diameter  $D = 28.1 \text{ kpc}$ ). The background QSO H1101-232 is located directly south of the pair at  $\rho = 60 \text{ kpc}$  and azimuth angle of  $67^\circ$  on the receding side. We detect Ly $\alpha$  at  $v_{\text{Ly}\alpha} = 1182 \text{ km s}^{-1}$  ( $\Delta v = -22 \text{ km s}^{-1}$ ) toward H1101-232. NGC3513 appears to be rotating slowly, with a maximal inclination-corrected rotation velocity of  $v_{\text{rot}} / \sin(i) = 22 \pm 24 \text{ km s}^{-1}$ . The  $\Delta v = -22 \text{ km s}^{-1}$  for this absorber is opposite in sign for co-rotation on the sky and just outside our predicted model

velocity range (cylindrical = [-19, 27], NFW = [-19, 28] km s<sup>-1</sup>). Given that NGC3511 is so close, this absorber's velocity is probably subject to a complex velocity field influenced by both NGC3511 and NGC3513. For this reason we have marked this galaxy as "uncertain" in all map plots and have not included it in our statistical results. This absorber system also contains C IV, N V, Si II, Si III, and Si IV lines.

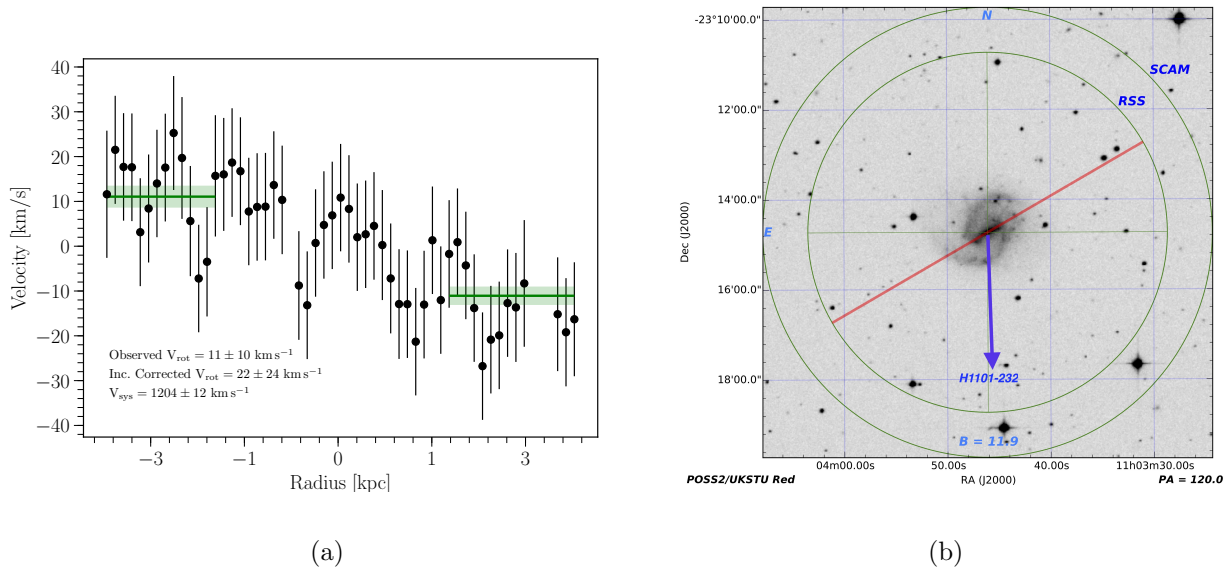


**Figure 4.14 :** a) Rotation curve of NGC3513. The solid green line indicates the weighted mean velocity over the corresponding x-axis region, and the shaded green indicates the  $1\sigma$  error in the mean. b) SALT finder chart for NGC3513 showing the position of the slit in red.

## A.7 NGC3633

NGC3633 is an isolated, edge-on SAa type galaxy with a measured systemic velocity  $v_{\text{sys}} = 2587 \pm 7$  km s<sup>-1</sup>. Several locations along the disk of NGC3633 show two velocities for emission. We have combined these into a single velocity measurement via a weighted average.

The background QSO RX\_J1121.2+0326 is located southeast at  $\rho = 184$  kpc and  $58^\circ$  azimuth on the approaching side of NGC3633. We detect Ly $\alpha$  at  $v_{\text{Ly}\alpha} = 2605$

$\text{km s}^{-1}$  ( $\Delta v = 18 \text{ km s}^{-1}$ ) toward RX\_J1121.2+0326. While close to  $v_{\text{sys}}$ , this absorber velocity is just outside our predicted model velocities (cylindrical = [-153, -14], NFW = [-77, 10]  $\text{km s}^{-1}$ ). However, this absorber is also very weak and broad, making the velocity center uncertain by at least  $\sim 10 \text{ km s}^{-1}$ . Taking this along with the uncertainty in  $V_{\text{sys}}$ , this absorber could still be consistent with co-rotation.

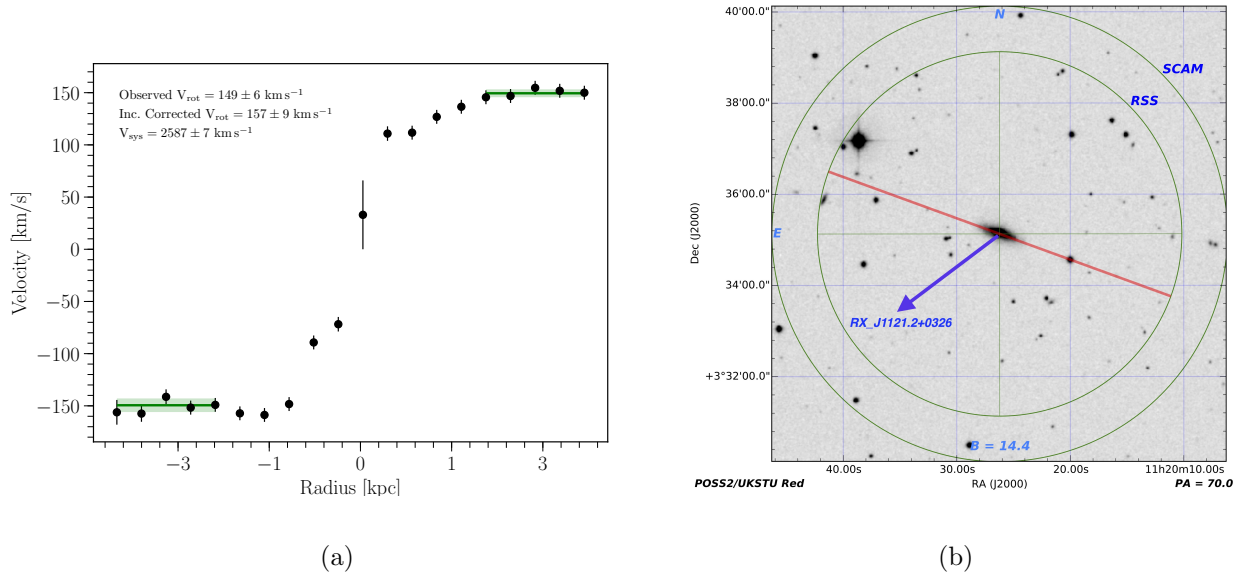


**Figure 4.15 :** a) Rotation curve of NGC4536. The solid green line indicates the weighted mean velocity over the corresponding x-axis region, and the shaded green indicates the  $1\sigma$  error in the mean. b) SALT finder chart for NGC3633 showing the position of the slit in red.

## A.8 NGC4536

NGC4536 is a SAB(rs)bc type galaxy located in the Virgo Cluster at a measured systemic velocity of  $v_{\text{sys}} = 1867 \pm 33 \text{ km s}^{-1}$  and inclination  $i = 61^\circ$ . The data on the receding side of NGC4536 is quite messy, and may include contamination from background sources. Hence, our measured systemic velocity, and thus rotation velocity of  $139 \pm 37 \text{ km s}^{-1}$ , have relatively high uncertainty. Other published redshift values available from

NED and rotation velocities from the HyperLEDA database are broadly consistent with our values, albeit biased slightly lower and higher in velocity, respectively.

There are 2 sightlines to the southwest of NGC4536, both on the receding side of the galaxy. HE1228+0131 at  $\rho = 338$  kpc and  $86^\circ$  azimuth has 5 Ly $\alpha$  lines:  $v_{\text{Ly}\alpha} = 1495, 1571, 1686, 1721, 1854 \text{ km s}^{-1}$  ( $\Delta v = -372, -296, -181, -146, -13 \text{ km s}^{-1}$ ). None of these are of the correct orientation for co-rotation relative to our model predictions (cylindrical = [18, 51], NFW = [2, 32]  $\text{km s}^{-1}$ ), and all are more likely to be associated with other nearby galaxies, such as NGC4517A, which is slightly closer to these absorbers in impact parameter and velocity than is NGC4536. At  $v_{\text{Ly}\alpha} = 1686 \text{ km s}^{-1}$  we also detect C II, C IV, Si II, Si III, and Si IV, and at  $v_{\text{Ly}\alpha} = 1721 \text{ km s}^{-1}$  we detect Lyman series from Ly $\alpha$  to Ly $\theta$  as well as C II, C III, C IV, Si II, Si III, and Si IV.

The second nearby sightline is toward 3C273 at  $\rho = 344$  kpc and  $46^\circ$  azimuth angle, and shows 3 Ly $\alpha$  lines at  $v_{\text{Ly}\alpha} = 1580, 2156, 2267 \text{ km s}^{-1}$  ( $\Delta v = -287, 289, 400 \text{ km s}^{-1}$ ). Two of these are correctly oriented for co-rotation relative to our model predictions (cylindrical = [87, 121], NFW = [5, 41]  $\text{km s}^{-1}$ ), but are too high in velocity to make this scenario probable. Overall, given the number of nearby galaxies and their locations, we would expect these absorbers to trace the overall velocity field instead of the halo rotation of any particular galaxy. After this galaxy was included in the SALT observing queue we realized it is actually located in the Virgo cluster, so we have decided to remove it from the statistical sample in this paper but present the observed data here nonetheless.

## A.9 NGC4939

NGC4939 is a large SA(s)bc type galaxy with measured systemic velocity  $v_{\text{sys}} = 3093 \pm 33 \text{ km s}^{-1}$  and inclination  $i = 48^\circ$ . The background QSO PG1302-102 is located southeast at  $\rho = 254$  kpc and  $61^\circ$  azimuth angle on the approaching side of NGC4939. We

detect a Ly $\alpha$  absorber at  $v_{\text{Ly}\alpha} = 3448 \text{ km s}^{-1}$  ( $\Delta v = 355 \text{ km s}^{-1}$ ) towards PG1302-102. As this absorber is located on the approaching side, we can easily rule out co-rotation in this case. NGC4939 does not have any close neighbors, so represents an intriguing case against co-rotation for gas past  $1R_{\text{vir}}$ .

### A.10 NGC5364

NGC5364 is a SA(rs)bc pec type galaxy at a measured systemic velocity  $v_{\text{sys}} = 1238 \pm 17 \text{ km s}^{-1}$  and inclination  $i = 57^\circ$ . It is located in a group environment with 5 other large, nearby galaxies. The background QSO SDSSJ135726.27+043541.4 is located southeast at  $\rho = 165 \text{ kpc}$  and  $84^\circ$  azimuth angle on the receding side of NGC5364. We detect Ly $\alpha$  at  $v_{\text{Ly}\alpha} = 967, 1124 \text{ km s}^{-1}$  ( $\Delta v = -271, -114 \text{ km s}^{-1}$ ) toward SDSSJ135726.27+043541.4. These absorbers have the opposite sign for co-rotation relative to our model predictions

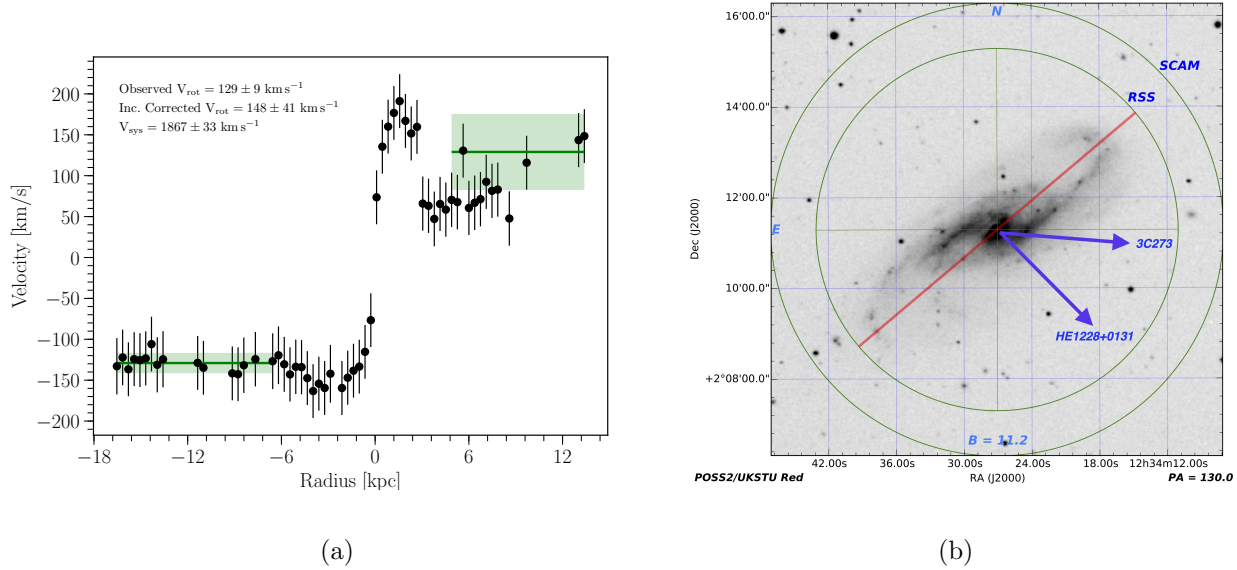


**Figure 4.16 :** a) Rotation curve of NGC4536. The solid green line indicates the weighted mean velocity over the corresponding x-axis region, and the shaded green indicates the  $1\sigma$  error in the mean. b) SALT finder chart for NGC4536 showing the position of the slit in red.

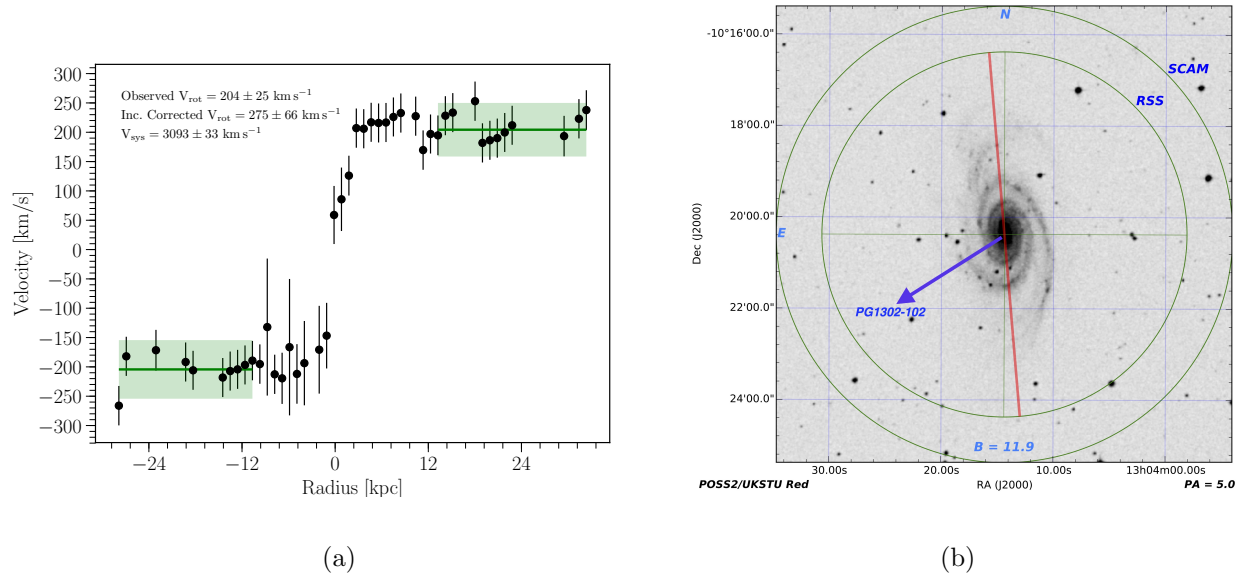


**Figure 4.17 :** a) Rotation curve of NGC4939. The solid green line indicates the weighted mean velocity over the corresponding x-axis region, and the shaded green indicates the  $1\sigma$  error in the mean. b) SALT finder chart for NGC4939 showing the position of the slit in red.

(cylindrical = [-26, 108], NFW = [-30, 68]  $\text{km s}^{-1}$ ). However, because of the orientation of NGC5364 on the sky with respect to this sightline, these absorbers lie extremely close to the inflection point where projected rotation velocities flip to approaching instead of receding. For example, shifting the location of SDSSJ135726.27+043541.4 east by a tenth of a degree ( $\sim 20$  kpc) is sufficient to put these absorbers on the approaching side of NGC5364. Hence, both of these absorbers could be co-rotating with NGC5364 given very reasonable assumptions on the shape of an extended disk. Nonetheless, the fact that this system lives in galaxy group environment likely dominates the surrounding velocity field.

### A.11 NGC5786

NGC5786 is a large, strongly-barred spiral galaxy with measured systemic velocity  $v_{\text{sys}} = 2975 \pm 22 \text{ km s}^{-1}$  and inclination  $i = 65^\circ$ . The background QSO QSO1500-4140 is

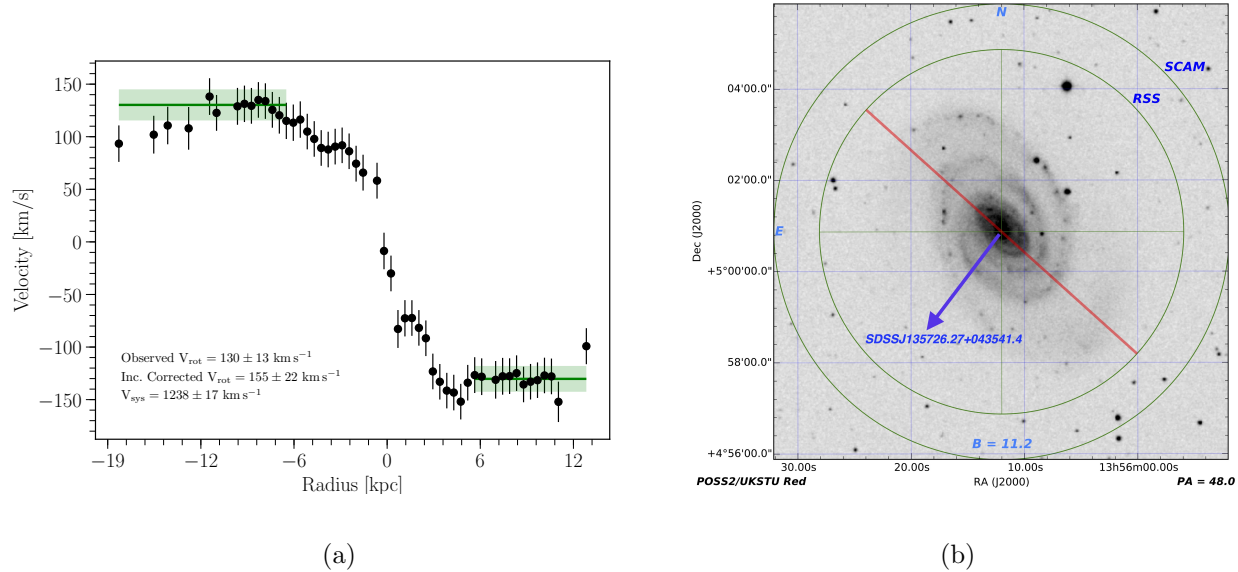


**Figure 4.18** : a) Rotation curve of NGC5364. The solid green line indicates the weighted mean velocity over the corresponding x-axis region, and the shaded green indicates the  $1\sigma$  error in the mean. b) SALT finder chart for NGC5364 showing the position of the slit in red.

located directly east at  $\rho = 453$  kpc and  $1^\circ$  azimuth angle on the receding side of NGC5786. We detect Ly $\alpha$  at  $v_{\text{Ly}\alpha} = 3138 \text{ km s}^{-1}$  ( $\Delta v = 163 \text{ km s}^{-1}$ ) toward QSO1500-4140, which is slightly above the model predicted velocity range (cylindrical = [106, 160], NFW = [19, 67]  $\text{km s}^{-1}$ ). However, the two neighboring galaxies ESO327-G038 and ESO327-G039 are both located south of NGC5786 at  $\rho = 62, 296$  kpc, respectively. These nearby galaxies, along with the large distance to the absorption ( $\sim 2.5R_{\text{vir}}$ ), make it difficult to believe this as evidence of an NGC5786 extended disk.

## A.12 UGC09760

UGC09760 is an edge-on, slow-rotating Sd galaxy with measured systemic velocity  $v_{\text{sys}} = 2094 \pm 16 \text{ km s}^{-1}$ . This systemic velocity deviates slightly from other published redshifts, such as the The Updated Zwicky Catalog value of  $v_{\text{sys}} = 2023 \pm 2 \text{ km s}^{-1}$  (Falco

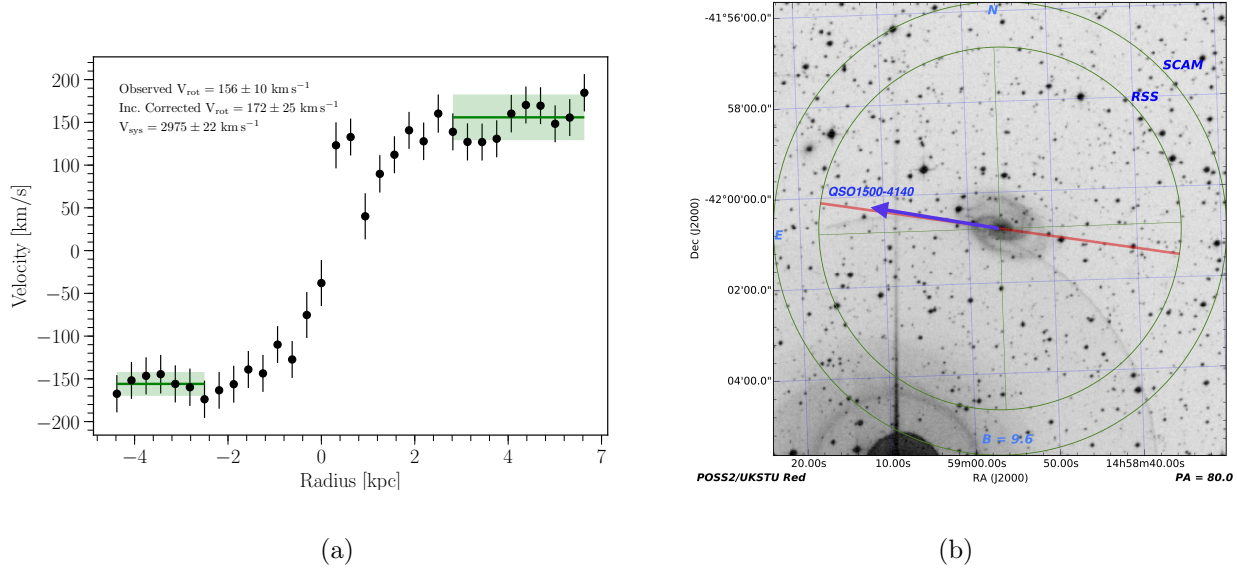


**Figure 4.19 :** a) Rotation curve of NGC5786. The solid green line indicates the weighted mean velocity over the corresponding x-axis region, and the shaded green indicates the  $1\sigma$  error in the mean. b) SALT finder chart for NGC5786 showing the position of the slit in red.

et al. 1999). This is likely due to our method of imposing rotation symmetry and averaging the approaching and receding velocities to derive  $v_{\text{sys}}$ . If we do not sample the rotation curve far enough out, a systematic offset is not unreasonable. Indeed, we do not detect the rotation curve turnover or flattening point.

The background QSO SDSSJ151237.15+012846.0 is located southeast at  $\rho = 123$  kpc and  $90^\circ$  azimuth angle. We detect Ly $\alpha$  absorption at  $v_{\text{Ly}\alpha} = 2029 \text{ km s}^{-1}$  ( $\Delta v = -65 \text{ km s}^{-1}$ ) toward SDSSJ151237.15+012846.0. This velocity falls outside the model predictions for co-rotation (cylindrical = [-30, 30], NFW = [-30, 86]  $\text{km s}^{-1}$ ), but unfortunately this sightline lies almost exactly at an azimuth of  $90^\circ$ . Hence, the motion of this gas could easily be either co-rotating or counter-rotating depending on a minute change in the position angle assigned to UGC09760. This is especially true if we assume our measured  $v_{\text{sys}}$  is erroneously high, and indeed closer to the values obtained by other observations. For

example, if we adjust the position angle by a single degree, to  $56^\circ$  instead of  $57^\circ$ , our model predictions become (cylindrical = [-30, 30] , NFW = [-79, 30]  $\text{km s}^{-1}$ ) and this absorber becomes consistent with co-rotation in the NFW model.

It is worth noting that there are several small satellite galaxies nearby, including SDSSJ151208.16+013508.5, SDSSJ151121.63+013637.6, SDSSJ151241.38+013723.7 and UGC09746 (impact parameters  $\rho = 53, 88, 82, 230$  kpc respectively). All of these galaxies lie slightly blue-ward of UGC09760, and thus *further* away in velocity from the Ly $\alpha$  absorber at  $2029 \text{ km s}^{-1}$ .

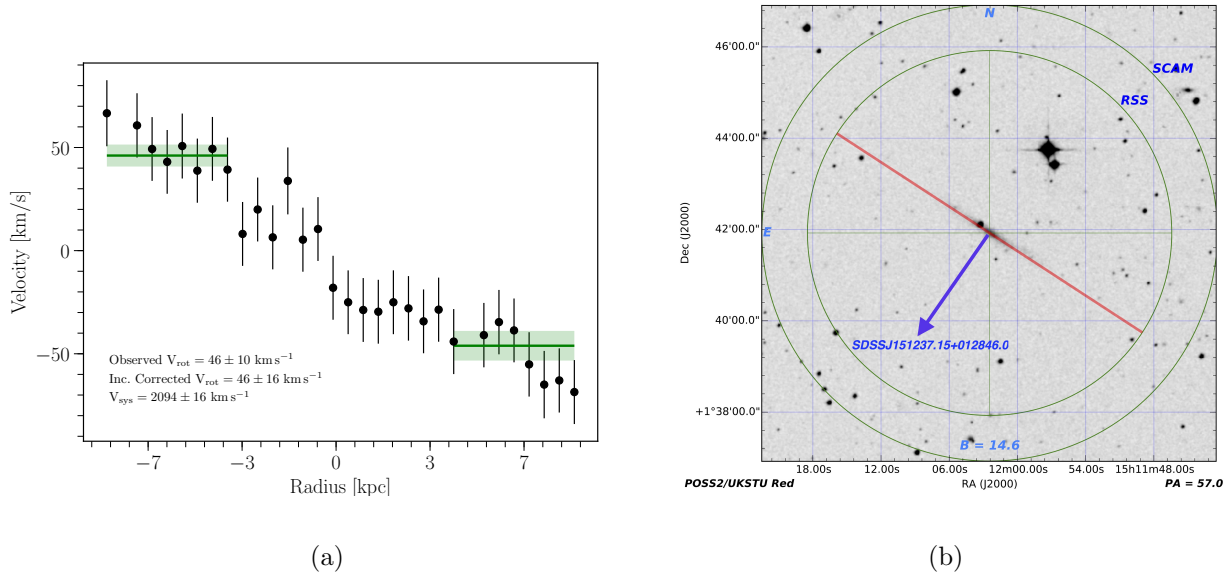


**Figure 4.20 :** a) Rotation curve of UGC09760. The solid green line indicates the weighted mean velocity over the corresponding x-axis region, and the shaded green indicates the  $1\sigma$  error in the mean. b) SALT finder chart for UGC09760 showing the position of the slit in red.

## B Ancillary Data

To increase our sample size we have also searched the literature for galaxies with published rotation curves and orientations. Unfortunately, while the rotation velocity

is available for thousands of galaxies, only a handful of publications also include the *orientation* of the rotation on the sky. Of these, we were able to find 18 additional galaxies which have a systemic velocity greater than  $\sim 500 \text{ km s}^{-1}$ , and are near to a COS or STIS sightline with available data. We have included 4 of the galaxy-QSO systems analyzed by Côté et al. (2005). We briefly summarize each of these systems here (see Sections B.9 - B.11), and refer the reader to Côté et al. (2005) for a more complete discussion. As new spectra and redshift-independent distances are available for these systems our results, while similar, are not identical.

## B.1 NGC3198

NGC3198 is a SB(rs)c type galaxy with systemic velocity  $v_{\text{sys}} = 661 \pm 3 \text{ km s}^{-1}$  and inclination  $= i = 70^\circ$ . It is a well studied galaxy, and is included the detailed THINGS rotation curve study of de Blok et al. (2008). We extracted the raw rotation curve derived by de Blok et al. (2008) using the plot digitization software WebPlotDigitizer<sup>3</sup>. NGC3198 has an even and flat rotation curve, with an average velocity of  $v_{\text{rot}} = 152 \text{ km s}^{-1}$ . The background QSO RX\_1017.5+4702 is located northeast at  $\rho = 370 \text{ kpc}$  and  $55^\circ$  azimuth angle on the approaching side of NGC3198. We detect Ly $\alpha$  toward RX\_1017.5+4702 at  $v_{\text{Ly}\alpha} = 629 \text{ km s}^{-1}$  ( $\Delta v = -32 \text{ km s}^{-1}$ ), which can nicely be described by a co-rotating disk based on our model predicted velocity range (cylindrical = [-153, -21], NFW = [-91, 6]  $\text{km s}^{-1}$ ). We note that the small dwarf galaxy SDSSJ101848.77+452137.0 is located 65 kpc away from NGC3198 toward the southwest.

---

<sup>3</sup>WebPlotDigitizer; <http://arohatgi.info/WebPlotDigitizer>

## B.2 NGC3351

NGC3351 is a mostly face-on ( $i = 29^\circ$ ) SB(r)b type galaxy with systemic velocity  $v_{\text{sys}} = 778 \pm 4 \text{ km s}^{-1}$ . It is located  $\sim 200$  kpc southwest of the core of the Leo I group. We take the rotation curve and orientation produced by Dicaire et al. (2008). While we expect any extended disk rotation to be quickly disrupted due to the complex Leo I environment, this galaxy also has one of the closest sightlines in our sample with SDSSJ104335.90+115129.0 at  $\rho = 31$  kpc and  $13^\circ$  azimuth on the northwest, approaching side. We detect Ly $\alpha$  at  $v_{\text{Ly}\alpha} = 717, 882, 1030 \text{ km s}^{-1}$  ( $\Delta v = -61, 104, 252 \text{ km s}^{-1}$ ) toward this sightline. The lowest velocity absorber agrees nicely with both models for co-rotation, while the other two are above our model predictions (cylindrical = [-99, 12], NFW = [-68, 20]  $\text{km s}^{-1}$ ). We also detect multiple metal ions associated with  $v_{\text{Ly}\alpha} = 717 \text{ km s}^{-1}$  line, including C II, N I, N V, O I, Si II, Si III, Si IV, S II, and Fe II.

## B.3 NGC5907

NGC5907 is a large, edge-on SA(s)c type galaxy with systemic velocity  $v_{\text{sys}} = 670 \pm 3 \text{ km s}^{-1}$ . We take the rotation curve and orientation produced by Yim et al. (2014). The background QSO SBS1503+570 is located northwest at  $\rho = 413$  kpc and  $47^\circ$  azimuth angle on the receding side of NGC5907. We detect Ly $\alpha$  at  $v_{\text{Ly}\alpha} = 708 \text{ km s}^{-1}$  ( $\Delta v = 38 \text{ km s}^{-1}$ ), which falls within the model predictions for co-rotation (cylindrical = [31, 228], NFW = [-24, 101]  $\text{km s}^{-1}$ ). Unfortunately there are several other nearby galaxies, the largest of which being NGC5866 (diameter  $D = 20.8$  and impact parameter  $\rho = 208$  kpc, versus for NGC5907 -  $D = 50.6$  and  $\rho = 413$  kpc). Hence, it is difficult to assign this absorber to NGC5907 alone.

#### B.4 NGC4565

NGC4565 is an edge-on SA(s)b type galaxy with systemic velocity  $v_{\text{sys}} = 1230 \pm 5 \text{ km s}^{-1}$ . We take the rotation curve and orientation produced by Sofue (1996). The background QSO RX\_J1236.0+2641 is located directly north at  $\rho = 147 \text{ kpc}$  and  $41^\circ$  azimuth angle on receding side of NGC4565. We detect Ly $\alpha$  absorption at  $v_{\text{Ly}\alpha} = 1009, 1166, 1254 \text{ km s}^{-1}$  ( $\Delta v = -221, -64, 24 \text{ km s}^{-1}$ ) toward RX\_J1236.0+2641. Only the  $v_{\text{Ly}\alpha} = 1254 \text{ km s}^{-1}$  line is consistent with co-rotating gas relative to our model predictions (cylindrical = [-2, 246], NFW = [-30, 144]  $\text{km s}^{-1}$ ). However, the presence of several other nearby galaxies (e.g., NGC4559, NGC4562) surely disrupts any possible extended disk rotation that would otherwise be detectable via sightline absorption.

#### B.5 UGC06446

UGC06446 is a Sd type galaxy with systemic velocity  $v_{\text{sys}} = 644 \pm 1 \text{ km s}^{-1}$  and inclination  $i = 48^\circ$  on the far northwest edge of the Ursa Major cluster of galaxies. We take the rotation curve and orientation information produced by (Verheijen & Sancisi 2001; Swaters et al. 2009). The background QSO SDSSJ112448.30+531818.0 is located southwest at  $\rho = 143 \text{ kpc}$  and  $22^\circ$  azimuth angle on the receding side of UGC06446. We detect Ly $\alpha$  at  $v_{\text{Ly}\alpha} = 664, 1019 \text{ km s}^{-1}$  ( $\Delta v = 20, 375 \text{ km s}^{-1}$ ). The absorber at  $v_{\text{Ly}\alpha} = 664$  falls well within our model predicted co-rotation range (cylindrical = [-9, 65], NFW = [-15, 61]  $\text{km s}^{-1}$ ), but the absorber at  $v_{\text{Ly}\alpha} = 1019$  is far more likely to be associated with NGC3631 ( $\rho = 86 \text{ kpc}$ ,  $v_{\text{sys}} = 1156 \text{ km s}^{-1}$ ). We therefore treat these as separate systems.

#### B.6 NGC3631

NGC3631 is a mostly face-on ( $i = 17^\circ$ ) SA(s)c type galaxy with systemic velocity  $v_{\text{sys}} = 1156 \pm 1 \text{ km s}^{-1}$ . We take the rotation curve and orientation information produced

by Knapen (1997). There are 4 nearby QSOs, which we will present in order of increasing impact parameter.

First, the closest background QSO RX\_J1117.6+5301 is located southwest at  $\rho = 78$  kpc and  $75^\circ$  azimuth angle on the receding side of NGC3631. We detect Ly $\alpha$  at  $v_{\text{Ly}\alpha} = 1131, 1259 \text{ km s}^{-1}$  ( $\Delta v = -25, 103 \text{ km s}^{-1}$ ). Both of these lines fall outside of our model predicted velocities (cylindrical = [10, 24], NFW = [1, 21]  $\text{km s}^{-1}$ ).

Second, background QSO SDSSJ112448.30+531818.0 is located northeast at  $\rho = 86$  kpc and  $74^\circ$  azimuth angle on the approaching side of NGC3631. We detect Ly $\alpha$  at  $v_{\text{Ly}\alpha} = 1019, 1141 \text{ km s}^{-1}$  ( $\Delta v = -137, -15 \text{ km s}^{-1}$ ). Only the higher velocity absorber falls within our model predicted velocity range (cylindrical = [-26, -11], NFW = [-22, 1]  $\text{km s}^{-1}$ ).

Third, the background QSO SDSSJ111443.70+525834.0 is located in the same direction but farther than RX\_J1117.6+5301, at  $\rho = 145$  kpc and  $72^\circ$  azimuth angle on the receding side of NGC3631. We detect Ly $\alpha$  at  $v_{\text{Ly}\alpha} = 1163 \text{ km s}^{-1}$  ( $\Delta v = 7 \text{ km s}^{-1}$ ). This absorber appears to agree well with our model predicted velocity range (cylindrical = [8, 29], NFW = [-5, 24]  $\text{km s}^{-1}$ ).

Finally, the background QSO SBS1116+523 is located south at  $\rho = 163$  kpc and  $40^\circ$  azimuth angle on the approaching side of NGC3631, but we do not detect any Ly $\alpha$  within  $\pm 400$  of NGC3631.

## B.7 NGC3726

NGC3726 is a SAB(r)c type galaxy with systemic velocity  $v_{\text{sys}} = 866 \pm 1 \text{ km s}^{-1}$  and inclination  $i = 52^\circ$  on the southwestern edge of the Ursa Major galaxy cluster (Verheijen & Sancisi 2001). The closest background QSO, CSO1208, is located southeast at  $\rho = 369$  kpc and  $88^\circ$  azimuth angle on the receding side of NGC3726. We detect Ly $\alpha$  at  $v_{\text{Ly}\alpha} = 731, 874$

$\text{km s}^{-1}$  ( $\Delta v = -135, 8 \text{ km s}^{-1}$ ) toward CSO1208. Only the higher velocity absorber falls within our predicted velocity range (cylindrical = [-27, 29], NFW = [-28, 21]  $\text{km s}^{-1}$ ). A more distant QSO, RX\_J1142.7+4625, is located in the same direction as CSO1208 at  $\rho = 440 \text{ kpc}$  and  $86^\circ$  azimuth angle on the approaching side of NGC3726. We detect Ly $\alpha$  at  $v_{\text{Ly}\alpha} = 818 \text{ km s}^{-1}$  ( $\Delta v = -48 \text{ km s}^{-1}$ ), which falls just outside our predicted velocity range (cylindrical = [-34, -14], NFW = [-30, -7]  $\text{km s}^{-1}$ ).

These two QSOs lie very close to and on apposing sides of the minor axis, such that CSO1208 samples the receding side and RX\_J1142.7+4625 the approaching. Unfortunately, both are also closer to a small group of dwarf galaxies, including NGC3782 and MCG+08-21-092,  $\sim 100 \text{ km s}^{-1}$  blueward of NGC3726. The  $v_{\text{sys}} = 731 \text{ km s}^{-1}$  line toward CSO1208 is likely associated with this dwarf group, and the other lines may also be.

## B.8 NGC3067

NGC3067 is a mostly edge-on ( $i = 68^\circ$ ) SAB(s)ab type galaxy with systemic velocity  $v_{\text{sys}} = 1465 \pm 5 \text{ km s}^{-1}$ . This galaxy and the nearby QSO sightline toward 3C232 is a particularly well studied system. They are separated by only  $\rho = 11 \text{ kpc}$  ( $74^\circ$  azimuth angle on the northwest, receding side) and a Lyman Limit System (LLS) with column density  $N_{\text{H I}} = 1 \times 10^{20} \text{ cm}^{-2}$  is detected toward 3C232 at  $v_{\text{Ly}\alpha} = 1408 \text{ km s}^{-1}$ , which has been postulated as a high velocity cloud (HVC) orbiting NGC3067 (Carilli et al. 1989; Keeney et al. 2005).

We obtained the rotation curve for NGC3067 from Rubin et al. (1982) and the orientation from Carilli et al. (1989). While H $\text{I}$  measurements of this LLS fit a single component (at  $v_{\text{H I}} = 1421 \text{ km s}^{-1}$ ), we have fit 3 separate components at  $v_{\text{Ly}\alpha} = 1408, 1510, 1641 \text{ km s}^{-1}$  ( $\Delta v = -57, 45, 176 \text{ km s}^{-1}$ ) to match the associated metal lines (namely, C IV, Si II, Si III, Si IV, Mg II, Fe II, and N I all show at least 2 separate components).

This splitting has been analyzed in detail most recently by Keeney et al. (2005) and Stocke et al. (2010), who find similar but slightly lower  $v_{\text{Ly}\alpha}$  for all three absorbers. Only the lowest velocity component can strictly be described by our model velocity range (cylindrical = [-121, 25], NFW = [-139, 26]  $\text{km s}^{-1}$ ), however the  $v_{\text{Ly}\alpha} = 1510 \text{ km s}^{-1}$  component is also very close to this range. The  $v_{\text{Ly}\alpha} = 1641 \text{ km s}^{-1}$  component, however, must be either a counter-rotating clouddlet or an outflow directed away from our line of sight.

A second QSO SDSSJ095914.80+320357.0 is located farther away, to the southeast at  $\rho = 128 \text{ kpc}$  and  $43^\circ$  azimuth angle on the receding side of NGC3067. We detect Ly $\alpha$  at  $v_{\text{Ly}\alpha} = 1493 \text{ km s}^{-1}$  ( $\Delta v = 28 \text{ km s}^{-1}$ ), which agrees well with our model predicted velocity range (cylindrical = [11, 138], NFW = [-12, 81]  $\text{km s}^{-1}$ ).

## B.9 NGC6140

NGC6140 is a small SB(s)cd type galaxy with systemic velocity  $v_{\text{sys}} = 910 \pm 4 \text{ km s}^{-1}$  and inclination  $i = 45^\circ$ . We take the rotation curve and orientation information produced by Côté et al. (2005). A background QSO Mrk876 is located northwest at  $\rho = 113 \text{ kpc}$  and azimuth angle  $21^\circ$  (although this is somewhat uncertain; the position angle for NGC6140 could be closer to  $60^\circ$  than our adopted value of  $94^\circ$  due to it being mostly face on, faint, and strongly barred). We detect Ly $\alpha$  at  $v_{\text{Ly}\alpha} = 939 \text{ km s}^{-1}$  ( $\Delta v = 29 \text{ km s}^{-1}$ ) toward MRK876. This absorber velocity is of the correct *sign*, but just under the the model predicted velocity range (cylindrical = [40, 101], NFW = [35, 102]  $\text{km s}^{-1}$ ) for co-rotation. However, this absorber is still likely co-rotating given both the velocity and position angle uncertainties. Additionally, we detect Ly $\beta$  and O VI associated with this Ly $\alpha$  absorber (see Narayanan et al. (2010)).

## B.10 NGC4529

NGC4529 is an edge-on and isolated Scd type galaxy with systemic velocity  $v_{\text{sys}} = 2536 \pm 11 \text{ km s}^{-1}$ . We take the rotation curve and orientation information produced by Côté et al. (2005). The QSO MRK771 is located west at  $\rho = 159$  kpc and  $23^\circ$  azimuth angle on the approaching side of NGC4529. We detect Ly $\alpha$  at  $v_{\text{sys}} = 2553 \text{ km s}^{-1}$  ( $\Delta v = 17 \text{ km s}^{-1}$ ), which is anti-rotating relative to our model predictions (cylindrical = [-103, -40], NFW = [-87, -25]  $\text{km s}^{-1}$ ). As Côté et al. (2005) conclude, “there is simply no physical way to produce such a velocity with an extending co-rotating disk.”

## B.11 UGC04238

UGC04238 is an isolated and edge-on SBd type galaxy with systemic velocity  $v_{\text{sys}} = 1544 \pm 7 \text{ km s}^{-1}$ . We take the rotation curve and orientation information produced by Côté et al. (2005). The background QSO PG0804+761 is located directly south at  $\rho = 148$  kpc and  $59^\circ$  azimuth on the receding side of UGC04238. We detect Ly $\alpha$  at  $v_{\text{Ly}\alpha} = 1526, 1593 \text{ km s}^{-1}$  ( $\Delta v = -18, 49 \text{ km s}^{-1}$ ) toward PG0804+761. Relative to our model predictions (cylindrical = [-3, 86], NFW = [-10, 75]  $\text{km s}^{-1}$ ), although both are close, only the absorber at  $1593 \text{ km s}^{-1}$  (the lower EW of the two) falls within the expected velocity range for co-rotation.

## B.12 NGC2770

NGC2770 is a large, edge-on Sc type galaxy with systemic velocity  $v_{\text{sys}} = 1948 \pm 2 \text{ km s}^{-1}$ . It is mostly isolated except for two nearby small dwarfs MCG+06-20-036NED02 and GALEXASCJ090946.88+330840.4 (both 25 kpc away, on opposite sides of NGC2770). We take the rotation curve and orientation information produced by Rhee & van Albada

(1996). There are five nearby QSOs, which we present in order of increasing impact parameter.

First, the QSO FBQSJ0908+3246 is located south at  $\rho = 204$  kpc and  $59^\circ$  azimuth angle on the approaching side of NGC2770. We detect Ly $\alpha$  at  $v_{\text{Ly}\alpha} = 1915, 1982 \text{ km s}^{-1}$  ( $\Delta v = -33, 34 \text{ km s}^{-1}$ ). Relative to our model predictions (cylindrical = [-146, -4], NFW = [-117, 10]  $\text{km s}^{-1}$ ), only the lower velocity line can be described as co-rotating.

Second, the QSO TON1015 is located northeast at  $\rho = 218$  kpc and  $61^\circ$  azimuth angle on the receding side of NGC2770. We detect Ly $\alpha$  at  $v_{\text{Ly}\alpha} = 1833, 1985 \text{ km s}^{-1}$  ( $\Delta v = -115, 37 \text{ km s}^{-1}$ ). Relative to our model predictions (cylindrical = [3, 146], NFW = [-10, 115]  $\text{km s}^{-1}$ ), only the higher velocity absorber can be described as co-rotating.

Third the QSO SDSSJ091127.30+325337.0 is located southeast at  $\rho = 234$  kpc and  $30^\circ$  azimuth angle on the approaching side of NGC2770. We detect Ly $\alpha$  at  $v_{\text{Ly}\alpha} = 2063 \text{ km s}^{-1}$  ( $\Delta v = 115 \text{ km s}^{-1}$ ). Relative to our model predictions (cylindrical = [-150, -43], NFW = [-117, -19]  $\text{km s}^{-1}$ ), this absorber appears to be counter-rotating.

Fourth, the QSO SDSSJ091052.80+333008.0 is located northeast at  $\rho = 239$  kpc and  $66^\circ$  azimuth angle on the receding side of NGC2770. We detect Ly $\alpha$  at  $v_{\text{sys}} = 1824, 1975 \text{ km s}^{-1}$  ( $\Delta v = -124, 27 \text{ km s}^{-1}$ ). Relative to our model predictions (cylindrical = [6, 145], NFW = [-7, 112]  $\text{km s}^{-1}$ ), only the higher velocity absorber can be described as co-rotating.

Finally, the QSO TON1009 is located south at  $\rho = 267$  kpc and  $41^\circ$  azimuth angle on the approaching side of NGC2770. We detect Ly $\alpha$  at  $v_{\text{sys}} = 1908, 1980 \text{ km s}^{-1}$  ( $\Delta v = -40, 32 \text{ km s}^{-1}$ ). Relative to our model predictions (cylindrical = [-146, -39], NFW = [-110, -14]  $\text{km s}^{-1}$ ), only the lower velocity absorber can be described as co-rotating.

Interestingly, we appear to be detecting extended gas structures in these 5 sightlines. Toward the northeast we find TON1015 and SDSSJ091052.80+333008.0 and a set of absorber pairs at  $v_{\text{Ly}\alpha} = 1833, 1824 \text{ km s}^{-1}$  and  $v_{\text{Ly}\alpha} = 1985, 1975 \text{ km s}^{-1}$  each having

very similar EW and  $N_{\text{H I}}$ , and remarkably similar appearing line-structure. Adopting a distance of 28.6 Mpc to this cloud, we calculate a linear separation between TON1015 and SDSSJ091052.80+333008.0 of 28 kpc. Hence, there appears to be two distinct clouds of at least 28 kpc in physical extent sandwiched around the system velocity of NGC2770. Toward the south we find TON1009 and FBQ SJ0908+3246 and a set of absorber pairs at  $v_{\text{Ly}\alpha} = 1908, 1915 \text{ km s}^{-1}$  and  $v_{\text{Ly}\alpha} = 1980, 1982 \text{ km s}^{-1}$ , again with similar EW,  $N_{\text{H I}}$  and line-shapes.

### B.13 NGC3432

NGC3432 is an edge-on SB(s)m type galaxy with systemic velocity  $v_{\text{sys}} = 616 \pm 4 \text{ km s}^{-1}$ . It is interacting with the nearby dwarf galaxy UGC05983 located 11 kpc away and at  $v_{\text{sys}} = 765 \text{ km s}^{-1}$ . We take a rotation curve and orientation for NGC3432 from Rhee & van Albada (1996). The QSO CSO295 is located just 20 kpc away and just to the receding side of the minor axis ( $82^\circ$  azimuth angle). This is the second closest pair in our sample, after the 11 kpc separated NGC3067-3C232 system. We detect Ly $\alpha$  at  $v_{\text{Ly}\alpha} = 600, 662 \text{ km s}^{-1}$  ( $\Delta v = -16, 46 \text{ km s}^{-1}$ ) toward CSO295. Relative to our model predictions (cylindrical = [-37, 48], NFW = [-37, 134]  $\text{km s}^{-1}$ ) both of these absorbers are consistent with co-rotation. In fact, this orientation would represent the lower-velocity cloud existing toward the near-edge of the halo and the higher velocity cloud lying very close to the plane of the stellar disk. We also detect C II, Si II, Si III, and Si IV associated with this absorption system.

A second QSO RX\_J1054.2+3511 is located south at  $\rho = 290 \text{ kpc}$  and  $57^\circ$  azimuth angle on the receding side of NGC3432. We detect Ly $\alpha$  at  $v_{\text{sys}} = 703 \text{ km s}^{-1}$  ( $\Delta v = 87 \text{ km s}^{-1}$ ) toward RX\_J1054.2+3511. Relative to our model predictions (cylindrical = [0, 123], NFW = [-9, 111]  $\text{km s}^{-1}$ ), this absorber is consistent with co-rotation as well.

## B.14 NGC3666

NGC3666 is a mostly isolated and edge-on SA(rs)c type galaxy with systemic velocity  $v_{\text{sys}} = 1060 \pm 1 \text{ km s}^{-1}$ . We take the rotation curve and orientation information produced by Rhee & van Albada (1996). The QSO SDSSJ112439.50+113117.0 is located north at  $\rho = 58 \text{ kpc}$  and  $83^\circ$  azimuth angle on the approaching side of NGC3666. We detect Ly $\alpha$  at  $v_{\text{sys}} = 1047, 1099 \text{ km s}^{-1}$  ( $\Delta v = -13, 39 \text{ km s}^{-1}$ ) toward SDSSJ112439.50+113117.0. Relative to our model predictions (cylindrical = [-87, 20], NFW = [-136, 20]  $\text{km s}^{-1}$ ) the lower velocity absorber is consistent with co-rotation, while the other is slightly too high in velocity.

## B.15 NGC5951

NGC5951 is a large, edge-on SBc type galaxy with systemic velocity  $v_{\text{sys}} = 1780 \pm 1 \text{ km s}^{-1}$ . We take the rotation curve and orientation for NGC5951 from Rhee & van Albada (1996). The QSO 2E1530+1511 is located east at  $\rho = 55 \text{ kpc}$  and  $85^\circ$  azimuth angle on the receding side of NGC5951. We detect Ly $\alpha$  at  $v_{\text{Ly}\alpha} = 1795, 1953 \text{ km s}^{-1}$  ( $\Delta v = 15, 173 \text{ km s}^{-1}$ ) toward 2E1530+1511. Relative to our model predictions (cylindrical = [-31, 114], NFW = [-32, 125]  $\text{km s}^{-1}$ ), the lower velocity absorber is consistent with co-rotation while the other is a bit outside of the upper range. The pair of galaxies NGC5954 and NGC5953 are nearby ( $\sim 100 \text{ kpc}$ ), but the sightline toward 2E1530+1511 is closer and on the opposite side of NGC5951. Given the systemic velocity for the nearby galaxies NGC5954 and NGC5953 ( $v_{\text{sys}} = 1959, 1965 \text{ km s}^{-1}$ ), this absorber is likely also linked with that system.

## B.16 NGC7817

NGC7817 is an edge-on SAbc type galaxy with systemic velocity  $v_{\text{sys}} = 2309 \pm 4 \text{ km s}^{-1}$ . We take the rotation curve and orientation information produced by Rhee & van Albada (1996). The background QSO MRK335 is located southeast at  $\rho = 343 \text{ kpc}$  and almost directly along the minor axis of NGC7817 ( $90^\circ$  azimuth angle). We detect Ly $\alpha$  at  $v_{\text{sys}} = 1954, 2274 \text{ km s}^{-1}$  ( $\Delta v = -355, -35 \text{ km s}^{-1}$ ) toward MRK335. Because these absorbers lie almost exactly along the minor axis, our model predicts a very narrow velocity range for co-rotation (cylindrical = [-26, -24], NFW = [-26, -24]  $\text{km s}^{-1}$ ). While the higher velocity line falls a mere  $9 \text{ km s}^{-1}$  outside this predicted range, the absorption at  $1954 \text{ km s}^{-1}$  is likely not directly associated with NGC7817 given the large velocity difference. Additionally, the neighboring dwarf galaxy ESDOF538-02 ( $v_{\text{sys}} = 2175 \text{ km s}^{-1}$ ) appears in the same direction as MRK335 and only  $\rho = 57 \text{ kpc}$  away from NGC7817, and NSA126180 ( $v_{\text{sys}} = 1950 \text{ km s}^{-1}$ ) appears only  $\rho = 83 \text{ kpc}$  away from MRK335.

## B.17 UGC08146

UGC08146 is an isolated and edge-on Sd type galaxy with systemic velocity  $v_{\text{sys}} = 670 \pm 1 \text{ km s}^{-1}$ . This galaxy (and the nearby QSO PG1259+593) are included in the Côté et al. (2005) sample also, but we have taken the rotation curve and orientation information from Rhee & van Albada (1996). The QSO PG1259+593 is located northwest at  $\rho = 114 \text{ kpc}$  at  $50^\circ$  azimuth angle on the receding side of UGC08146. While Côté et al. (2005) cite a single Ly $\alpha$  component at  $v_{\text{Ly}\alpha} = 679 \text{ km s}^{-1}$ , we detect two components at  $v_{\text{Ly}\alpha} = 646, 683 \text{ km s}^{-1}$  ( $\Delta v = -24, 13 \text{ km s}^{-1}$ ), in the higher signal-to-noise COS data now available for PG1259+593. Relative to our model predictions (cylindrical = [-13, 82], NFW = [-16, 83]  $\text{km s}^{-1}$ ), the higher velocity component is consistent with co-rotation, and the other component is only  $8 \text{ km s}^{-1}$  shy of falling into the NFW co-rotation range as well.

## Chapter 5

### Conclusions

The conclusion!